

2015

Ultracold rubidium and potassium system for atom chip-based microwave and RF potentials

Austin R. Ziltz

College of William & Mary - Arts & Sciences

Follow this and additional works at: <https://scholarworks.wm.edu/etd>



Part of the [Atomic, Molecular and Optical Physics Commons](#), and the [Condensed Matter Physics Commons](#)

Recommended Citation

Ziltz, Austin R., "Ultracold rubidium and potassium system for atom chip-based microwave and RF potentials" (2015). *Dissertations, Theses, and Masters Projects*. Paper 1539624008.

<https://dx.doi.org/doi:10.21220/s2-rejy-4083>

This Dissertation is brought to you for free and open access by the Theses, Dissertations, & Master Projects at W&M ScholarWorks. It has been accepted for inclusion in Dissertations, Theses, and Masters Projects by an authorized administrator of W&M ScholarWorks. For more information, please contact scholarworks@wm.edu.

Ultracold Rubidium and Potassium System for Atom Chip-based
Microwave and RF Potentials

Austin R. Ziltz

Williamsburg, Virginia

Master of Science, College of William and Mary, 2010
Bachelor of Science, Bucknell University, 2008

A Dissertation presented to the Graduate Faculty
of the College of William and Mary in Candidacy for the Degree of
Doctor of Philosophy

Department of Physics

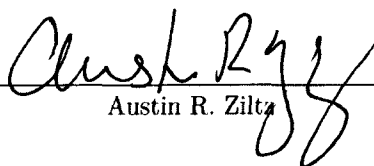
The College of William and Mary
May 2015

©2015
Austin R. Ziltz
All rights reserved.

APPROVAL PAGE

This Dissertation is submitted in partial fulfillment of
the requirements for the degree of


Doctor of Philosophy



Austin R. Ziltz


Approved by the Committee, April, 2015



Committee Chair

Associate Professor Seth Aubin, Physics
The College of William and Mary


Professor Todd Averett, Physics
The College of William and Mary


Professor Keith Griffioen, Physics
The College of William and Mary


Assistant Professor Eugeniy Mikhailov, Physics
The College of William and Mary


Professor Charles Sukenik, Physics
Old Dominion University

ABSTRACT PAGE

In this dissertation we study the development of microwave and RF near-field potentials for use with atom chip trapped atomic gases. These potentials are inherently spin-dependent, able to target individual spin states simultaneously. In contrast with traditional atom chip potentials, these RF traps can be operated at arbitrary bias magnetic field strengths and thus be combined with magnetic Feshbach resonances. Furthermore, these potentials can strongly suppress the potential roughness that plagues traditional atom chip potentials. We present a dual chamber atom chip apparatus for generating ultracold ^{87}Rb and ^{39}K atomic gases. The apparatus produces quasi-pure Bose-Einstein condensates of 10^4 ^{87}Rb atoms in an atom chip trap that features a dimple and good optical access. We have also demonstrated production of ultracold ^{39}K and subsequent loading into the chip trap. We describe the details of the dual chamber vacuum system, the cooling lasers, the magnetic trap, the multi coil magnetic transport system, and the atom chip. The apparatus is well suited for studies of atom-surface forces, quantum pumping and transport experiments, atom interferometry, novel chip-based traps, and studies of one-dimensional many-body systems.

TABLE OF CONTENTS

Acknowledgments	v
Dedication	vi
List of Tables	vii
List of Figures	viii

CHAPTER

1 Introduction	2
2 Ultracold Atom Theory	7
2.1 A Two Level Atom	7
2.2 Optical Potentials	8
2.2.1 Doppler Cooling	12
2.2.2 Sub-Doppler Cooling	15
2.2.3 Magneto-Optical Trapping	15
2.2.4 Practical Laser Cooling	19
2.2.5 Optical Pumping	21
2.2.6 Optical Dipole Traps	23
2.3 Magnetic Potentials	24
2.3.1 Magnetic Trapping	27
2.4 Temperature and Phase-Space Density	28
3 Microwave and RF Potentials	32
3.1 AC Zeeman Shift	32
3.2 Spin-Dependent Force	34
3.2.1 Feshbach Resonance	35

3.2.2	Spin-Selectivity	36
3.3	Atom Chip Near-Field Potentials	36
3.4	DC Magnetic Chip Traps	40
3.4.1	Atom Chip Modeling	42
3.5	Roughness Suppression	44
3.5.1	Simulation	48
3.5.2	Suppression Factor	53
4	Apparatus	55
4.1	Vacuum System	56
4.1.1	MOT Cell	56
4.1.2	Atom Chip Cell	57
4.1.3	Atom Source	58
4.1.4	Vacuum Quality	59
4.2	Laser Cooling System	60
4.2.1	Rubidium	64
4.2.2	Potassium	66
4.3	Magnetic Trapping and Transport	69
4.4	Atom Chip	72
4.4.1	RF Evaporation System	74
4.5	Imaging	74
4.6	Optical Dipole Trapping	76
5	System Performance	79
5.1	Rubidium: MOT to BEC	80
5.2	Dimple Trap	82
5.3	Potassium: MOT to Atom Chip	83
5.3.1	Atom Number Analysis	85

5.3.2	Performance Comparison	88
6	Magnetic Trapping System	89
6.1	Motivation	90
6.2	Coil and Mount Design	90
6.3	Magnetic Switch Driver	92
6.3.1	Design and Theory of Operation	93
6.4	Power Supply Considerations	98
6.5	Isolation and Remote Control	99
6.6	Calibration and Usage Notes	100
7	Magnetic Transport System	104
7.1	Magnetic Transport Constraints	106
7.1.1	Vertical Gradient	108
7.1.2	Aspect Ratio	108
7.2	Transport Velocity	109
7.3	MOT to Transport Handoff	111
7.4	Simulation	113
7.5	Design and Theory of Operation	115
7.5.1	Current Multiplexer	115
7.6	Transport Coils Design and Mount	115
7.7	Electrical Connections	120
7.8	Thermal Concerns	120
7.9	Installation	122
7.10	Performance	122
8	Potassium Laser Cooling System	128
8.1	Trap and Repumper Tunability	129
8.2	Single-Pass Tapered Amplifier	131

8.3	Double-Pass Scheme	135
8.4	^{39}K MOT Loading Rate	137
9	Microwave Evaporation System	141
9.1	Evaporative Cooling	141
9.1.1	Radio Frequency Evaporation	144
9.1.2	Microwave Evaporation	146
9.1.3	Sympathetic Evaporation	147
9.2	6.8 GHz Evaporation System	149
9.2.1	Design and Theory of Operation	149
9.2.2	Performance	151
9.3	Ultracold Atomic Tests and Techniques	152
9.3.1	Zeeman Level Cleaning and Stern-Gerlach Imaging	153
9.3.2	Adiabatic Rapid Passage	155
10	Summary and Outlook	157
10.1	Summary of Results and Limitations	158
10.2	Outlook and Potential Improvements	158
APPENDIX A		
	Engineering Designs	160
A.1	TIVAR MOT Coil Mount	160
A.2	Copper Transport System Mount	163
	Bibliography	166
	Vita	174

ACKNOWLEDGMENTS

This work would not have been possible without the guidance of my advisor, Dr. Seth Aubin, and the hard work of my colleagues in the group both past and present including Megan Ivory, Charles Fancher, A. J. Pyle, Jim Field and Aiyana Garcia. The excellent scientific, moral and L^AT_EX support of the one and only N. B. Phillips. For three long years since his defense, several more examples were set by those who made it out before me, including Matt Simons and Travis Horrom. The William & Mary Machine Shop and its personnel were invaluable resources for me over the years as well as the wonderful people who form the backbone of the Physics Department including Paula, Carol, Elle, Bonnie and Sylvia. I must also acknowledge the hard work of every undergraduate and REU student who set foot in our lab, whose contributions significantly enhanced the outcome of this project.

I present this thesis in honor of my wife, without whose patience, love, and support none of this would have been possible.

LIST OF TABLES

2.1	Table of atomic parameters	19
5.1	^{39}K Cooling Parameters	84
5.2	Apparatus comparison	88
6.1	MOT cell coils	90
7.1	Transport System Coils	117

LIST OF FIGURES

1.1	An atom chip and associated support structure	6
2.1	Two Level Atom	8
2.2	Diagram of polarization gradient cooling	16
2.3	Diagram of Magneto-Optical Trapping Principles	17
2.4	Standard D_2 line cooling transitions of ^{87}Rb and ^{39}K	20
2.5	Ballistic expansion of a thermal cloud	29
3.1	Relevant level shifts for trapping 2-level atoms with an RF magnetic near-field	34
3.2	Example of state-selective AC magnetic potentials	37
3.3	Diagram of a traditional atom chip geometry designed for DC magnetic potential trapping	41
3.4	Atom chip fabrication mask	41
3.5	Proposed Transmission Line Chip design for microwave traps.	43
3.6	Profile of B_{rf}^2 above a transmission line trap.	44
3.7	Comparison of AC and DC atom chip microtrap simulations	45
3.8	Vector representation of the effect of roughness.	47
3.9	Roughness defect model	49
3.10	Comparison of μ/RF & DC potential roughness	50
3.11	A vector explanation of potential roughness	51
3.12	Comparison of μ/RF & DC potential roughness	52

3.13	Suppression Factor vs Trap Height and Effective Wavelength	54
4.1	Diagram of the Apparatus	57
4.2	Saturation spectroscopy lock setup	61
4.3	Laser Scheme Block Diagram	63
4.4	Rubidium lock scheme	65
4.5	Potassium Lock Scheme	67
4.6	Double Pass Tapered Amplifier Setup.	69
4.7	MOT coil current and light sequence	70
4.8	Transport System Current Sequence	71
4.9	Atom Chip Z-Wire Layout	72
4.10	Dipole Trapping using the 1W Novawave Fiber Laser	77
5.1	Dual Species Magneto-Optical Trap	79
5.2	Evaporative cooling path to ^{87}Rb BEC	81
5.3	Transition to Quantum Degeneracy	82
5.4	1D Chip MOT of ^{39}K	85
5.5	Diagram of the 1D Chip MOT Technique	86
5.6	Lifetime of the ^{39}K Chip Trap	86
6.1	TIVAR MOT Coil Mount	91
6.2	MOT coil current sequence	94
6.3	Magnetic Switch Circuitry and Photo	96
6.4	Schematic of the Magnetic Switch, Pt 1	97
6.5	Schematic of the Magnetic Switch, Pt 2	101

6.6	Potassium m_f levels in the magnetic trap	103
7.1	Transport System Operation	107
7.2	Multiplexer Block Diagram	116
7.3	Copper and Thermoplastic Transport Mount	118
7.4	Thermal Compound as applied to the Transport System	119
7.5	Thermal Voltage Testing	121
7.6	Transport System Installation mockup	123
7.7	Transport system and associated wiring	124
7.8	Transport System Gradient Testing	125
7.9	Transport system lifetime	126
7.10	Transport and Chip Trap	127
8.1	Energy Levels of ^{39}K	130
8.2	Trap double-pass AOM efficiency	131
8.3	Repumper double pass AOM efficiency	132
8.4	Single Pass Tapered Amplifier Topology	133
8.5	Double Pass Tapered Amplifier Topology	136
8.6	Photo of the Double Pass Tapered Amplifier	137
8.7	MOT Loading and Saturation Rate	139
8.8	^{39}K MOT Loading Rate	140
9.1	Diagram of evaporative cooling	142
9.2	Two level dressed atom description of evaporation cooling	143
9.3	Magnetic sublevels used in microwave and RF evaporation	145

9.4	Diagram of sympathetic evaporative cooling	148
9.5	Diagram of the 6.8 GHz Amplifier	150
9.6	Photo of the 6.8 GHz amplifier	151
9.7	Microwave evaporation at the atom chip	152
9.8	Microwave level cleaning	154
9.9	Adiabatic Rapid Passage	155

ULTRACOLD RUBIDIUM AND POTASSIUM SYSTEM FOR ATOM
CHIP-BASED MICROWAVE AND RF POTENTIALS

CHAPTER 1

Introduction

Production of cold trapped atoms was first motivated by simple scientific wonder and the desire to control the quantum state of the atom. Atomic physics is one of the most well established subfields of modern physics, however it wasn't until the 80's, the 1980's that is, that the first examples of trapped ions and neutral atoms were achieved through meticulous application of atomic laser spectroscopy. Only a decade later, the first demonstrations of Bose-Einstein and Fermi quantum degenerate gases were successfully produced from laser-cooled atoms. These achievements sparked an extensive scientific growth both within the field and out where a broad range of cold atom applications have had far reaching implications for other fields including condensed matter, nuclear physics, statistical mechanics, and fundamental tests of quantum mechanics and symmetry. Recent advancements in the production of cold molecules promises even wider ranging applications as they unlock a potentially limitless set of new quantum gases with their own complicated range of interactions and internal states. As a result, the field of atomic physics is wider and more diverse than ever, with far reaching applications.

The successful production of Bose-Einstein condensation [1, 2, 3] and degener-

ate Fermi gas [4] in ultracold gases marked a shift from the study of single atoms and photons to a focus on particle statistics and interactions [5]. With this new achievement comes the exciting first exploration of many phenomena associated with coherent matter waves, including the interference of two overlapping condensates [6], long range phase coherence [7] and quantized vortices [8] among others. Common to all of these is a coherent, macroscopic matter wave in an interacting many-body system, similar to the classic topics of super conductivity and superfluidity [5]. One key development since the advent of experimental degenerate gases was the ability to tune the interaction strength in cold gases by Feshbach resonance [9]. This allows even extremely dilute gases to enter a regime where they can no longer be described as weakly interacting particles or quasiparticles. Such a phenomenon is characteristic of strongly correlated systems, and for a long time research was confined to the dense, strongly interacting quantum liquids of condensed matter and nuclear physics [5]. Atomic physics persevered however, and this regime was unlocked through the use of Feshbach resonances.

Perhaps even more exciting is the ability to produce and study a true one-dimensional quantum system. Since the inception of quantum mechanics, the one-dimensional (1D) models have fascinated physicists with their elegant and often exact solutions [10]. Often regarded as nothing more than mathematical curiosities or instructional examples, the one-dimensional model which presents such an accessible solution, is easily one of the more difficult systems to implement in the real three-dimensional (3D) world [11]. It might be a personal view, but the allure of producing an experimental system with as few degrees of freedom as possible almost seems *more* challenging, and thus more rewarding.

Often, the engineering physics that goes into an experiment for one field has applications in others. Many of the techniques developed for the production and of ultracold gases can be used to study the phenomena previously reserved for nu-

clear physics. The atomic parity violating weak interaction of francium (Fr) is 18 times larger than that of cesium (Cs), which makes it a wonderful candidate to probe the effects of the weak interaction [12]. Atomic trapping and cooling methods present new ways to study these atoms with precision [13] and bode well for future experiments.

The technology required to produce degenerate quantum gases has since been miniaturized and is slated for a stint on the International Space Station [14]. It is with these great feats in mind that I present this dissertation work both as a record of the past six years working in a dark basement, but also as a testament to all the work that has come before.

The ultimate goal of the Ultracold Atom Group at The College of William & Mary is to develop and demonstrate spatial manipulation techniques of ultracold atoms via microwave and radio-frequency (μ /RF) potentials created on atom chips and leverage these methods to pursue previously out-of-reach physics. This project is an on-going effort by the entire research group. Here I present the theoretical background, design, and simulation efforts pertaining to atom chip μ /RF potentials that will serve as a guide for the group's current and future members to bring these tools to use experimentally.

These potentials arise from the AC Zeeman energy shift experienced by an atom in an applied μ /RF field. μ /RF potentials are inherently spin-dependent and can be used to target independent and qualitatively different trapping potentials to different spin states; furthermore, they can operate at arbitrary magnetic field and so can be used in combination with magnetic Feshbach resonances to tune atom-atom interactions. μ /RF potentials are best generated by an atom chip, a device which produces strong magnetic near-fields from micro-fabricated current carrying wires imprinted on a substrate, as shown in Figure 1.1. The atom chip approach also opens up the possibility of future miniaturization.

The combination of atom chips and hyperfine manipulation is a recent development in atomic physics [15]. Atom chips consist of specialized 2-D electrical wiring patterns on a substrate that can be used to create traps, waveguides, manipulation fields, and detectors. Atoms can be directed very close to the current carrying wires to create strong magnetic field gradients and tight confinement for rapid evaporative and sympathetic cooling. In the near-field regime, the μ /RF structures geometry is set by the configuration of current-carrying wires on the chip and is not limited by the μ /RF wavelength. Chips can support multiple wire geometries on the same substrate, providing experimental flexibility. These μ /RF potentials are ideal for studying many-body physics, creating spin-dependent traps with tunable interactions, and producing interferometers for sensing of inertial forces, gravity, and magnetic fields. A μ /RF-based interferometric sensor implemented compactly on an atom chip has been proposed to be used aboard spacecraft and aircraft to provide inflight navigational feedback, planetary and atmospheric telemetry [16] or even remote magnetic gradient sensing [17, 18].

Although microwave and RF potentials have been previously demonstrated using atom chips [19], μ /RF trapping has yet to be implemented. Applications that would be enhanced through the use of this new technology include interferometry, isothermal phase-space cooling, quantum computation and information, and 1D many-body phenomena, such as spin-charge separation. Quantum information in particular is physical information held in the states of a quantum system, and the spin-dependent forces generated by μ /RF potentials can be used to create quantum gates where the qubit is the spin state of the atom.

The research documented here spans six years of experimental and theoretical work, beginning at a time where the research group had the basic vacuum system, the bulk of the rubidium laser system and a crude MOT before blossoming into the multipurpose research machine described in this dissertation. This dissertation



FIG. 1.1: Atom chip support structure prior to being installed under vacuum. The substrate is approximately 1 sq. in. Multi-layer metallic wires were photo-lithographically produced by photo-lithography on an aluminum-nitride substrate by D. Jervis of the Thywissen group at University of Toronto.

begins with a review of basic atomic physics in Chapter 2 as it pertains to optical and magnetic forces before stepping through a discussion of the AC Zeeman shift, atoms chips and the predicted suppression of potential roughness. Chapter 4 explains the details of our dual species apparatus as built and the following chapter summarizes the performance and capabilities of the system. The final four chapters describe in detail the key systems I was responsible for during my tenure including the magnetic trapping, magnetic transport, potassium laser cooling, and microwave evaporation systems. Throughout the document, vectors are represented with arrows (\vec{v}), whereas operators appear in bold (**S**).

CHAPTER 2

Ultracold Atom Theory

In this chapter I present a necessary theoretical background of the main atomic processes that form the basis of this dissertation work. Starting from the canonical two level atom, I will first develop the scattering and dipole forces present between a laser and atom, before moving on to discuss their uses in Doppler cooling, magneto-optical trapping, optical pumping, and dipole trapping. This derivation is modeled on the great example of Metcalf and Van der Straten [20], invoking the work of Tammuz [21] and Landini [22] for clarity along the way. Finally, a discussion of the magnetic Zeeman shift and how it can be used to generate magnetic potentials for atomic trapping and manipulation, pulling from several additional examples including Metzkes [23] and Yoon [24].

2.1 A Two Level Atom

Perhaps the simplest atomic system is that of the two level atom, first explored by Rabi in connection with magnetic resonance [25]. Picture a system with ground state $|g\rangle$ and excited state $|e\rangle$, separated by an energy $\hbar\omega_{eg}$. These states become coupled by the application of a laser field at frequency ω_l , detuned by δ from the

atomic separation. This configuration is laid out in Figure 2.1.

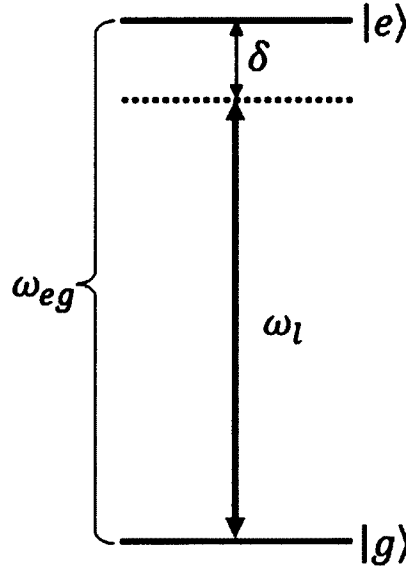


FIG. 2.1: The simplest case of the two-level atom with ground and excited states $|g\rangle$ and $|e\rangle$ separated by energy $\hbar\omega_{eg}$. A laser field of frequency ω_l is coupled to the system, detuned from the atomic separation by detuning $\delta = \omega_l - \omega_{eg}$.

2.2 Optical Potentials

Atomic interactions with an externally applied electromagnetic field can be described as a combination of three discrete processes, the combination of which results in the total force felt by the atoms. These processes are the absorption, spontaneous emission, and stimulated emission of photons back and forth to the radiation field. The first two processes result in what is known as the *scattering* or *radiation* force while the last process results in a dispersive force known as the *dipole* force. These two forces can be treated separately with very different uses in the trapping and cooling of atoms. The scattering force is used for laser cooling and magneto-optical trapping as the backbone of ultracold atomic experiments. The dipole force is typically used as a final destination or *science* trap much like

magnetic trapping where its tight confinement and conservative potential is ideal for evaporative cooling techniques.

For the two-level atom in an external plane-wave electric field propagating in the \hat{z} direction, an interaction exists between the field and the induced dipole moment of the atom, $-e\vec{r}$, where \vec{r} is in the direction of the induced dipole and e is the charge of the electron in Coulombs. The Hamiltonian of this system is

$$\mathcal{H}(t) = -e\vec{\mathcal{E}}(\vec{r}, t) \cdot \vec{r} \quad (2.1)$$

where $\vec{\mathcal{E}}(\vec{r}, t)$ is the operator of the electric field and $e\vec{r}$ is the dipole moment operator [21, 20]. An oscillating electric field traveling in the \hat{z} direction is given by $\vec{\mathcal{E}}(\vec{r}, t) = E_0\hat{e}\cos(kz - \omega_1 t)$ where \hat{e} is the unit polarization vector and E_0 is the amplitude of the light field. The coupling term of the Hamiltonian becomes $\mathcal{H}'_{eg}(t) = \hbar\Omega\cos(kz - \omega_1 t)$ where Ω is known as the Rabi frequency, defined as

$$\Omega \equiv \frac{-eE_0}{\hbar} \langle e|r|g \rangle. \quad (2.2)$$

The Ehrenfest theorem will then give the force F_z along the propagation axis of the plane-wave field \hat{z} from the quantum mechanical expectation value of the spatial derivative of the Hamiltonian [20, 21], following the form

$$F_z = -\left\langle \frac{\partial \mathcal{H}}{\partial z} \right\rangle = e \left\langle \frac{\partial}{\partial z} (\vec{\mathcal{E}}(\vec{r}, t) \cdot \vec{r}) \right\rangle. \quad (2.3)$$

Assuming a regime where $\lambda \gg |r|$, the derivative and expectation value can be interchanged, resulting in

$$F_z = e \frac{\partial}{\partial z} \langle (\vec{\mathcal{E}}(\vec{r}, t) \cdot \vec{r}) \rangle. \quad (2.4)$$

Although the atom has no dipole moment in an eigenstate of the base Hamil-

tonian ($\langle g|\vec{r}|g\rangle = \langle e|\vec{r}|e\rangle = 0$), the presence of the electric field E_0 mixes $|g\rangle$ and $|e\rangle$. The dipole operator can be rewritten as

$$\begin{aligned}\vec{r} &= \vec{r}_{eg}|e\rangle\langle g| + \vec{r}_{eg}^*|g\rangle\langle e| \\ \langle \vec{r} \rangle &= \text{tr}(\rho \vec{r}) = \vec{r}_{eg}\rho_{eg} + \vec{r}_{eg}^*\rho_{eg}^*\end{aligned}\quad (2.5)$$

where ρ_{eg} is the off-diagonal density matrix element of $\rho = |\Psi\rangle\langle\Psi|$ [20, 21]. With this in hand, Equation 2.4 can now be written as

$$F_z = \hbar \left(\frac{\partial \Omega}{\partial z} \rho_{eg}^* + \frac{\partial \Omega^*}{\partial z} \rho_{eg} \right) \quad (2.6)$$

assuming that the rotating-wave approximation is valid, where $\delta \equiv \omega_l - \omega_{eg} \ll \omega_l + \omega_{eg}$. By separating the derivative of the Rabi frequency into real and imaginary components

$$\frac{\partial \Omega}{\partial z} = (q_r + iq_i)\Omega, \quad (2.7)$$

where $q_r + iq_i$ is the logarithmic derivative of Ω . Equation 2.6 can be reduced to

$$F_z = \hbar q_r (\Omega \rho_{eg}^* + \Omega^* \rho_{eg}) + i \hbar q_i (\Omega \rho_{eg}^* - \Omega^* \rho_{eg}) = \frac{\hbar s}{1+s} \left(-\delta q_r + \frac{1}{2} \Gamma q_i \right) \quad (2.8)$$

where $\delta = \omega_L - \omega_0$ is the field detuning from the transition frequency [20, 21] and ρ_{eg} can be written

$$\rho_{eg} = \frac{i\Omega}{2(\Gamma/2 - i\delta)(1+s)}, \quad (2.9)$$

where s is the saturation parameter as defined by

$$s \equiv \frac{s_0}{1 + (2\delta/\Gamma)^2} \quad (2.10)$$

and

$$s_0 \equiv \frac{2\Omega^2}{\Gamma^2} = \frac{I}{I_s}, I_s \equiv \frac{\pi\hbar c}{3\lambda_0^3\tau} \quad (2.11)$$

where λ_0 is the resonance wavelength, c is the speed of light, and $\tau = 1/\Gamma$ is the transition lifetime [22, 20]. The *saturation intensity*, I_s , is the intensity at which the scattering rate is half of its maximum value (1/4 of the atoms are in the excited state). The intensity I is related to the electric field by $I = \epsilon_0 c E_0^2/2$ where E_0 is the amplitude of the electric field. The rotating wave approximation invoked earlier allows the field to be written as $\mathcal{E}(\vec{r}, t) = E_0 e^{ikr}$. Substituting this into Equation 2.2 and combining it with Equation 2.7 results in [21]

$$\frac{\partial\Omega}{\partial z} = \frac{e}{\hbar} \langle e|r|g \rangle \frac{\partial E_0}{\partial z} e^{ikr} + i \frac{e}{\hbar} k_z E_0 \langle e|r|g \rangle e^{ikr}. \quad (2.12)$$

Employing the definitions of Equation 2.11, this expression reduces to

$$\frac{\partial\Omega}{\partial z} = \frac{1}{2s_0} \frac{\partial s_0}{\partial z} \Omega + ik\Omega = q_r \Omega + iq_i \Omega \quad (2.13)$$

and thus we have come full circle to the realization that

$$q_r = \frac{1}{2s_0} \frac{\partial s_0}{\partial z}, q_i = k. \quad (2.14)$$

Substituting these new definitions into Equation 2.8 gives the total force which is generalized to three dimensions [21] exchanging the partial derivatives with the gradient in the form

$$\begin{aligned} \vec{F}_{total} &= -\frac{\hbar\delta}{2} \frac{\nabla(I/I_s)}{1 + I/I_s + (2\delta/\Gamma)^2} + \frac{\Gamma}{2} \frac{I/I_s}{1 + I/I_s + (2\delta/\Gamma)^2} \hbar\vec{k} \\ &= \vec{F}_{dipole} + \vec{F}_{scattering} \end{aligned} \quad (2.15)$$

from which one can see that the scattering force is proportional to electric field

intensity, I , while dipole force is proportion to the gradient of I . In the large detuning regime of $|\delta| \gg \Gamma$, the dipole force can be rewritten as the derivative of the AC Stark shift [21]

$$\vec{F}_{dipole} = -\nabla U_{dipole} \simeq -\nabla \left(\frac{\hbar\Omega^2}{4\delta} \right). \quad (2.16)$$

A spatially dependent intensity gives rise to a net force felt by the atoms that is inversely proportional to the detuning δ , that is, a negative or *red* detuning results in a positive force drawing atoms to the areas of highest intensity. In the opposite case, a positive or *blue* detuned field draws atoms to the regions of lowest intensity. On resonance ($\delta = 0$), the dipole force vanishes.

As the scattering force arises from the absorption of photons from the applied field, it could be alternately derived from the equivalence of force and the rate of change of momentum. A closer look at Equation 2.15 reveals that scattering force is of the form $\vec{F}_{scattering} = \hbar\vec{k} \cdot R_{scattering}$ where the scattering rate is given to be [20]

$$R_{scattering} = \frac{\Gamma}{2} \cdot \frac{I/I_s}{1 + I/I_s + (2\delta/\Gamma)^2}. \quad (2.17)$$

The scattering force as it is used for laser cooling and trapping will be discussed in the following two subsections.

2.2.1 Doppler Cooling

As hinted above, laser cooling is based on a deliberate transfer of momentum from a propagating electric field plane wave. With each photon absorption, the photon's linear momentum, $\hbar\vec{k}$, is transferred to the atom along with its angular momentum \hbar and energy $\hbar\omega$, the latter of which excites the atom to a higher energy state. The subsequent recoil and spontaneous emission is spatially symmetric and

thus averages to zero over many absorption and emission events. The net force on the atom is in the direction of the light propagation, and magnitude of the force is given by the single-photon momentum transfer, $\hbar\vec{k}$, and the photon scattering rate, $R_{scattering}$, as shown in Equation 2.17. In laser cooling, small detunings are employed where $|\delta| \approx \Gamma$, ensuring that the dipole force is negligible. The distance over which the beam intensity varies is kept large compared to the wavelength $|\nabla I| \ll kI$, and thus the Doppler effect is used to create a velocity-dependence over a distribution of atoms. An atom in motion with velocity \vec{v} experiences a Doppler shift of $\vec{k} \cdot \vec{v}$. In Doppler cooling the total detuning is

$$\delta_{Doppler}^{\pm} = \delta \mp \vec{k} \cdot \vec{v} \quad (2.18)$$

where δ^+ describes atoms moving into the incident laser beam at velocity v and δ^- describes those moving away. Consider two counter propagating beams of intensity I and frequency ω . The total force exerted on an atom with velocity v is then given by [21, 20]

$$\begin{aligned} F_{Total}(v) &= F_+ + F_- \\ &= \hbar k \frac{\Gamma}{2} \left(\frac{1}{1 + I/I_s + (2\delta_{Doppler}^+/\Gamma)^2} - \frac{1}{1 + I/I_s + (2\delta_{Doppler}^-/\Gamma)^2} \right) \frac{I}{I_s} \end{aligned} \quad (2.19)$$

where the relative negative sign comes from the wavevectors of the counterpropagating beams. In the small-velocity limit where $v \ll \delta/k$, the velocity dependence becomes more obvious when the total force is expanded to first order in v [21, 20]

$$F_{Total}(v) \approx \frac{4\hbar k^2(I/I_s)(2\delta/\Gamma)}{(1 + I/I_s + (2\delta/\Gamma)^2)^2} v \equiv -\beta v. \quad (2.20)$$

With a red-detuned beam ($\delta < 0$), the Doppler force acts as a damping force, opposing the atomic motion, hence the term *optical molasses*. The laser configuration is

easily generalized to three dimensions by adding two additional pairs of orthogonal counter-propagating beams.

Doppler Cooling Limit

An important aspect of laser cooling is the point at which the Doppler cooling is balanced by the heating of the discrete recoils of the spontaneous emission process. Assuming a regime below saturation where $I/I_s \ll 1$, an energy of $\hbar\omega_r$ is transferred with each scattering event where the recoil energy or $\hbar\omega_r = \hbar^2 k^2 / 2m$ [21, 22]. One single absorption and re-emission event results in a total energy transferred to the atom of $\hbar\omega_r$, at a rate of $R_{scattering}$. Taking the opposing beam into account, the energy transfer becomes $2\hbar\omega_r$, at a rate of $2R_{scattering}$. The heating rate is then $4\hbar\omega_r R_{scattering}$ and is balanced by the cooling rate $\vec{F}_{Total} \cdot \vec{v}_x$ where \vec{F}_{Total} is given by Equations 2.19 and 2.20. This results in the expression for the steady-state kinetic energy [20]

$$E_{kinetic} = -\frac{\hbar\Gamma}{8} \left(\frac{2|\delta|}{\Gamma} + \frac{\Gamma}{2|\delta|} \right) = \frac{1}{2} m \overline{v_x^2}. \quad (2.21)$$

Kinetic energy of a gas can also be represented using temperature, such as $\frac{1}{2} k_B T$. Equating this with Equation 2.21, the expression can be minimized with respect to the detuning δ , yielding the Doppler temperature to be [20]

$$T_D = \frac{\hbar\Gamma}{2k_B} \quad (2.22)$$

which occurs at the minimization condition of $\delta = -\Gamma/2$. This corresponds to a minimum velocity of $v_D = \sqrt{k_B T_D / m}$. Fortunately for atomic experimentalists, sub-doppler cooling is often available for free, depending on the specific hyperfine structure of the atom in question.

2.2.2 Sub-Doppler Cooling

Sub-Doppler cooling, is a technique that achieves a final temperature below the Doppler limit, at the cost of trapping. Optical molasses is usually performed without much effort, simply turning off the quadrupole field of the MOT coil pair and turning on the three pairs of counter-propagating cooling beams. The detuning is usually increased to reduce the scattering rate. The explanation presented here is intentionally kept brief as sub-Doppler cooling was not studied in depth.

The counter propagating laser cooling beams have circular polarization which combine to create a spatially-varying polarization gradient formed from the standing wave. As an atom moves along the axis of a cooling beam, the polarization of the light varies from σ^+ to linear to σ^- to \perp and so on. Depicted in Figure 2.2 atoms in the spin $+1/2$ state travel “uphill” to regions of σ^+ light where they are shifted closer to resonance by the Stark shift of the optical beam. They are then optically pumped to the spin $-1/2$ ground state via the cooling light. During spontaneous emission back to the ground state, atoms emits a higher energy photon than it absorbed, as the spin $-1/2$ state is Stark shifted farther away. This cycle repeats at the spin $-1/2$ atom next enters a σ^- region of the beam [20]. This configuration is usually referred to as polarization-gradient cooling or Sisyphus cooling.

The tight hyperfine structure of ^{39}K complicates the sub-doppler cooling processes as multiple nearby transitions affect the cycle, a process explored in great detail by Landini et al [22]. Their results became the starting point for a sweeping MOT technique described in Chapter 4.

2.2.3 Magneto-Optical Trapping

While Doppler cooling is an effective and efficient cooling mechanism, it cannot confine the atoms and prevent their diffusion out of the beam overlap region. In

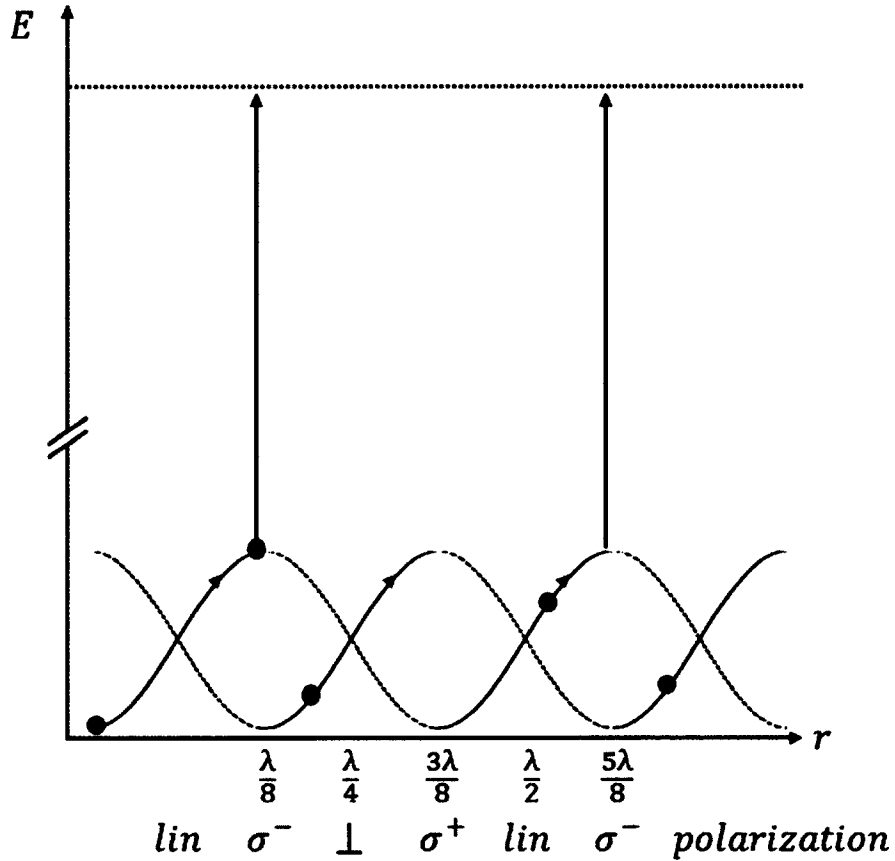


FIG. 2.2: The spatial dependence of the light shifts in the ground state sublevels of the $J = 1/2 \rightarrow 3/2$ transition in the $\text{lin} \perp \text{lin}$ polarization configuration. The arrows represent the path that atoms follow as they are being cooled. Atoms must climb the potential hill as they approach a point where light becomes σ^\pm polarized, from which they are then optically pumped into the opposite ground state via the cooling light. From there the atoms begin climbing another hill. The black arrow represents an absorption transition whereas the orange arrow represents spontaneous emission. The process repeats until the atomic kinetic energy is too low to climb the next hill. Each optical pumping event results in absorption of light at a lower frequency than the subsequent emission, dissipating energy into the radiation field.

order to create a spatially-dependent force, the Zeeman shift of magnetic sublevels can be exploited to create what is known as a *magneto-optical trap* or MOT.

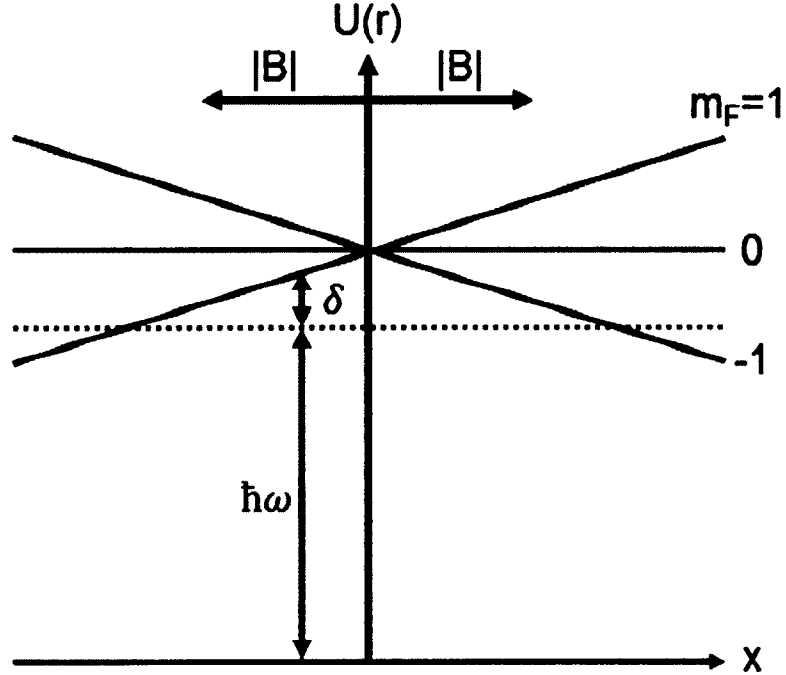


FIG. 2.3: A Diagram of Magneto-Optical Trapping Principles. Three Zeeman magnetic sublevels are shown in a qualitative representation of their relative splittings. The applied cooling field $\hbar\omega$ has a spatially varying detuning γ .

Consider for a moment an ideal two-level system with $F = 0$ ground state and $F = 1$ excited state in a linearly varying one-dimensional magnetic field; the magnetic field breaks the degeneracy of the excited state Zeeman sublevels, $m_F = -1, 0, +1$. Two counter-propagating beams are introduced with opposing circular polarization, red-detuned from the atomic transition. The circular polarization forbids any transitions other than $\Delta m_F = \pm 1$ for σ^\pm , respectively. The allowed transitions are forced closer to resonance when atoms stray from the magnetic minimum towards either beam. The oppositely polarized beam is shifted further from resonance because of the atom's location [21]. A linearly varying magnetic field such

as this is easily reproduced in three dimensions using a pair of anti-helmholtz coils to create a quadrupole field with gradient B'_0 of the form $\vec{B} = \vec{B}'_0(x, y, -2z)$. The combined detuning for the entire system can be described as [21]

$$\delta_{MOT}^{\pm} = \delta_{Doppler}^{\pm} \pm (g_e m_e - g_g m_g) \frac{\mu_B B'_x}{\hbar} = \delta \mp \vec{k} \cdot \vec{v} \pm \alpha|x| \quad (2.23)$$

where μ is the atomic magnetic moment and subscripts g and e represent the ground and excited states. The third term is the detuning introduced by the Zeeman shift, $U = -\mu \cdot \vec{B}$ (note: $\mu_B/h \approx 1.4$ MHz/G).

At this point, the scattering force has been given a position-dependence in addition to the aforementioned Doppler cooling velocity-dependence. Again in the regime of low-velocity but now within a weak magnetic field condition ($v \ll \delta/k$ and $B \ll \hbar\delta/\mu_B$), Equation 2.19 is again expanded to first order in v but with the inclusion of the detunings of Equation 2.23. This results in the following expression [21]

$$F_{Total}(x, v) \approx \frac{4\hbar k(I/I_s)(2\delta/\Gamma)}{(1 + I/I_s + (2\delta/\Gamma)^2)^2} (kv + \alpha x) \equiv -\beta v - \kappa x \quad (2.24)$$

where κ represents the spring constant $\alpha\beta/k$. This system can now be describe via the equation of motion [21]

$$\ddot{x} + \gamma_{MOT}\dot{x} + \omega_{MOT}^2 x = 0. \quad (2.25)$$

This is more commonly known as a damped harmonic oscillator of mass m with damping coefficient $\gamma_{MOT} = \beta/m$ and effective oscillation frequency $\omega_{MOT} = \sqrt{\kappa/m}$. The specifics of how the MOT is applied to rubidium and potassium systems is discussed in subsection 2.3.

2.2.4 Practical Laser Cooling

	$\Gamma/2\pi$	λ	v_r	T_D	I_s	τ
^{87}Rb	6[20]	780.24[20]	5.8845[26]	146[26]	1.67[26]	26.23 [26]
^{39}K	6.1[20]	766.70[20]	13.35[27]	145[20]	1.75 [27]	26.37 [27]
units	MHz	nm	mm/s	μK	mW/cm^2	ns

TABLE 2.1: Table of atomic parameters for ^{87}Rb and ^{39}K . Γ is the natural linewidth, λ is the wavelength of the transition. v_r is the recoil velocity, T_D is the Doppler temperature and I_s is the saturation intensity. τ is the lifetime, also known as $1/\Gamma$.

Although ideal two-level theory of laser cooling is far less complicated than actual atomic electronic level structures, the single valence electron of alkali metals make for convenient cooling targets. More recently, advancements have been made to laser cool non-alkali atomic species such as calcium, strontium, argon, krypton, magnesium and ytterbium among others.

Two bosonic species are the focus of this thesis: the canonical ^{87}Rb and the similar but finicky ^{39}K . Laser cooling of these isotopes uses the D_2 transitions. The natural linewidth of the D_2 line of both species are approximately $\Gamma = 2\pi \times 6\text{MHz}$, which corresponds to an excited state lifetime of $\tau = 1/\Gamma = 26\text{ns}$. The ground state is split into $|F = 1\rangle$ and $|F = 2\rangle$ where the excited states feature four hyperfine levels $|F' = 0, 1, 2, 3\rangle$. For both species, the two-level system cooling transition is the $nS_{1/2}|F = 2\rangle \rightarrow nP_{3/2}|F' = 3\rangle$ transition where $n = 4(5)$ for K(Rb).

The selection rule of $\Delta F = 0, \pm 1$ restricts decay from the excited state of $|F' = 3\rangle$ solely to the $|F = 2\rangle$ ground state. The cooling laser can cause the occasional excitation from $|F = 2\rangle$ to $|F' = 2\rangle$ where decay to the dark ground state $|F = 1\rangle$ is allowed, atoms will eventually accumulate. This problem is solved by the introduction of a *repump* beam that is tuned on resonance with the $nS_{1/2}|F = 1\rangle \rightarrow nP_{3/2}|F' = 2\rangle$ transition, again where $n = 4(5)$ for K(Rb). The atoms then have a chance to decay back to $nS_{1/2}|F = 2\rangle$ state. The repumper beam is represented in

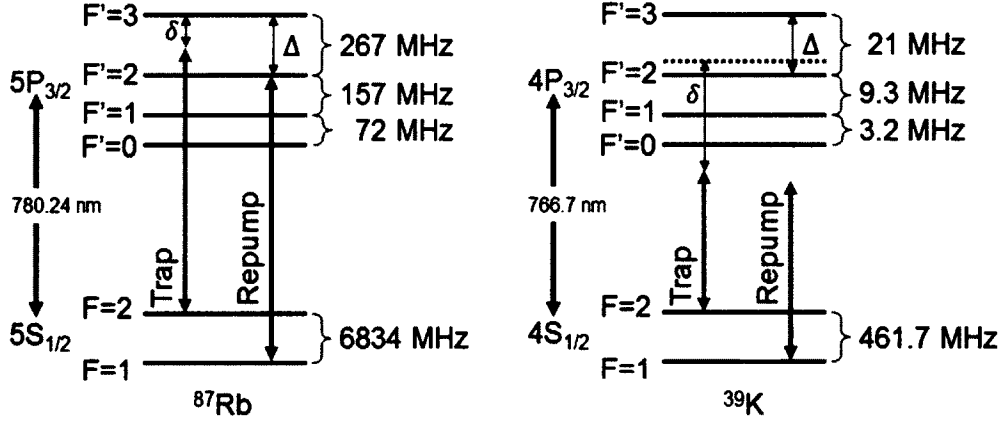


FIG. 2.4: Traditionally leveraged cooling transitions of ^{87}Rb and ^{39}K . In ^{87}Rb , the trapping or cooling light is detuned from the $|F = 2\rangle$ to $|F' = 3\rangle$ in a regime where the detuning δ is much less than the adjacent hyperfine splitting of Δ . ^{39}K presents an interesting case where the trap is traditionally detuned from the entire $4P_{3/2}$ hyperfine manifold represented by the dotted line, since the hyperfine states are closely spaced.

blue in Figure 2.4.

The narrow hyperfine manifold of the ^{39}K excited state complicates the system. Traditionally in ^{39}K , the trap and repumper beams are detuned from the entire excited hyperfine manifold as shown in Figure 2.4. This compromise results in two significant consequences, namely the need for a much more intense repumper beam and a lack of effective sub-Doppler cooling mechanism.

The more closely spaced excited-state hyperfine manifold results in more excitations to the $F' = 2, 1$ levels, resulting in a stronger decay path into the dark $nS_{1/2}|F = 1\rangle$ ground state. This closely spaced manifold remains unresolved in a vapor cell with saturation spectroscopy; however, in our MOT, the $F' = 3, 2$ levels were successfully resolved. This feature necessitates the need for a repumper with similar intensity to that of the trap light, to prevent accumulation of dark state atoms. The pumping is so strong that the contribution of the repumper to the

cooling process is non-negligible, and the use of these names is purely a historical convention. Typically both the trap and repumper beams are red-detuned from the entire excited state manifold where historically the largest capture velocity is achieved [28, 29, 30, 31, 32, 33].

The red-detuning of both beams from the closely spaced excited ^{39}K hyperfine manifold results in little-to-no sub-Doppler cooling force. Under these conditions, typical MOT and optical molasses techniques result in temperatures on the order of 1 mK. As a general rule of thumb, the sub-Doppler cooling mechanisms are only efficient when the excited-state hyperfine splitting is much bigger than the natural linewidth Γ , such is the case with Rb, Na, & Cs or smaller than Γ , as in Sr. In ^{39}K and ^{41}K , the excited-state hyperfine splitting is on the order of Γ ; as a result, the sub-Doppler cooling process is impeded by heating forces and resonant photon reabsorption. Nevertheless, it has been demonstrated both theoretically and experimentally by Landini et al [22] that sub-Doppler cooling is possible with a clever adaptation of the traditional cooling parameters. This approach still leverages an initial Doppler cooling stage where both repumper and trap are detuned below the entire excited state manifold. This is followed by an optical molasses stage with a significant reduction in detuning and intensity of both beams, resulting in final temperatures of approximately $30\mu\text{K}$, [34, 35]. This thesis work follows a similar approach adapted to the MOT operation to attain comparable temperatures with lower available power and intentionally without molasses as described in Chapter 8.

2.2.5 Optical Pumping

Following the MOT and optical molasses techniques, the atoms are distributed into all available magnetic Zeeman sublevels of the $|F = 2\rangle$ ground state. While some of these spin states are magnetically trappable, others are anti-trapped or

magnetically neutral. In order to secure the highest atom number yield in the magnetic trap, the atomic cloud must be spin-polarized to ensure that as much of the population is magnetically trappable. To create this effect, a uniform magnetic field on the order of 1 G is applied to define a quantization axis but not so strong as to shift the atoms out of resonance with the lasers. The atoms are illuminated by resonant $nS_{1/2}|F = 2\rangle \rightarrow nP_{3/2}|F' = 2\rangle$ light with σ^+ circular polarization along the quantization axis. The repumper usually remains on to some extent, resonant with the $nS_{1/2}|F = 1\rangle \rightarrow nP_{3/2}|F' = 2\rangle$ transition, where $n = 4(5)$ for K(Rb).

Transitions driven by σ^+ circular polarized light are subject to the selection rule of $\Delta m_F = +1$, in other words,

$$nS_{1/2}|F = 2, m_F\rangle \rightarrow nP_{3/2}|F' = 2, m_F + 1\rangle. \quad (2.26)$$

The resulting spontaneous decay to the ground state follows a broader selection rule of $\Delta m_F = 0, \pm 1$; with decay path probability governed by the Clebsch-Gordan coefficients [21]. The repump light ensures that any atoms that decay to the dark ground state of $|F = 1\rangle$ are transferred back to $|F' = 2\rangle$ and kept in the pumping cycle. After enough cycles of absorption and emission, all atoms end up in the $|F = 2, m_F = 2\rangle$ ground state where they go dark.

This technique is crucial not only to maximize the number of initially trapped atoms but also to minimize atom loss and heating caused by collisions between atoms in different magnetic sublevels. This is even more important in a system such as ours where interspecies collisions will be used for the sympathetic cooling of ^{39}K . It is sometimes necessary to make extra efforts to remove unwanted $|F = 1, m_F = -1\rangle$ and $|F = 2, m_F = 1\rangle$ atoms from the atomic cloud to further suppress the detrimental collisions associated with their presence. The target state of $|F = 2, m_F = 2\rangle$ also represents the tightest magnetic confinement for the highest possible

collision rate for efficient evaporative cooling.

2.2.6 Optical Dipole Traps

This subsection takes a closer look at the optical dipole force defined in Equation 2.15, which may dominate at large laser detuning when the scattering force is weak. An optical gradient can be used to create a trapping potential analogous to the magnetic case. Certain experiments and atomic phenomena either require or benefit from a non-magnetic trapping potential including most many body physics experiments such as magnetic Feshbach resonance studies of Anderson Localization [36, 37] and some forms of atom interferometry [38]. Optical dipole traps can provide tight confinement and evaporative cooling, often as the last step to degeneracy in an experiment. Equation 2.15 describes the conservative optical dipole force as an interaction between the induced dipole and the light field intensity gradient. By integrating the expression in Equation 2.15, we obtain the optical dipole potential [21]

$$\begin{aligned}
U_{dipole}(\vec{r}) &= - \int \vec{F}_{dipole} \cdot d\vec{r} \quad \text{with} \quad \vec{F}_{dipole} = -\frac{\hbar\delta}{2} \cdot \frac{\nabla(I/I_s)}{1 + I/I_s + (2\delta/\Gamma)^2} \\
&= \frac{\hbar\delta}{2} \ln(1 + I/I_s + (2\delta/\Gamma)^2) + C_1 \\
&= \frac{\hbar\delta}{2} \ln(1 + (I/I_s + 1)/(2\delta/\Gamma)^2) + C_2 \\
&= \frac{\hbar\delta}{2} \left((1 + (I/I_s + 1)/(2\delta/\Gamma)^2) - \frac{(1 + (I/I_s + 1)/(2\delta/\Gamma)^2)^2}{2} + \dots \right) \\
&\approx \frac{\hbar\delta}{2} \frac{\Gamma^2}{(2\delta)^2} \frac{I}{I_s} \quad \left(\frac{\delta}{\Gamma} \right)^2 \gg \frac{I}{I_s} \\
&= \frac{3\pi c^2 \Gamma}{2\omega_0^3} \frac{I(\vec{r})}{\delta}
\end{aligned} \tag{2.27}$$

where ω_0 is the transition frequency, assuming a large detuning and low intensity. Integration constants have been cast aside and the natural log has been expanded using the Taylor series, keeping only the first term. The definition of $I_S \equiv \pi\hbar c/3\lambda_0^3\tau$ from Equation 2.11 has been invoked while discarding terms of order higher than $(\frac{2\delta}{\Gamma})^{-2}$. Additionally within the limit of large-detuning, the scattering rate from Equation 2.17 reduces to

$$R_{scattering}(\vec{r}) = \frac{3\pi c^2}{2\hbar\omega_0^3} \left(\frac{\Gamma}{\delta}\right)^2 I(\vec{r}). \quad (2.28)$$

It is now apparent that red-detuned ($\delta < 0$) far off resonant light results in a negative or *attractive* potential where atoms are drawn to the most intense regions of light. Blue-detuning ($\delta > 0$) draws atoms to regions of low-intensity. One can also see now that the potential depth scales as I/δ while the scattering rate goes as I/δ^2 , which is why dipole traps typically use high intensity beams with large detunings to create deep potentials while keeping scattering in check.

A common experimental technique used to increase the confinement involves two intersecting non-parallel red-detuned beams also known as a *crossed-dipole trap*. Periodic lattices can be generated through standing wave interference of counter-propagating beams of red or blue-detuned light and easily extended to multiple dimensions.

2.3 Magnetic Potentials

A magnetic field can be used to produce a conservative magnetic potential that operates without the use of photon absorption, thus allowing atoms to be effectively cooled below the recoil limit. As all atoms with a non-zero magnetic dipole moment in an applied magnetic field gradient will experience a Zeeman shift,

a conservative trapping potential can be engineered to efficiently hold the atoms with an appropriate magnetic field.

This section follows the excellent example of Cohen-Tannoudji for the details [39]. An atom in the presence of a local static magnetic field $\vec{B} = |\vec{B}_z|\hat{z}$ experiences an energy shift given by

$$\mathcal{H} = -\vec{\mu} \cdot \vec{B} = \frac{\mu_B}{\hbar}(g_S\mathbf{S}_z + g_L\mathbf{L}_z + g_I\mathbf{I}_z) \cdot B_z \quad (2.29)$$

where μ_B is the Bohr magneton and B_z is the magnetic component along the quantization axis, z . S_z, L_z and I_z are the z -component operators of spin, orbital and nuclear angular momenta, respectively with corresponding Landé g -factors, g_S, g_L and g_I . This g -factor depends on the total angular momentum state of $|n, L, I, S, J, F\rangle$ where n is the principle quantum number, L is the orbital angular momentum, I is nuclear angular moment, S is the electron spin, and J is the electronic angular momentum. In the low magnetic field limit, this energy shift is small compared to the hyperfine splitting [21], thus

$$\mathcal{H}_{hfs} = A_{afs}\mathbf{I} \cdot \mathbf{J} \Rightarrow \mathcal{E}_{afs} = [F(F+1) - I(I+1) - J(J+1)] \quad (2.30)$$

due to the electronic and nuclear momenta coupling. In this instance, the good quantum numbers are $\mathbf{F} = \mathbf{I} + \mathbf{J}$ and m_F . A_{afs} is the hyperfine A coefficient, accepted as $h \cdot 3.415$ GHz for ^{87}Rb [26] and $h \cdot 230.86$ MHz for ^{39}K [27], and \mathcal{E}_{afs} represents the associated energy. With this in hand, Equation 2.29 can be rewritten as

$$\mathcal{H}_B = \mu_B g_F \mathbf{F}_z \cdot \vec{B}_z. \quad (2.31)$$

This Landé g-factor can be calculated as [20]

$$g_F = \left(\frac{F(F+1) + J(J+1) - I(I+1)}{2F(F+1)} \right) \left(1 + \frac{J(J+1) + S(S+1) - L(L-1)}{2J(J+1)} \right) \quad (2.32)$$

where $F \in [J - I, J + I]$ and $J \in [L - S, L + S]$. This leads us to see that the Zeeman energy shift is linear with the applied magnetic field strength, for a given $|F, m_f\rangle$ state

$$U(\vec{r})_{|F, m_F\rangle} = -\vec{\mu} \cdot \vec{B}(\vec{r}) = \mu_B g_F m_F |B_z|. \quad (2.33)$$

The force experience by an atom in this potential is given by

$$F(\vec{r}) = -\nabla U(\vec{r}) = -\mu_B g_F m_F \nabla |B_z| \quad (2.34)$$

Equation 2.33 illustrates that any states with $g_F m_F > 0$ can lower their energy by seeking the low-field or magnetic minima. States with $g_F m_F < 0$ then become the high-field seekers. As free space magnetic maxima are forbidden by Maxwell's equations, these high-field seeking states are always anti-trapped and thus, magnetic traps are always created around a local magnetic minimum [40, 41]. The ground state Landé factors of ^{87}Rb and ^{39}K are $g_{F=1} = -1/2$ and $g_{F=2} = 1/2$, thus the trappable states are $|F = 1, m_F = -1\rangle$, $|F = 2, m_F = 1\rangle$ and $|F = 2, m_F = 2\rangle$.

Classically, the magnetic dipole moment precesses around the local external magnetic field at the Larmor frequency, $\omega_L = \mu B / \hbar$. If the direction of the external field changes slowly with respect to ω_L , the moment will follow the field direction adiabatically. Quantum mechanically, the atom remains in the same $|F, m_f\rangle$ state. This can be mathematically expressed as [20, 21]

$$\omega_L \gg \frac{|\mathbf{v} \cdot \nabla \vec{B}|}{B} \quad (2.35)$$

a condition that is easily satisfied by the low velocity \vec{v} of ultracold atoms. However, it is easily seen from Equation 2.35 that when the magnetic field is very low, this condition can easily be violated. Atoms that possess enough kinetic energy will experience a rapidly changing field, enough to transition to another m_F state, a process known as Majorana spin flipping.

2.3.1 Magnetic Trapping

A quadrupole trap, such as that described in the MOT of subsection 2.2.3, is one such field configuration that will result in a magnetic minimum where magnitude increases in every direction. For any field to provide efficient magnetic confinement, the atoms must be low enough in temperature that the trap provides an effective barrier in all directions, and the Zeeman force must be strong enough to hold the atoms against the force of gravity.

Should the trapping field become sufficiently weak that Majorana spin flips occur, atoms can transition to a variety of states that are anti-trapped (i.e. $g_F m_f < 0$) or untrappable (i.e. $g_F m_f = 0$). In this instance, the atoms are immediately lost from the trap in a process known as Majorana losses [42, 43]. This mechanism is a particular concern in trap geometries that feature a magnetic zero point since this is also where the coldest atoms collect. Majorana spin flips also heat the remaining trapped atoms, preventing the atomic cloud from cooling to quantum degeneracy [44, 45]. If the atom cloud is not too cold, the probability for an atom to traverse the zero region is small, so the Majorana loss rate is typically smaller than the vacuum loss rate. While the common quadrupole trap has a magnetic zero, other trap geometries, such as the Ioffe-Pritchard trap, and others generated with atom chips can achieve confinement with a non-zero minimum.

2.4 Temperature and Phase-Space Density

The motivation for the techniques described in this chapter is all about producing ultracold atomic samples with the best possible combination of atom density and temperature, or what is commonly known as the phase-space density (PSD) of the trapped atoms. Attaining the highest possible phase-space densities in any magnetic, optical or hybrid trapping system is an important first step in the production and observation of collective quantum effects such as Bose-Einstein condensates and degenerate Fermi Gases. We begin with a discussion of the thermal deBroglie wavelength defined as

$$\Lambda = \frac{\sqrt{2\pi\hbar}}{\sqrt{mk_B T}} \quad (2.36)$$

where \hbar is the reduced Planck constant, k_B is the Boltzman constant, m is the mass of the atom in question [46]. Reducing the temperature at constant particle density raises the deBroglie wavelength. At some temperature, the deBroglie wavelength becomes comparable to the distance between atoms. It is at this temperature that the wavefunctions representing the atoms begin to share common space and no longer behave like classical particles that collide like billiard balls [47]. Similar to stimulated emission in optics, scattering of atoms into the ground state is further enhanced by bosonic stimulation and leads to a macroscopically occupied ground state (BEC) that leaves only a small fraction of thermal atoms. The “thermal tail” population continues to decay as the temperature is lowered to $T = 0$ (absolute zero). [47].

The temperature of a thermal cloud can be extracted by monitoring the cloud after it is released from a trapping potential and allowed to expand ballistically over some varied time-of-flight (TOF). With enough clean data, the Gaussian profile of the cloud can be fit in two orthogonal directions and the width σ_x and σ_y can be

tracked as the time-of-flight increases. The data will follow the form,

$$\sigma(t) = \sqrt{\sigma_0^2 + (k_B T/m)t^2} \quad (2.37)$$

where k_B is the Boltzmann constant, T is the temperature and m the mass of the atom in question. A qualitative depiction of the cloud expansion is shown in Figure 2.5.

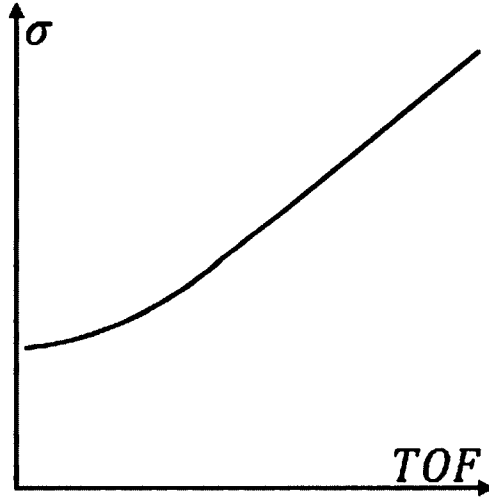


FIG. 2.5: A qualitative depiction of the thermal expansion of cold and ultracold atoms release from a conservative trapping potential. This is one of the most common measurement techniques used in the lab. The data can be fit using Equation 2.37. TOF stands for time-of-flight or t in Equation 2.37.

We can define the phase-space density as the dimensionless quantity

$$\rho = n_{peak} \Lambda^3 \quad (2.38)$$

where n_{peak} is the peak spatial density of atoms in the trapped cloud of interest. A rough approximation of this quantity is the number of particles in a box of size \hbar^3 in

phase-space. In a gas of indistinguishable bosons (all in the same spin state), the onset of Bose-Einstein condensation (i.e. macroscopic occupation of the mechanical ground state of the system) occurs at a phase-space density of 2.612 [46, 47]. A favorable method of achieving the required cooling and compression is through the use of a conservative potential such as a magnetic or optical dipole trap, and subsequently cool the system through evaporative methods. The maximum achievable phase-space density through evaporative cooling is usually proportional to its value before cooling, thus the starting conditions are just as important as the efficiency of the evaporation system.

The spatial density distribution, $n(x, y, z)$, can be computed from the total number of atoms N and the three dimensional size of the gaussian-shaped cloud as

$$n(x, y, z) = n_{peak} \exp \left[-\frac{1}{2} \left(\left(\frac{x}{\sigma_x} \right)^2 + \left(\frac{y}{\sigma_y} \right)^2 + \left(\frac{z}{\sigma_z} \right)^2 \right) \right] \quad (2.39)$$

where σ_x, σ_y , and σ_z define the size of the cloud. n_{peak} is then given by the normalization condition

$$\int_{all\ space} n(x, y, z) dx dy dz = N = n_{peak} \int_{-\infty}^{\infty} \exp \left[-\frac{1}{2} \left(\frac{x}{\sigma_x} \right)^2 \right] dx \cdot \int_{-\infty}^{\infty} \exp \left[-\frac{1}{2} \left(\frac{y}{\sigma_y} \right)^2 \right] dy \int_{-\infty}^{\infty} \exp \left[-\frac{1}{2} \left(\frac{z}{\sigma_z} \right)^2 \right] dz \quad (2.40)$$

where each integral term evaluates to $\sqrt{2\pi}\sigma_i$ and the expression becomes

$$N = n_{peak} (2\pi)^{3/2} \sigma_x \sigma_y \sigma_z. \quad (2.41)$$

Thus the peak spatial density in $atoms/m^3$ is

$$n_{peak} = \frac{N}{(2\pi)^{3/2} \sigma_x \sigma_y \sigma_z}. \quad (2.42)$$

This quantity can be calculated at any point over the course of the different cooling and trapping processes employed in our apparatus (MOT, magnetic trap, evaporative cooling, etc...) in order to track the phase-space density along the path to quantum degeneracy. This is used in Chapter 5 to confirm the production of ^{87}Rb Bose-Einstein condensate.

CHAPTER 3

Microwave and RF Potentials

This chapter describes the AC Zeeman shift and how it can be used to create microwave and RF magnetic field potentials to trap and manipulate ultracold atoms. The discussion begins with the theoretical background of the AC Zeeman shift in the dressed atom basis and progresses into simulations of atom chip roughness and the mechanisms by which μ/RF potentials can suppress it.

3.1 AC Zeeman Shift

An atom in the presence of an oscillating magnetic field B_{rf} experiences an energy shift of its magnetic hyperfine levels known as the AC Zeeman effect. It takes exactly the same form as the dipole force discussed in Chapter 2 with one key difference: the lack of spontaneous emission. Here I present a model of a two-level atom interacting with N μ/RF photons, using the dressed atom basis $\{|g, N\rangle, |e, N - 1\rangle\}$ where the ground and excited states, $|g\rangle$ and $|e\rangle$ [48]. The Hamiltonian for the atom- μ/RF photon system is given by

$$\mathcal{H}_{rf} = \mathcal{H}_a + \mathcal{H}_{rad} + \mathcal{H}_{int} \quad (3.1)$$

where \mathcal{H}_a represents the basic atomic Hamiltonian that gives rise to the atomic energy levels [20]. \mathcal{H}_{rad} represents the radiation field component defined as $\mathcal{H}_{rad} = \hbar\omega_l(a^\dagger a + 1/2)$ with eigenvalues of $E_N = (N + 1/2)\hbar\omega_l$ where a^\dagger and a are the creation and annihilation operators for the μ /RF photons, respectively. \mathcal{H}_{int} represents the atom-field interaction and is analogous to Equation 2.1. The full Hamiltonian can be represented as

$$\mathcal{H}_{rf} = \hbar\omega_{ge} \begin{bmatrix} 0 & 0 \\ 0 & 1 \end{bmatrix} + \hbar\omega_{rf} \begin{bmatrix} N & 0 \\ 0 & N - 1 \end{bmatrix} + \frac{\hbar}{2} \begin{bmatrix} 0 & \Omega_{rf} \\ \Omega_{rf}^* & 0 \end{bmatrix} \quad (3.2)$$

where $\Omega_{rf} = \langle g | -\vec{\mu} \cdot \vec{B}_{rf} | e \rangle / \hbar$ is the Rabi frequency given by the Zeeman interaction between the magnetic moment $\vec{\mu}$ of the atom and the RF magnetic field \vec{B}_{rf} . By reestablishing the energy origin appropriately, the Hamiltonian can be rewritten in the form

$$\mathcal{H}_{rf} = \hbar \begin{bmatrix} \delta & \frac{1}{2}\Omega_{rf} \\ \frac{1}{2}\Omega_{rf}^* & 0 \end{bmatrix} \quad (3.3)$$

where $\delta = \omega_{rf} - \omega_{ge}$ is the detuning of the μ /RF magnetic field (\vec{B}_{rf}) from the atomic transition, not unlike the detuning described in Chapter 2. Thus, a two level atom, separated by energy $\hbar\omega_{ge}$, placed in an off resonance μ /RF magnetic field of frequency ω_{rf} will see its shifted energy levels as,

$$E_{g,e} = \left(-\delta \pm \sqrt{|\Omega_{rf}|^2 + \delta^2} \right) \frac{\hbar}{2}. \quad (3.4)$$

In the limit where $\Omega_{rf} \ll |\delta|$, the interaction induced energy shifts are reduced to,

$$\Delta E_{(g,e)} = \pm \frac{|\Omega|^2}{4\delta} \hbar = \pm \frac{|\langle e | \vec{\mu} \cdot \vec{B}_{rf} | g \rangle|^2}{4\delta \hbar} \quad (3.5)$$

where $\vec{\mu}$ is the atomic magnetic moment and the local DC magnetic field defines the quantization axis for the atomic spin and angular momentum. Figure 3.1 shows the energy shifts of E_g and E_e for red (a) and blue detuning (b) of the μ /RF magnetic field \vec{B}_{rf} .

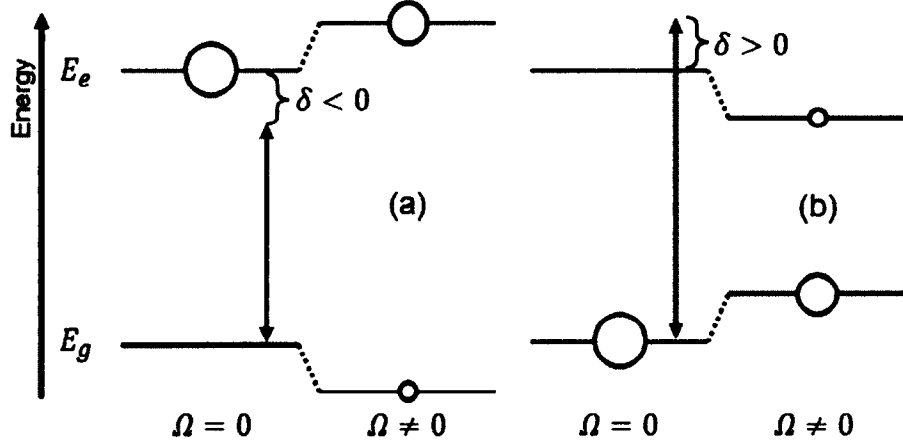


FIG. 3.1: Relevant level shifts for trapping 2-level atoms with a μ /RF magnetic near-field in the vicinity of a magnetic minimum. (a) Red-detuning of RF near-field is necessary for confining atoms in the $|e\rangle$ state, while (b) blue-detuning is necessary for confining atoms in the $|g\rangle$ state. The trapping process mixes the original states somewhat, whose relative fractions are represented qualitatively by the area of the circles.

3.2 Spin-Dependent Force

The AC Zeeman potential created by B_{rf} is a conservative potential that when given some spatial dependence creates a force on atoms in both the excited and ground states. This force is not unlike the dipole force that results from a strong, far off resonant optical field, taking the form of

$$\vec{F}_{g,e} = \nabla U_{g,e} = \nabla E'_{g,e} = \pm \frac{\nabla |\langle e | \vec{\mu} \cdot \vec{B} | g \rangle|^2}{4\delta\hbar} \quad (3.6)$$

where the key point is the dependence on the magnetic field gradient. The force is inherently spin-dependent because of the dependence on the atomic state ($|e\rangle$ or $|g\rangle$) and the detuning. Atoms in the excited state will seek low amplitude regions of red-detuned μ /RF field as shown in Figure 3.1 (a) and high amplitude regions of blue-detuned field as depicted in Figure 3.1 (b). Ground state atoms exhibit the opposite behavior.

In contrast to optical forces, spontaneous emission-induced spin-flipping is essentially non-existent, allowing atoms to remain in the excited state (and also the ground state). This technique requires a DC magnetic bias field to establish the quantization axis and maintain separation of the hyperfine levels, but it does not influence the AC Zeeman force. The hyperfine splittings of ^{39}K and ^{41}K (460 and 254 MHz, respectively [27]) are more accessible than the traditionally used ^{87}Rb (6.8 GHz [26]). One may be able to work as low as 35 MHz in ^{41}K at 51 G with an intra-manifold transition or 1360 MHz in ^{39}K at 350 G [49, 27]. The significance of these DC magnetic bias field examples is that they are attainable with existing Helmholtz coil pairs in the lab.

3.2.1 Feshbach Resonance

In ultracold gases, the close proximity of atoms generates non-trivial inter-atom interactions. The magnitude and sign of these interactions can be controlled by the local magnetic field in the vicinity of an atom-atom scattering resonance called a Feshbach resonance. A magnetic field that causes interactions to pass through zero is known as a Feshbach zero-crossing. Feshbach resonance is especially compatible with μ /RF potentials as the external DC bias field that establishes the quantization axis provides an additional, independent parameter to manipulate the interactions between ultracold bosonic atoms, crucial to such experiments as interferometry and

many-body physics [38, 50, 51, 52]. Potassium isotopes have relatively accessible Feshbach resonances at 25.9 G, 33.6 G (^{39}K) and 51.4 G (^{41}K) [27].

3.2.2 Spin-Selectivity

A state-selective potential is created when a μ/RF field is tuned to a particular hyperfine splitting while remaining sufficiently detuned from other nearby transitions. Figure 3.2 illustrates this example for the similar hyperfine structure of the $5S_{1/2}$ levels of ^{87}Rb and the $4S_{1/2}$ in ^{39}K and ^{41}K . This technique has the ability to manipulate or trap any spin state, regardless of the applied DC magnetic bias field while avoiding spontaneous spin-flips and leaving neighboring hyperfine transitions unshifted. Multiple states could be simultaneously manipulated by applying additional magnetic fields appropriately detuned from other transitions. These techniques are broadly applicable to atomic and molecular systems with hyperfine structure.

3.3 Atom Chip Near-Field Potentials

In practice, the wavelength λ of hyperfine transitions is usually too large (0.01 – 1 m) to achieve sufficient focusing of a propagating electromagnetic wave to create a gradient strong enough for trapping atoms. Although cavities have been used to generate large gradients for demonstrating this effect [15], and recent use of metamaterials has achieved sub-wavelength focusing of microwaves for tweezer applications [53], strong near-field potentials are available on atom chips at reasonable currents. Atom chips provide a more practical method of producing large enough gradients to exploit the AC Zeeman force. Recently, μ/RF atom chip potentials have been incorporated into ion trap atom chips [54, 55] as well as experiments in ion trap quantum computing with impressive success [56, 57, 58, 59].

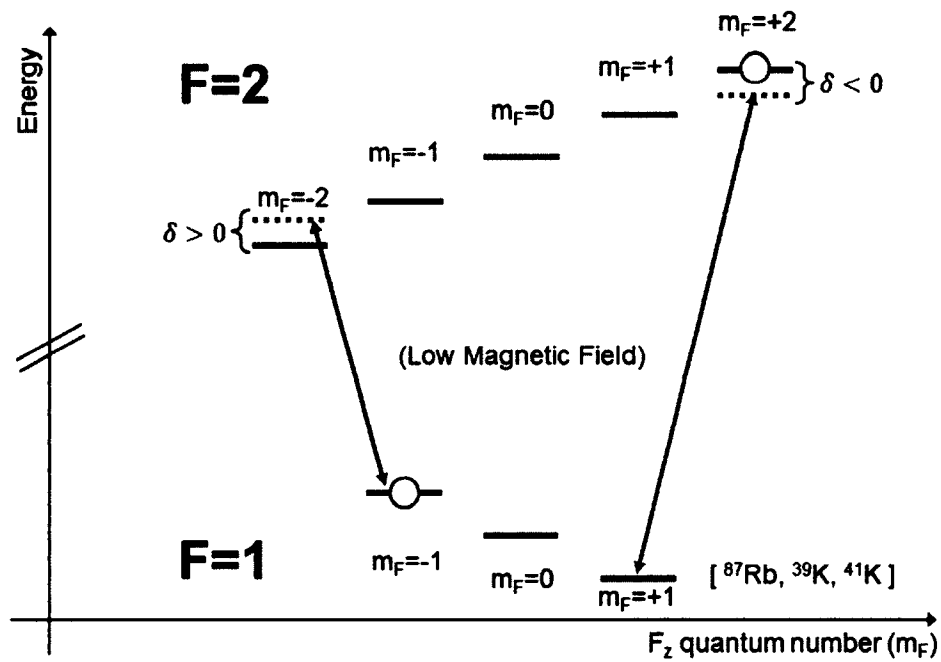


FIG. 3.2: An example of using a red-detuned AC magnetic field to manipulate the $m_F = +2$ excited state while simultaneously using a blue-detuned field to target the $m_F = 0$ ground state. The eight sublevels shown represent the similar hyperfine structure of the $5S_{1/2}$ levels in ^{87}Rb and the $4S_{1/2}$ in ^{39}K and ^{41}K

In the near-field where the atom chip wire width w satisfies the condition $w \ll r \ll \lambda$ where r is the position of the atoms, the amplitude and direction of an atom chip RF magnetic field is identical to the magnetostatic solution of a DC current through the same atom chip wires. In other words,

$$\begin{aligned}
I_{DC} &\rightarrow B_{DC}(I_{DC}) \\
I_{rf} &\rightarrow B_{rf} = B_{DC}(I_{rf}) \\
I_{rf} &= I_0 \cos(w_{rf}t).
\end{aligned} \tag{3.7}$$

Due to magnetic equivalent of Earnshaw's theorem [60], only local \vec{B}_{rf} minima can be generated in the near-field, thus the ground state $|g\rangle$ can only be trapped by a blue-detuned μ /RF magnetic field, whereas the excited state $|e\rangle$ requires a red-detuning. Equation 3.5 can be evaluated in the stretched state transition of ^{87}Rb ($5S_{1/2}|F=1, m_f=1\rangle$ to $5S_{1/2}|F=2, m_f=2\rangle$), shown as the red transition in Figure 3.2) and similar hyperfine structures (ie ^{39}K and ^{41}K). If the nuclear spin is neglected, the magnetic moment operator can be written as $\vec{\mu} = (g_s \mu_B / \hbar) \mathbf{S}$, where \mathbf{S} is the spin operator for the valence electron. In the circular polarization basis, the Rabi frequency is described by,

$$\Omega = \langle e | \vec{\mu} \cdot \vec{B}_{rf} | g \rangle / \hbar = \frac{\mu_B g_s}{2\hbar^2} \langle e | \mathbf{S}_+ B_{rf,-} + \mathbf{S}_- B_{rf,+} + 2\mathbf{S}_z B_{rf,z} | g \rangle \tag{3.8}$$

where $\mathbf{S}_{\pm} = \mathbf{S}_x \pm i\mathbf{S}_y$ and $B_{rf,\pm} = B_{rf,x} \pm iB_{rf,y}$. $|e\rangle$ represents the hyperfine state $|F=2, m_f=2\rangle$ and the ground state $|g\rangle$ is $F=1, m_f=1$. In our geometry, $B_{rf,z} = 0$ and thus the Rabi frequency simplifies to,

$$\Omega = \frac{\mu_B g_s}{2\hbar^2} \langle 1, 1 | \mathbf{S}_+ B_{rf,-} + \mathbf{S}_- B_{rf,+} | 2, 2 \rangle \tag{3.9}$$

in the F, m_f basis. In the basis where I and S are good quantum numbers,

$$\begin{aligned} |2, 2\rangle &= |3/2, 1/2\rangle \\ |1, 1\rangle &= \frac{\sqrt{3}}{2}|3/2, -1/2\rangle - \frac{1}{2}|1/2, 1/2\rangle \end{aligned} \quad (3.10)$$

where the $\sqrt{3}/2$ and $1/2$ are Clebsch-Gordan coefficients. In this basis, the S_{\pm} operators can act as

$$\mathbf{S}_{\pm}|S, m_s\rangle = \sqrt{S(S+1) + m_s(m_s \pm 1)}\hbar|S, m_s \pm 1\rangle \quad (3.11)$$

where $S = 1/2$ for ^{87}Rb and ^{39}K . The only non-zero term is,

$$\begin{aligned} \Omega &= \frac{\sqrt{3}}{2} \frac{\mu_B g_s}{\hbar} \langle 3/2, 1/2 | B_{rf,-} | 3/2, 1/2 \rangle \\ &= \frac{\sqrt{3}\mu_B g_s}{2\hbar} B_{rf,-} = \frac{\sqrt{3}\mu_B g_s}{4\hbar} (B_{rf,x} - iB_{rf,y}) \end{aligned} \quad (3.12)$$

Following right along, $E_{\pm} = \hbar|\Omega|^2/4\delta$ from which the μ/RF potential takes the form

$$U_{rf} = \frac{3\mu_B^2 g_s^2}{64\delta\hbar} B_{rf}^2 = \frac{3\mu_B^2 g_s^2}{64\delta\hbar} (B_x^2 + B_y^2) \quad (3.13)$$

where g_s is 2, the g-factor for electron spin. The DC Zeeman potential follows the form

$$U_{DC} = \mu_B m_F g_F |B| = \mu_B m_F g_F (B_x^2 + B_y^2 + B_z^2)^{1/2} \quad (3.14)$$

where and the Landé g-factor g_F is $1/2$ for the ^{87}Rb $F = 2$ levels as defined by Equation 2.32 and $m_F = +2$ for the $5S_{1/2}|F = 2, m_f = 2\rangle$ state of ^{87}Rb and similar hyperfine structures such as ^{39}K and ^{41}K . The point of this exercise is to illustrate the difference between the AC and DC Zeeman shifts. Most noticeably,

the AC Zeeman potential is inversely proportionally to the detuning of B_{rf} from the hyperfine splitting where as the DC Zeeman shift is proportional to m_F . More importantly for our purposes, the DC Zeeman potential is proportional to $|B|$ where the AC Zeeman potential follows B_{rf}^2 with no B_z component. This seemingly minor difference plays an important role when it comes to potential roughness, a topic explored in section 3.5.

3.4 DC Magnetic Chip Traps

Traditional atom chips use DC current through a Z-shaped planar wire combined with a uniform magnetic external field, B_{Hold} , to form a cigar shaped trap above the central wire segment. The diagram of Figure 3.3 illustrates the geometry of our atom chip as installed under vacuum. A third uniform magnetic field, known as B_{Ioffe} is directed along the longitudinal axis of the trap [61]. In the μ /RF case, B_{Ioffe} is a DC magnetic field that provides the quantization axis that defines the hyperfine splittings and can be adjusted to tune to magnetic Feshbach resonances and zeroes [61]. The atom chip used in this work was designed as a traditional DC magnetic trap device produced by photo-lithography on an aluminum nitride substrate. The mask used to produce the chip is shown in Figure 3.4 where the main z-wire is shown in blue. The prominent u-wires shown in red are typically used to coupling microwave and RF signals to the atom chip for evaporation but can also generate a micro-quadrupole trap, similar to that of an anti-helmholtz pair. The u-wire quadrupole trap is anecdotally easier to load and is sometimes used when first transferring atoms from the magnetic transport system to the atom chip. The magnetic transport system will be explained in detail in Chapter 7.

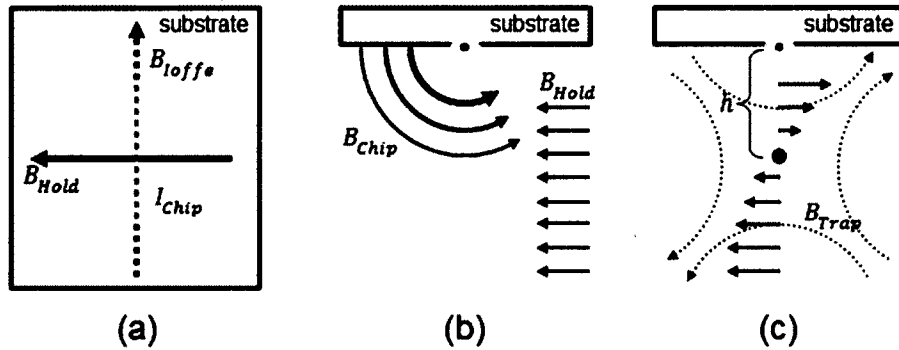


FIG. 3.3: Diagram of a traditional atom chip geometry designed for DC magnetic potential trapping. (a) Top view of the chip. The chip features a Z-shaped planar wire (gold) on the surface (gold) and two external, uniform DC fields B_{Ioffe} and B_{Hold} . The chip wire creates a circular field above its central axis that cancels with B_{Hold} (shown in b) at a distance h above the z-wire to form a region of zero field, shown as the red circle in (c). B_{Ioffe} is directed out of the page in (b) and (c) and provides a nonzero minimum field when combined with the field from the encap segments of the Z-wire, which also determine the longitudinal field curvature.

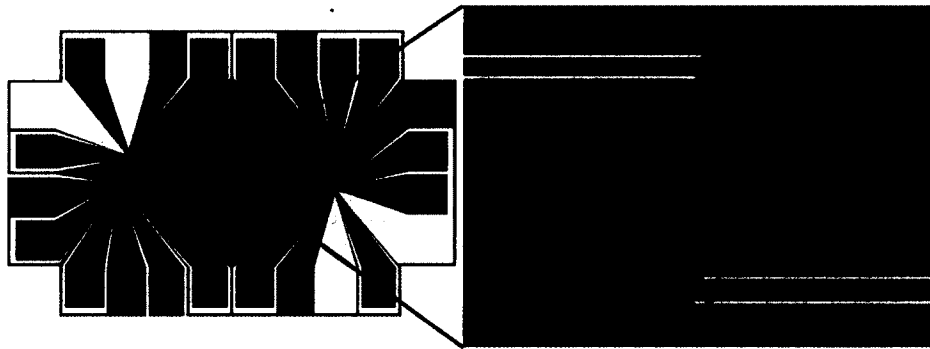


FIG. 3.4: Diagram of the fabrication mask used to produce the atom chip used for this work. The atom chip was designed and produced by Dylan Jarvis, Marcus Extavour and Thorsten Schumm of Joseph Thywissen's ultracold atom group at the University of Toronto. The chip itself (and a replacement) were graciously gifted to our group.

3.4.1 Atom Chip Modeling

The magnetic field from an atom chip can be calculated in the thin wire limit from the piece-wise line segments that form the Z-wire. The analytic expression for the magnetic field created by a finite wire segment can be obtained from the Biot-Savart law and takes the form,

$$\vec{B} = \frac{\mu_0 I}{4\pi} \cdot \frac{1}{(x-a)^2 + (y-b)^2} \cdot \left((y-b)\hat{x} - (x-a)\hat{y} \right) \cdot \left(\frac{z-c}{\sqrt{(z-c)^2 + (x-a)^2 + (y-b)^2}} + \frac{L-(z-c)}{\sqrt{(L-(z-c))^2 + (x-a)^2 + (y-b)^2}} \right) \quad (3.15)$$

where the point of interest is located at the coordinates (x, y, z) . The wire segment has dimensions of length L , with endpoints at the coordinates (a, b, c) and $(a, b, c+L)$ and current I directed along the $+\hat{z}$ axis. Equations 3.13 and 3.14 are used to construct the potentials from the static magnetic field components given by Equation 3.15.

Modeling the z-wire geometry of Figure 3.3 with an I_{Chip} of 1 A, a DC potential trap is created at approximately $100 \mu\text{m}$ above the surface of the chip. The presence of B_{Ioffe} guarantees a harmonic potential along all 3 axes. As for a μ/RF -based atom chip, in theory we can simulate any geometry desired; however, an important consideration is how efficiently the μ/RF signal can be coupled to the wires on the chip. For this reason, we have explored also transmission line geometries that present an impedance-matched load to the microwave signal. One such example is shown in Figure 3.5. In a geometry such as this, with dimensions a and h , a trap is formed at a location of a^2/h above the chip surface, aligned with the central axis of the transmission line. This analytic solution for the trap height was derived by fellow graduate student J. Field during his tenure. For simplicity, end caps have

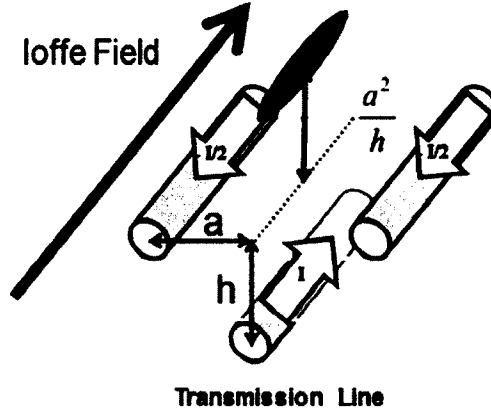


FIG. 3.5: Proposed geometry of a transmission line atom chip for microwave magnetic traps. This design does not provide endcaps, however the simple geometry (a, h) of the system creates a magnetic minimum at the location $\frac{a^2}{h}$ above the central wire of the chip when the microwave currents are balanced as depicted. This analytic result was first achieved by Jim Field.

been omitted. A profile of the magnitude of B_{rf}^2 plotted at the trap height above the atom chip is shown in Figure 3.6.

Driven by an oscillating current, I_{rf} with an amplitude of 1 A, as defined in Equation 3.7, an atom chip can create an μ /RF harmonic trap that is essentially equivalent to the DC harmonic trap by carefully manipulating the transmission wire geometry (a and h) to match the transverse trapping frequencies and trap height above the chip. As is quite obvious in Figure 3.7, the trap depths can be quite different. The trap height is typically on the order of 100 μm . Figure 3.7 compares the traditional DC Z-wire trap potential to that of the μ /RF transmission line potential based on Equation 3.13 in the vertical direction moving away from the face of the chip.

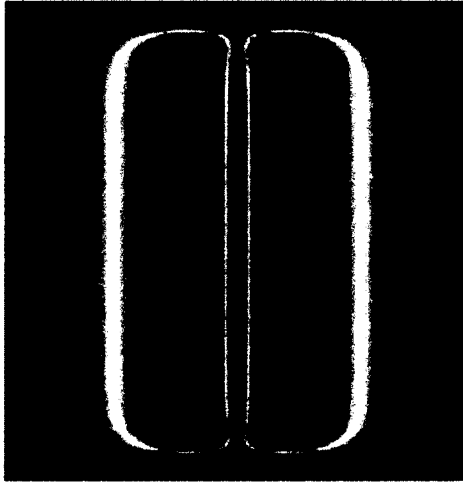


FIG. 3.6: Profile of B_{rf}^2 above a transmission line trap of the geometry described in Figure 3.5. The plot is taken as a horizontal slice at the height of $\frac{a^2}{h}$ where the magnetic minimum is located. Red corresponds to $B^2 = 0$ and blue/pink represents a maximum value of B_{rf}^2 . As shown in this calculated field potential, the design makes no attempt to provide an endcap for the trap.

3.5 Roughness Suppression

Surface defects and irregularities in the micro-fabricated wires of an atom chip will cause unwanted roughness in the magnetic potential. This is an inherent limitation to the technology that cannot as of yet be eliminated [62]. Local inhomogeneities in the magnetic field will affect the quality and effectiveness of the trap structure, and this places experimental limitations on traditional atom chips using DC magnetic fields. Nevertheless, atom chips are one of the most effective experimental systems for manipulating ultracold atoms. Tight confinement, strong gradients, and compact, scalable, cost effective systems are all advantages of using atom chips. However, the ultracold atomic samples are extremely sensitive to the potential shape, often occupying the deepest part of a trap where the roughness is most severe, causing segmentation of the atomic cloud. This has been thoroughly explored experimentally and the current solution is to operate the trap far enough

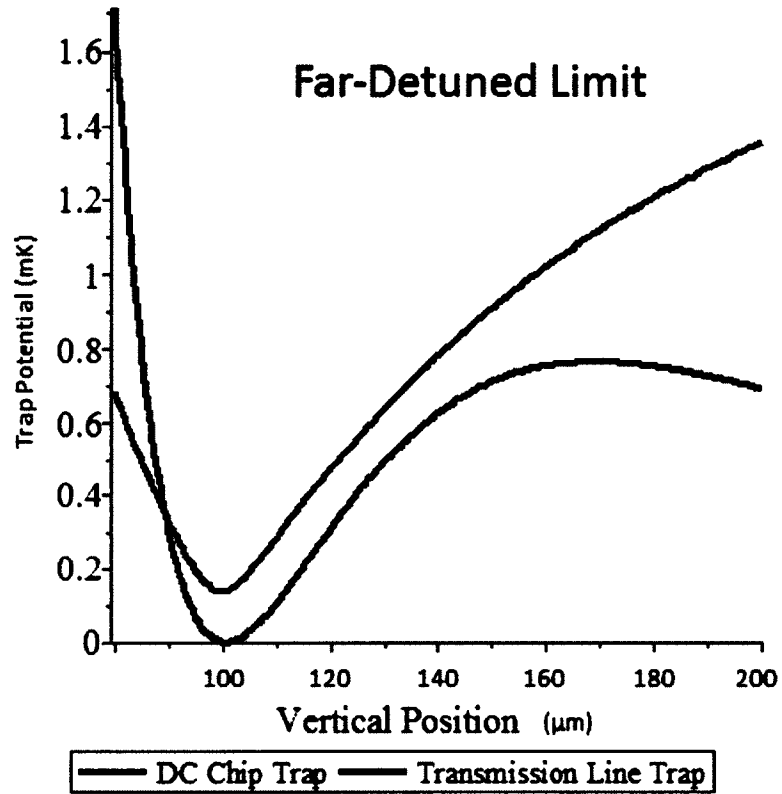


FIG. 3.7: Simulation of the vertical trapping potential of comparable AC and DC atom chip microtraps. The DC Z-wire trap (red) was simulated using 1 A of chip current. The AC transmission line trap (blue) was modeled using 1.4 A of RF current on the chip, at a detuning $\delta = 2\pi \times 1$ MHz from the ^{87}Rb stretched state hyperfine transition $5S_{1/2}|F = 1, m_f = 1\rangle \leftrightarrow 5S_{1/2}|F = 2, m_f = 2\rangle$. The transverse trapping frequencies were matched at 2.5 kHz. At this current, the wire separation parameters of a and h were determined to be $71 \mu\text{m}$ and $50 \mu\text{m}$, respectively.

away from current carrying wires as to sufficiently suppress the roughness [62]. This workaround comes with a large trade off, as it is inherently difficult to study atom-surface physics, where the desired trap to surface distance is very small.

As described by Equation 3.14, a DC magnetic potential depends on all three components of the magnetic field, which explains its sensitivity to any local deviations in the magnetic field caused by defects in the current carrying wires and underlying substrate surface. An important advantage of μ /RF magnetic potentials is that the lack of dependence on one field component (B_z , in the stretched state in our coordinate system) strongly suppresses the primary component of atom chip potential roughness. This can be represented in the following expressions, reduced from Equations 3.13 and 3.14,

$$\begin{aligned} U_{rf} &\propto \langle g|\vec{\mu} \cdot \vec{B}_{rf}|e\rangle \propto |\vec{B}_{rf}|^2 = B_x^2 + B_y^2 \\ U_{DC} &\propto |\vec{B}_{DC}| = (B_x^2 + B_y^2 + B_z^2)^{1/2} \simeq |B_z| + \frac{B_x^2 + B_y^2}{2|B_z|} + \dots \end{aligned} \quad (3.16)$$

where U_{DC} reduces to just $|B_z|$ at the very bottom of the trap where $|B_x|, |B_y| \ll |B_z|$. As shown in Figure 3.8, current which deviates from a straight line path by an angle α introduces a small magnetic field component along the main current axis, which is the direction of the axial magnetic field, B_{Ioffe} . The magnetic field at point P located at a distance h above a wire carrying current I that has been rotated by angle α can be expressed as,

$$B_{wire}(P) = \frac{\mu_0 I}{2\pi h} (\cos(\alpha)\hat{y} + \sin(\alpha)\hat{z}) \quad (3.17)$$

where the cartesian system is defined in Figure 3.8. Notice that B_{wire} reduces to B_y at $\alpha = 0$. At an angle of $\alpha = 0$, the magnetic field contains only a orthogonal component in the \hat{y} direction. As roughness is introduced into the system and α

becomes non-zero, a component parallel to the wire axis appears. This co-linear contribution (along \hat{z}) adds to the total magnetic potential B_z as αB_{wire} in the small angle approximation of $\sin(\alpha) \approx \alpha$, where B_{wire} is the magnetic field at point P generated by the current carrying wire, and α is the characteristic small angle relative to the \hat{z} axis. This component can be seen as the term $(x - a)\sin(\alpha)\hat{z}$ in the more general Equation 3.18.

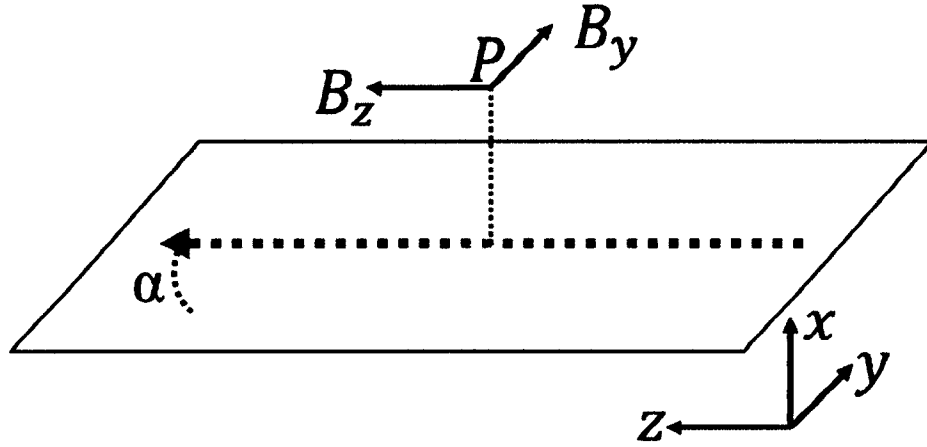


FIG. 3.8: Vector representation of the effect of roughness. The current flow (gold) deviates from the intended direction shown in grey by an angle α . The potential roughness introduced to the system can be described in terms of $B_z(\alpha)$ and $B_y(\alpha)$.

To effectively simulate roughness, simple bumps are introduced to a wire segment by the addition of an angular parameter in the $y - z$ plane. Equation 3.15 is expanded to take the form,

$$\vec{B} = \frac{\mu_o I}{4\pi} \cdot \frac{1}{(x - a)^2 + (y - b)^2} \cdot \left(-(y - b)\hat{x} + (x - a) \cdot \cos(\alpha)\hat{y} + (x - a) \cdot \sin(\alpha)\hat{z} \right) \cdot \left(\frac{z - c}{\sqrt{(z - c)^2 + (x - a)^2 + (y - b)^2}} + \frac{L - (z - c)}{\sqrt{(L - (z - c))^2 + (x - a)^2 + (y - b)^2}} \right) \quad (3.18)$$

where it can easily be seen that the angle introduces an additional component in

the \hat{z} direction of \vec{B} .

In the atom chip geometries considered here, the μ /RF magnetic field that contributes to the potential is always normal to the quantization axis. Any parallel μ /RF magnetic field component introduced by wire defects does not contribute to the potential, as there is no nearby associated transition to drive. This statement is made with confidence as the described μ /RF potential is created by driving off resonant σ^\pm transitions, and not π transitions. A current deviation contributes to the AC Zeeman potential of a π transition as $\alpha^2 B_{wire}^2 / \delta_\pi$, where δ_π is the detuning to the nearest allowed transition for π -polarization. In addition, the angle α reduces the magnitude of the perpendicular component (B_y) of the μ /RF magnetic field by $\alpha^2 B_{wire}$ such that all contributions to the potential roughness scale as α^2 , which is very small for $\alpha \ll 1$. This can be seen by taking the small angle approximation of the \hat{y} component of Equation 3.17 or $(1 - \alpha^2/2)\hat{y}$.

3.5.1 Simulation

For the case of the stretched state in a detuned near-field, the μ /RF potential is independent of the magnetic field component along the direction of the current carrying wire central segment (\hat{z}) due to the choice of detuning δ and the fact that $B_{Ioffe} \parallel \hat{z}$. Any field component induced in the z-axis by a wire defect is suppressed in the μ /RF potential compared to an equivalent magnetic DC potential. Using a simple model of a single wire defect shown in Figure 3.9, I have computed the resulting potential roughness in both cases, as shown in Figure 3.10. Unfortunately, it is not as simple as calculating the field components of an isolated bump segment alone because of the nonlinear B_{rf}^2 term in the μ /RF magnetic potential. The net potential roughness is computed from the difference between an ideal, roughness-free

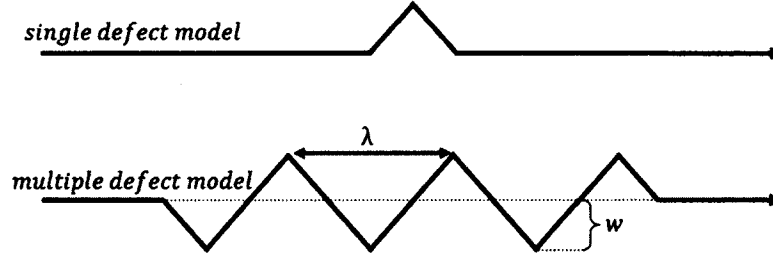


FIG. 3.9: A model of a finite current carrying wire as simulated in this work. The top example displays the simplest case of a single simulated wire deviation. The bottom model represents multiple defects such that an effective wavelength can be defined. The parameter w is held fixed at $2.5\mu\text{m}$ throughout the simulation for simplicity.

potential and that of the engineered wire bump as described with

$$U_{ideal} - U_{defect} = U_{roughness} \quad (3.19)$$

which applies to both the DC and μ/Rf cases. For similar trap parameters, the μ/Rf potential roughness is one or more orders of magnitude lower than that of the DC magnetic trap depending on the bump characteristics. The symmetry of the disturbance also changes from odd (DC case) to even (μ/Rf). Odd deviations involve both positive and negative excursions around a zero-crossing that creates a unique feature in the bottom of a trap. This feature presents itself as a small potential wall coupled next to a divot or dimple. Depending on its location and the temperature of the atomic cloud, this feature could create an unwanted segmentation or bunching of the atom cloud, especially if it exists near the very bottom. The even behavior of the μ/Rf potential roughness has no such zero-crossing, only presenting a potential wall of much smaller magnitude. A visual explanation of the roughness shape is presented in Figure 3.11.

A second mechanism has been identified when multiple defects are considered.

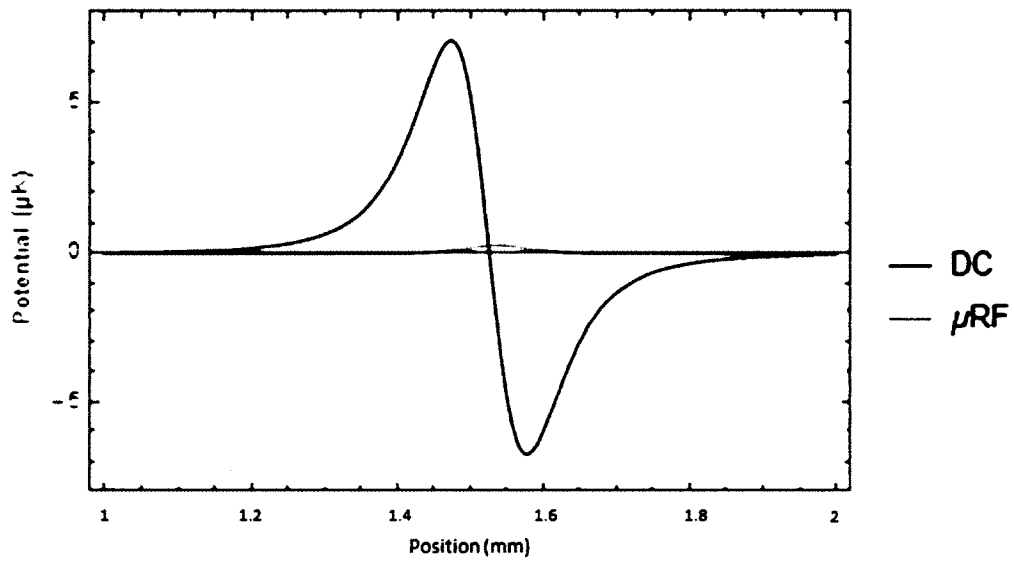


FIG. 3.10: Comparison of μ /RF & DC potential roughness for a single, isolated defect. The magnitude of potential roughness is reduced when moving from DC to μ /RF magnetic fields, and the character changes from odd behavior (blue, DC case) to even (orange, μ /RF case). $I_{DC} = 1$ A, $B_{I_{offe}} = 1$ G, $I_{\mu/RF} = 1.4$ A. The trap center was located at $100 \mu\text{m}$ above the wire segment.

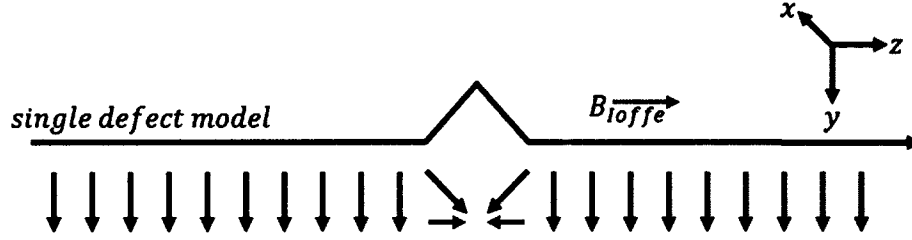


FIG. 3.11: Using the single bump model of Figure 3.9, the dispersive shape of the DC roughness can be visually explained. As a wire segment changes direction, a component is introduced along B_{offe} in the \hat{z} direction. As the μ/RF potential does not depend on B_z component in our geometry, this component has no effect on the roughness. In the case of the DC potential however, all components contribute to the potential as it follows the magnitude of \vec{B} . At the very bottom of the trap in fact U_{DC} is essentially linear with respect to B_{offe} as the other components contribute minimally. The roughness contributes along B_{offe} on one side of the bump and opposes it on the other side, introducing a positive deviation followed by a negative one, hence the dispersive shape seen in Figure 3.10.

Depicted in Figure 3.12, as the roughness from individual features builds, the combined effect is dominated by symmetry. In the DC trap, each bump produces a zero-crossing and a corrugated structure emerges which can lead to unwanted partitioning of the ultracold atomic cloud. μ/RF roughness remains orders of magnitude smaller as well as retaining the even structure where the features are always positive. In the μ/RF case, the multiple bumps can meld into one and thus lose their individual character. The simulated periodic wire defect can define an effective wavelength λ , which should be thought of as a spatial frequency that the current follows down the wire. In theory, higher frequency wire features should result in less μ/RF potential roughness as the individual features overlap more tightly where the net effect is a higher trap floor and modified trap frequency.

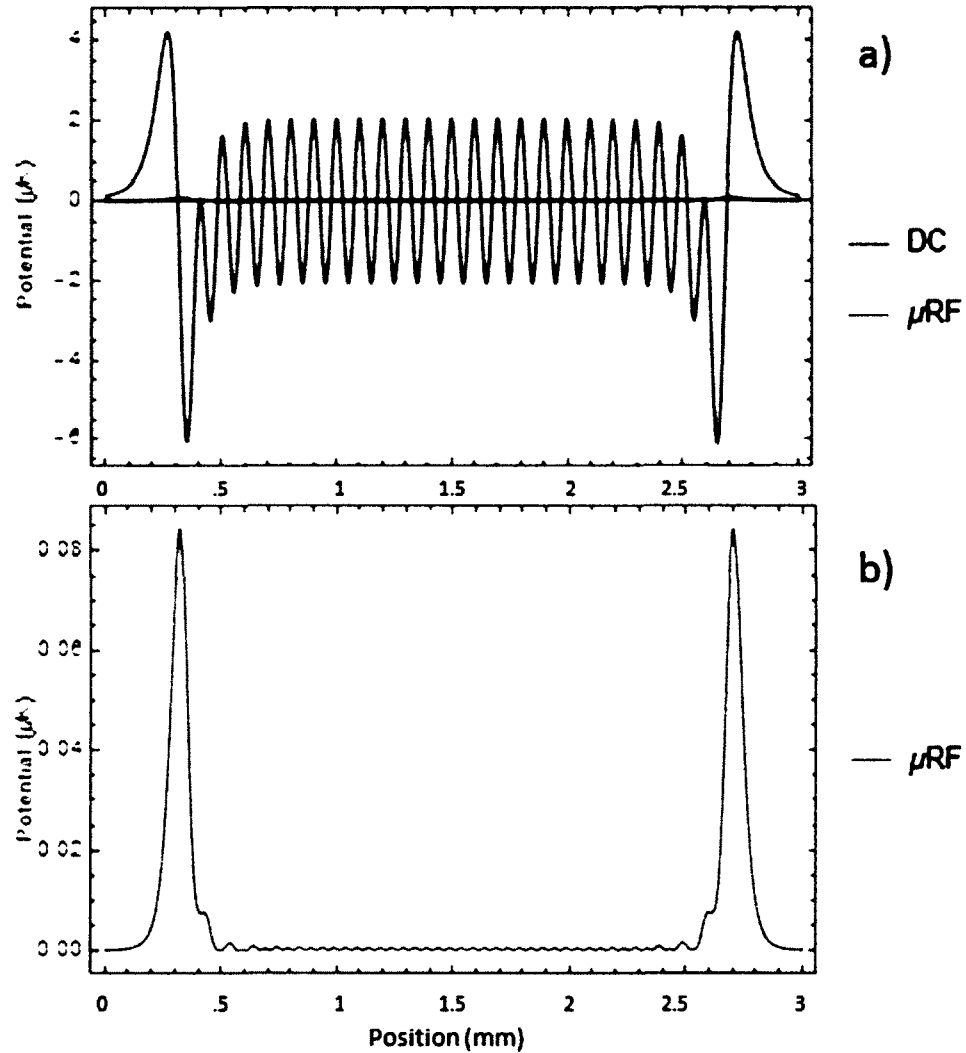


FIG. 3.12: (a) Comparison of μRF & DC potential roughness for a periodic defect. In this case, the contribution from multiple defects causes a corrugation of the potential in the DC case (blue), which can segment an ultracold cloud of atoms. The μRF case (orange) is orders of magnitude smaller and does not display the problematic corrugation. (b) The μRF result from (a) is replotted to show the detail. Notice the scale of the vertical axis. $I_{DC} = 1$ A, $B_{\text{Offe}} = 1$ G, $I_{\mu\text{RF}} = 1.4$ A. The trap height was located at $100 \mu\text{m}$ above the wire segment.

3.5.2 Suppression Factor

To quantify the reduction in potential roughness expected when comparing a μ/RF potential as to an equivalent DC potential, a suppression factor, η , is defined as the ratio of peak DC to μ/RF roughness. The location of the peak DC roughness is not stationary, and changes as the bump parameters vary, so a derivative algorithm is used to automate its calculation during the simulation. Evaluating the differential equation,

$$\frac{dU_{DC}}{d\vec{r}} = 0 \quad (3.20)$$

leads to the point \vec{r}_{peak} at which the DC roughness is at a local maximum. In the μ/RF potential, the peak roughness coincides with the center of the bump geometry, as it displays even behavior. This point is defined as \vec{r}_{center} in the expression for the suppression factor,

$$\eta = \frac{U_{DC}(\vec{r}_{peak})}{U_{\mu/\text{RF}}(\vec{r}_{center})}. \quad (3.21)$$

Trends emerge as this suppression factor is computed as a function of trap height and the effective wavelength λ of the periodic wire defects. Shorter effective wavelength and larger trap heights result in a greater suppression factor as seen in Figure 3.13. The deviation width was fixed to $\pm 2.5\mu\text{m}$ from the z-axis as the effective wavelength is varied from $30\mu\text{m}$ to $100\mu\text{m}$. As Figure 3.13 (a) shows, the suppression factor increases significantly with the trap height. Higher frequency deviations also result in a higher suppression factor; nevertheless, it seems to approach a saturation limit that depends on the trap height. The theoretical results presented here should be considered in future designs of μ/RF atom chips.

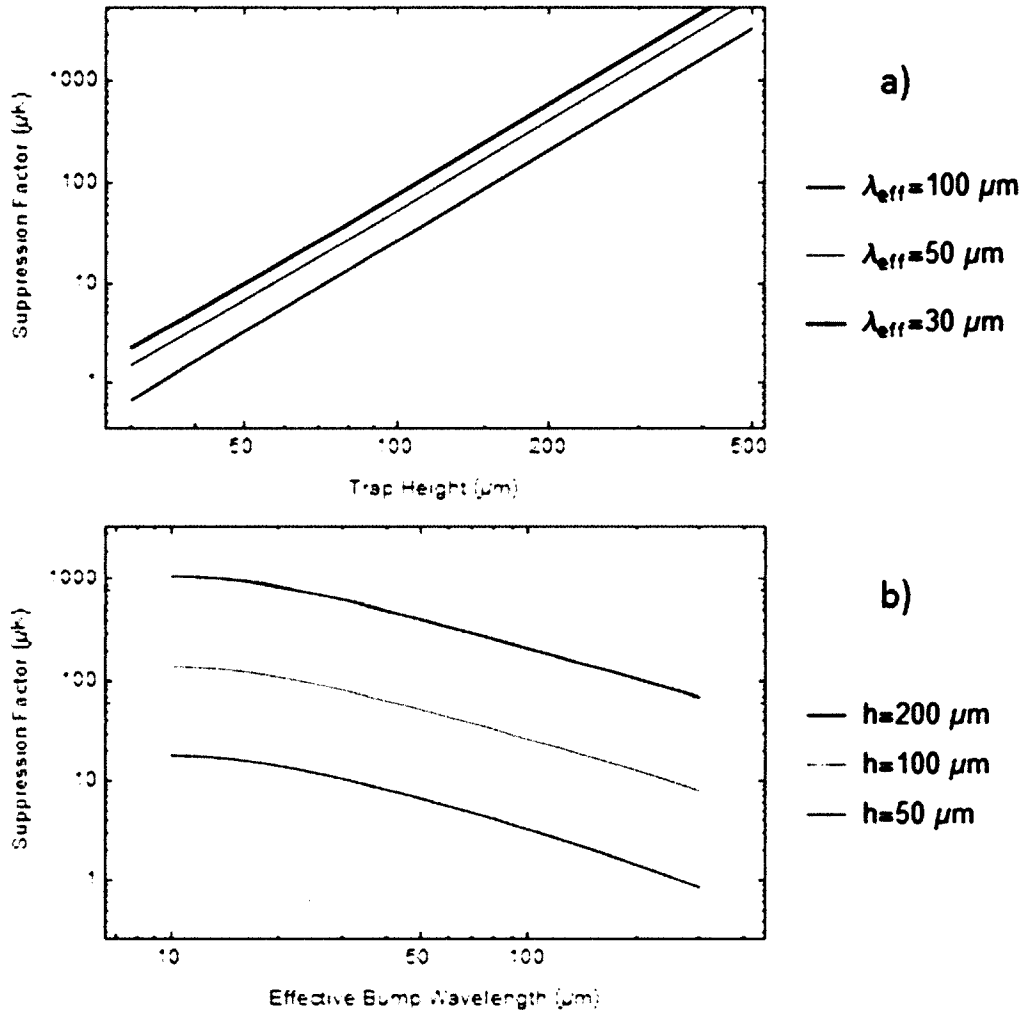


FIG. 3.13: (a) A plot of the newly defined suppression factor as a function of trap height above the atom chip. Three effective wavelengths of 30, 50 and 100 μm were considered and are represented here. (b) A plot of the newly defined suppression factors as a function of the effective wavelength of periodic roughness. Three trap heights of 50, 100 and 200 μm were considered and are represented here. Both plots were generated from a single set of trap parameters matching those used for Figure 3.10 (a).

CHAPTER 4

Apparatus

In this chapter, I describe the design, construction, and features of the apparatus as completed during my tenure. The primary use of the system is to prepare ultracold rubidium and potassium for on-chip experiments involving μ /RF potentials, however its actual capabilities amount to much more. The system is depicted in Figure 4.1, which shows its major magnetic, optical and vacuum components. So far, the apparatus has produced ultracold Rb and K, ^{87}Rb BEC, and atom chip-trapped ^{39}K , a world first. Major features include two glass chambers, a fast magnetic switch for the MOT coils, magnetic transport system, two dipole traps, and an atom chip. Of these systems, I contributed most directly to the magnetic switch electronics and MOT coils, construction and sequencing of the magnetic transport system, potassium laser system, and design of the microwave evaporation system. Each of these systems will be explained in greater detail in Chapters 6, 7, 8, and 9.

Success of this experimental apparatus would not have been possible without the tireless efforts of my colleagues and advisor. The transport coils were designed and constructed by Ayana Garcia, the atom chip support structure was designed, constructed and installed by James Field, a multiplexer was constructed by Seth

Aubin for switching of the transport system, and the apparatus laser systems were configured and aligned by Megan Ivory.

4.1 Vacuum System

The dual chamber design of the vacuum system was chosen to keep the atom chip and science cell clean, contaminant-free, and somewhat isolated from the dynamically varied vapor pressure of the MOT cell. As shown in Figure 4.1, the MOT and atom chip are located in two double-ended glass cells (Technical Glass) connected by a tube with a right-angle corner. The corner eliminates line-of-sight trajectories between the cells and allows the science cell to be oriented vertically for long time-of-flight (TOF) imaging of atoms released from the atom chip.

4.1.1 MOT Cell

The glass used for the MOT cell is constructed of Pyrex with a rectangular middle section of dimensions 17 cm in length and 6.3 cm in both width and height. Both ends are connected to cylindrical glass necks that transition to glass-to-metal seals of diameters 2.75 in. and 4.5 in. The 2.75 in. end features a formed bellows, allowing the overall 51 cm length to be adjusted by a few millimeters and providing relief against mechanical stress and strain during bake-outs. The MOT cell is supported by a 4.5 in. Conflat six-way vacuum cube that connects to a 55 l/s ion pump, a titanium-sublimation pump (TSP), an all-metal angle valve, a residual-gas analyzer (RGA), and a vacuum viewport along the long axis. The ion pump (Varian StarIon Plus 55) operates at 7kV as the primary MOT cell pump. The TSP assembly (Gamma Vacuum) is attached via a 4.5 in. Conflat right-angle elbow and provides a calculated pumping rate of about 60 l/s, but is generally activated about once a year and reserved as a backup. The all-metal angle valve provides a con-

nection to a 60 l/s turbo-molecular pump (Pfeiffer) used for initial pump down and bake-out. The RGA (ExTorr XT100) is installed on a four-way cross with a vacuum viewport for independent verification of filament operation. The RGA ion gauge indicates that the vacuum is in the low 10^{-10} Torr range, due almost exclusively to hydrogen.

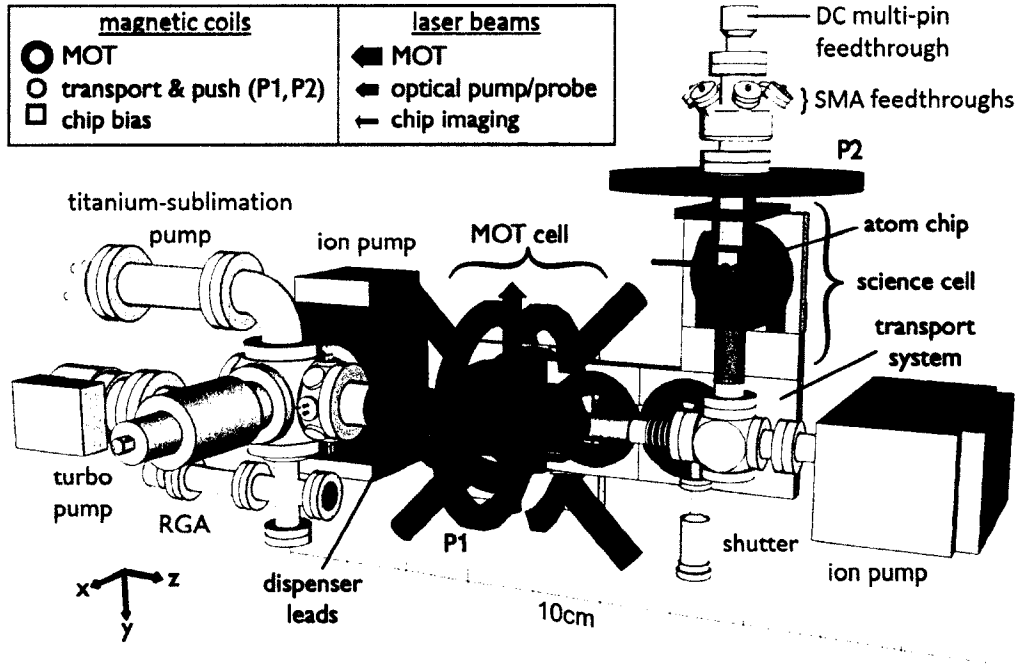


FIG. 4.1: Ultracold atom vacuum apparatus. The figure depicts the vacuum system components (grey labels), laser beams, dual-species MOT and transport magnetic coils, and the atom chip. Large red arrows: dual-species MOT trapping beams. Green arrows: Optical pumping and MOT absorption imaging beams. Small red arrows: Atom chip absorption imaging beams. Purple coils: MOT anti-Helmholtz coils (a portion of the foreground coil has been removed to show the MOT region) and the MOT bias coils. Orange coils: Transport system coils; P1: MOT cell push coil pair; and MOT bias coils; P2: atom chip push coil. The foreground half of the transport system and part of coil P1 have been omitted to show the vacuum system. Blue coils: Atom chip biasing coils. The coordinate system is consistent with that of Figure 4.9.

4.1.2 Atom Chip Cell

The component joining the MOT and Science cells is a custom, four-port 2.75 in. cube (Kimball Physics), with a custom vacuum shutter (Huntington Mechanical

laboratories) sandwiched between it and the flange of the MOT cell. This shutter provides the ability to isolate the vacuum of the cells from each other. An additional ion pump is connected to the opposite end of the cube from the MOT cell and maintains the science cell vacuum, providing 40 l/s at 7 kV (Varian VacIon Plus) from the same controller as the first. The mounting location allows line-of-sight pumping of the MOT cell and atom dispensers for additional pumping. The bottom of the cube features a viewport providing a clear but distant view of the atom chip surface.

The science cell is a smaller version of the MOT cell, with a double-ended rectangular section of 7.7 cm x 4.6 cm x 4.6 cm, with stainless steel flanges. The bottom flange is a 2.75 in. Conflat and connects to the four-port cube supporting the cell and ion pump. The upper flange is a 3.375 in. Conflat connecting the cell to a custom, multiport flange (McCallister Technical Services). This multiport flange provides six 1.33 in. ports with SMA RF feedthroughs and a 20-pin DC electrical feedthrough that connect to the atom chip.

4.1.3 Atom Source

The MOT cell is supplied with ^{85}Rb , ^{87}Rb , ^{39}K , ^{40}K , and ^{41}K through 2 rubidium and 2 potassium dispensers (SAES and Alvatec). All isotopes are bosonic with the exception of the fermionic ^{40}K , which has a natural abundance of 0.01%. To access this isotope more easily, one of the Alvatec dispensers has been enriched to 7%. The dispensers are mounted to long, rigid copper wire supported by Groove Grabbers (Kimball Physics). The Grabbers are attached to a narrow 4.5 in. diameter spherical octagon (Kimball Physics) and individually connected to four 1.33 in. electrical feedthroughs. The spherical octagon is sandwiched between the 6-way cube and 4.5 in. Conflat flange of the MOT cell, with the dispensers suspended at

the entrance to the rectangular center section of the MOT cell.

Light Induced Atom Desorption

The MOT cell vapor pressure of both rubidium and potassium is dynamically varied through light induced atom desorption (LIAD) by nearly three orders of magnitude on a sub-second timescale. Up to seven 405 nm LED modules (Epitex, L405-66-60-550) totalling 1.8 W, are powered by a lab-built constant current source. These lights are directed at the MOT cell to desorb rubidium and potassium atoms deposited on the cell walls. In ^{39}K , the LIAD process increases the MOT population by well over a factor of 10^2 . In ^{87}Rb , we see increases of up to a factor of 10^4 . The LIAD light is turned off immediately following the MOT loading procedure to allow the vacuum pressure to recover.

4.1.4 Vacuum Quality

The lifetime of magnetically trapped ^{39}K at the atom chip was measured to be about 9 s. The lifetime was previously measured using ^{87}Rb to be about 7 s. The MOT cell vacuum is better than expected given that we activate a dispenser (SAES) every other day for up to 5 min: We observe ^{87}Rb MOT loading time constants on the order of 10 s and ^{87}Rb and ^{39}K magnetic trap lifetimes of about 18 s. We attribute this unexpected performance to a careful vacuum cleaning procedure. The entire vacuum system was baked-out at 100°C for two weeks, limited by the temperature rating of the enriched Alvac dispensers and UHV-grade electrically conductive epoxy used at the chip to make wire connections.

4.2 Laser Cooling System

The first step in cooling an atomic gas to degeneracy is laser cooling in a large-beam collection MOT. The MOT is formed with three pairs of counter-propagating beams forming three perpendicular axes through the MOT cell (one horizontal and two diagonal). The large beams are just under 5 cm in diameter to maximize the MOT loading rate. The counter-propagating beams follow six independent paths (instead of retro-reflected) to avoid shadowing of the cooling light and ensure low cooling temperatures. The MOT is typically operated with a 9–12 G/cm magnetic gradient (strong axis) produced by anti-helmholtz multi-layer coils. These coils are also used for magnetic trapping. The cooling light for rubidium and potassium is combined just before being beam-split into the six paths, allowing the MOT to cool both species simultaneously. Fluorescence from the MOT is used to monitor the atomic samples with an industrial-grade CCD camera (Unibrain) placed directly above the MOT, in conjunction with a set of miniature TV cameras. When the desired number of atoms has been collected in the MOT, we extinguish the cooling light, and then the magnetic gradient before applying a brief (5-12 ms) optical molasses pulse to provide sub-doppler cooling down ($30 \mu K$ for ^{87}Rb), followed by a short (~ 1 ms) optical pumping pulse before loading into the magnetic trap.

The laser cooling of rubidium and potassium is operated on the respective D2 lines of these elements at 780 nm and 767 nm. The laser systems share a similar architecture for producing trap light, however the techniques used for producing repumper, optical pumping and imaging probes are quite different. A master external cavity diode laser (ECDL) is locked to a saturated absorption transmission line: we produce an error signal by using a lock-in amplifier to observe the saturated absorption probe signal at roughly 100 kHz dither frequency of the pump light. The pump light frequency dither is imposed by way of a double-pass acousto-optical mod-

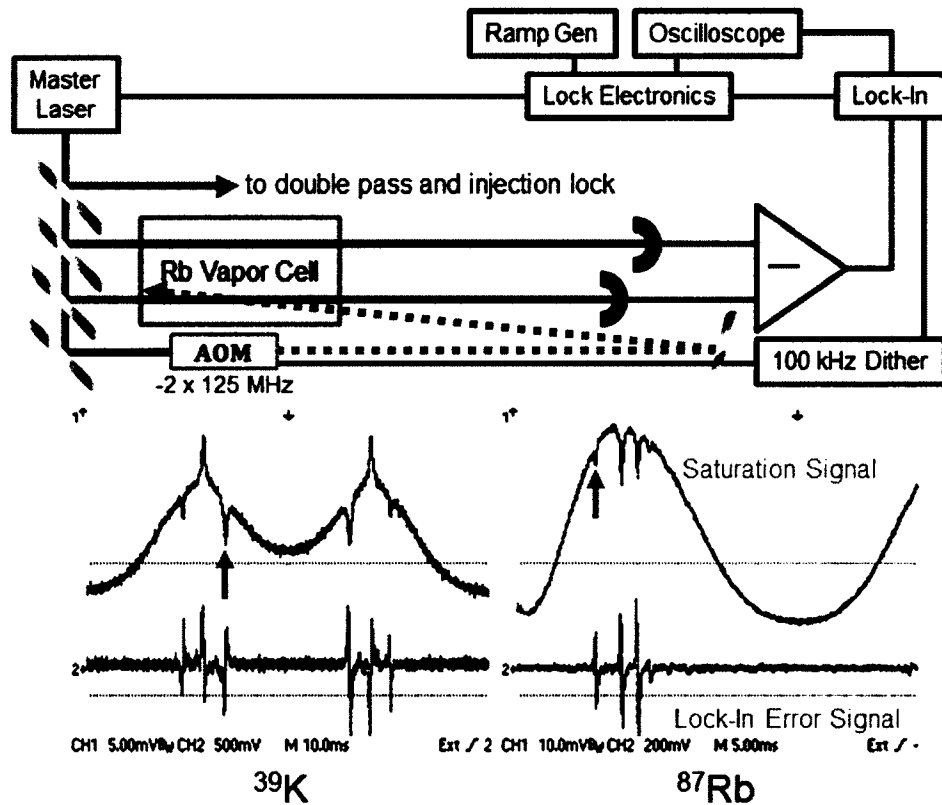


FIG. 4.2: Details of the saturation spectroscopy lock. In both rubidium and potassium, the master laser is split with two *probe* beams directed through a vapor cell and a third into a double-pass AOM. The output of the double-pass pump is directed backwards through the vapor cell, overlapping with one of the probe beams. The two probe beams are incident on photodiodes where the signals are subtracted, and input to a lock-in amplifier. The lock-in amplifier extracts a saturation spectroscopy signal at the 100 kHz dither frequency that modulates the double pass AOM frequency. This error signal is processed by the custom lock electronics and passed back to the Master Laser. In the ^{87}Rb saturation signal, all four excited state transitions can be resolved. However in the case of ^{39}K , the close spacing of hyperfine levels results in an unresolved saturation signal for the excited levels, so that only lower levels $4S_{1/2}F = 1$ and $F = 2$ are resolved. The red arrows indicate the transitions that are used for the master lock.

ulator (AOM) that creates a frequency shift of $+\nu$ on the pump light, but also causes the transmission line of the probe to be offset by $-\nu/2$ from the original saturated absorption transmission line. Some master ECDL light is also sent through another double-pass AOM to injection lock a commercial diode laser, isolated by a Faraday isolator, for a significant laser power increase. This double-pass AOM provides frequency control of the injected laser light, the output of which is sent through an 80 MHz single-pass AOM for amplitude control. The resulting light is then combined with separately generated repumper light to form the MOT cooling beam. Optical pumping and probe imaging beams are derived by picking off light from the trap and repumper beams. These combined beams pass through lab-made optical shutters to provide additional gating and path selection. This scheme provides independent control over the trap, probe and repumper light so that the repumper can be turned off for absorption imaging, but left on for optical pumping and fluorescence imaging.

The combined trap and repumper beams are directed through optical fibers to the apparatus table where they are amplified by lab-built tapered amplifiers (TA) before being sent to the MOT. Shutters placed after both TAs block spontaneous emission during magnetic trapping and transport. All lasers and TAs are isolated from back reflections with Faraday isolators. The laser systems and vacuum apparatus are on separate optics tables to suppress unwanted magnetic, electrical, optical, and mechanical coupling. All beams are directed to the vacuum apparatus table through optical fibers.

The potassium and rubidium cooling beams are combined and then split up along six separate pathways to the MOT cell. Each path contains a 1:5 expansion telescope as the last component before the cell. We use dichroic waveplates ($\lambda/2$ for 767 nm and λ for 780 nm) to independently control the potassium power balancing relative to that of rubidium along each arm of the MOT. A small portion of the combined light is picked off for monitoring with a commercial scanning Fabry-

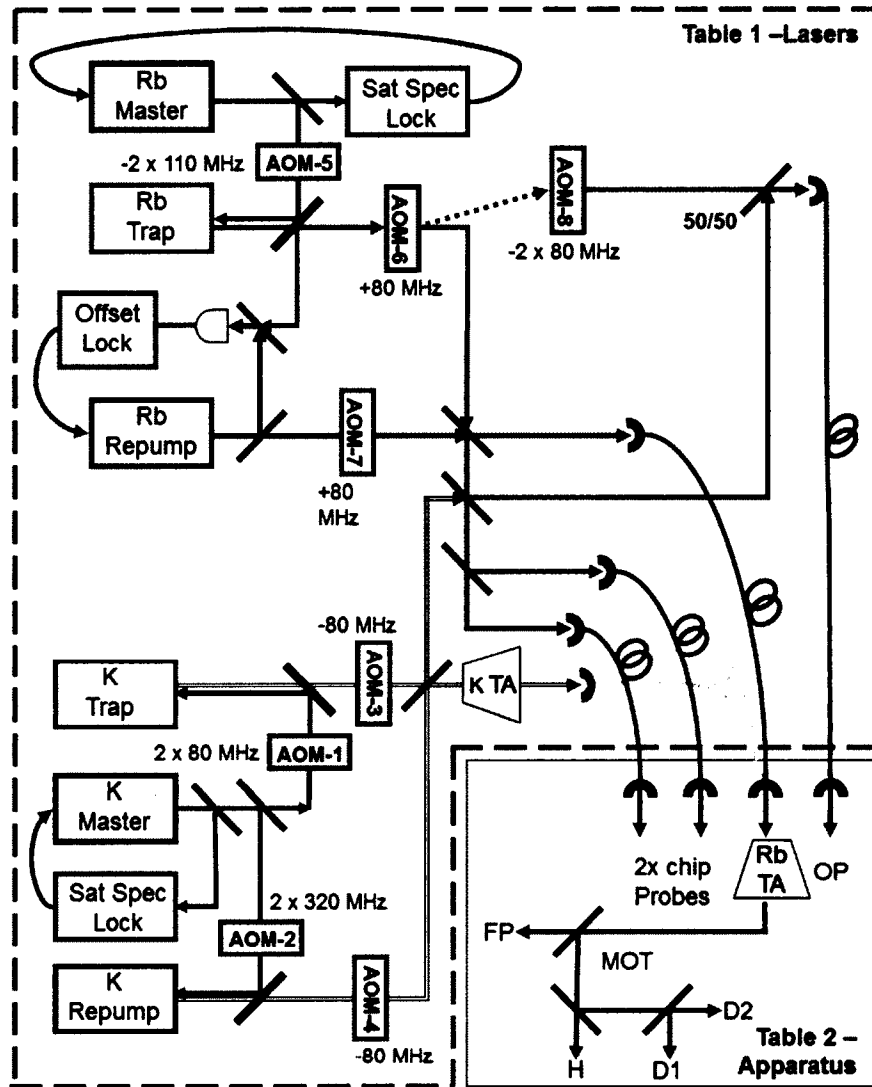


FIG. 4.3: Laser system schematic for operation of the MOT, optical pumping and probe beams for Rb and K. Straight arrows represent free space laser beams. Curved gray arrows represent electrical signals. Gray and gold lines with double loops represent optical fibers. TA: single pass tapered amplifier. FP: Fabry-Perot cavity. OP: optical pumping and absorption probe for the MOT cell. H, D1 and D2: Horizontal and diagonal tapping beams for the MOT. The AOM frequencies indicate the nominal center frequencies of the devices. Note: the gold fiber optic represents the connection of daisy-chaining the single pass potassium TA into the rubidium TA.

Perot cavity to monitor the individual powers of the trapping and repumping lasers of rubidium and potassium simultaneously. This utility also provides a means of monitoring the injection locking of the lasers.

4.2.1 Rubidium

The rubidium laser system pairs two 780 nm ECDL lasers (New Focus) for the trap and repumper. The primary ECDL laser is locked to the $5S_{1/2}, F = 2 \leftrightarrow 5P_{3/2}, F = 3$ saturated absorption line of ^{87}Rb . Mirroring the potassium laser lock scheme, the pump beam is offset so that the ECDL is locked +65 MHz above the transition line. The output of the ECDL is shifted through a -2×110 MHz double-pass AOM for frequency control and subsequently injected into a diode laser (Sanyo DL7150-201W) with an output power of about 50 mW. The output of this injection locked laser is sent through a +80 MHz single-pass AOM for amplitude control and forms the rubidium trap light.

The second 780 nm ECDL laser is locked directly to the master ECDL laser frequency instead of an atomic transition. A small amount of light with parallel polarizations from both ECDL lasers is combined through a 50:50 beamsplitter and directed into a low-cost, high-speed telecom photodiode (Finisar, HFD6180-418) to detect the beatnote between the two optical fields. The resulting microwave signal (~ 6.4 GHz) is converted to a digital pulse train with a limiting amplifier (Hittite, HMC750LP4). The signal is conditioned by a divide-by-8 frequency divider (Hittite, MHC363G8) below 1 GHz and then coupled to a phase-frequency detector (PFD) where it is compared to a reference signal of 796 MHz. The PFD (Hittite, MHC439QS16G) generates an error signal which is feedback through a proportional-integral gain module to the piezo and current drivers of the repumper ECDL. Built by Megan Ivory, this offset locking is very robust with a relative linewidth compa-

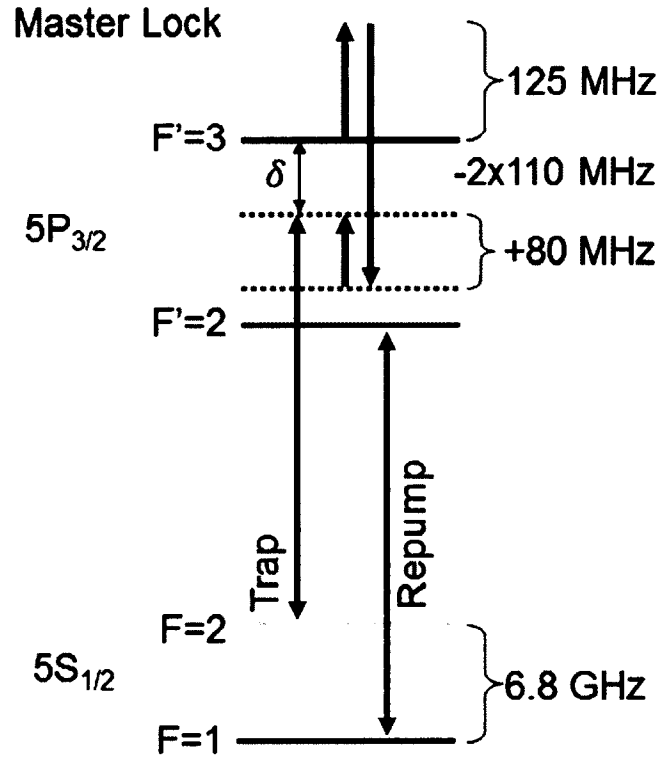


FIG. 4.4: Lock scheme of the rubidium laser cooling system. The master lock is offset from the $|F = 2\rangle$ to $|F' = 3\rangle$ by +125 MHz, highlighted in orange. The trapping light then goes through a double pass AOM centered at 110 MHz for detuning control on the input beam to an injection lock diode laser. Amplitude control is provided by a final 80 MHz single pass AOM. In this system, the repumper is locked through an offset lock system and its own single-pass AOM for amplitude modulation. The $F' = 0$ and $F' = 1$ levels are not shown.

rable to the short term sub-MHz width of the beatnote when the ECDL lasers are free running. The output of the offset-locked ECDL is shifted by a +80 MHz AOM for amplitude control before it is combined with the trap light.

Some of the combined light is used for optical pumping and absorption imaging, however most of the power of the combined beams is coupled via fiber to a 780 nm TA (Eagleyard EYP-TPA-0780-01000) on the apparatus table. This single-pass configuration provides 350 mW of useable power to the MOT. The rubidium cooling light has a typical peak intensity of 1.4 mW/cm² per beam. The system is also capable of producing a ⁸⁵Rb MOT when the ECDL master laser is locked to the $5S_{1/2}, F = 3 \leftrightarrow 5P_{3/2}, F = 4$ saturated absorption line of ⁸⁵Rb, and the reference lock frequency of the repumper offset lock is adjusted accordingly.

Optical pumping light for the $5S_{1/2}, F = 2 \leftrightarrow 5P_{3/2}, F = 2$ transition is sourced from the zeroth order of the trap light single-pass AOM and shifted with a -2×80 MHz double-pass AOM. This light is combined with some repumper light before being direct to the apparatus table via optical fiber to preferentially populate the $F = 2, m_F = +2$ state after the optical molasses pulse in preparation for magnetic trap loading.

4.2.2 Potassium

The potassium laser system is anchored by a single 767 nm ECDL master laser (New Focus) locked to the ³⁹K $4S_{1/2}, F = 2 \leftrightarrow 4P_{3/2}$ transitions. Following the ⁸⁷Rb laser system description, the pump beam in the saturation spectroscopy is offset by $\nu = +2 \times 90$ MHz with respect to the probe, implying that the lock point of the ECDL master laser is $-\nu/2 = -90$ MHz from the transition line. Master laser light is split between two injection lock diode lasers (Eagleyard EYP-RWL-0770-00025) simultaneously to generate the trap and repumper beams as shown in

Figure 4.5. Two double-pass AOMs control the detuning of each injection beam. One laser is offset by $+2 \times 77.5$ MHz (80 MHz AOM) to form the trap light, while the other is offset by $+2 \times 310$ MHz (310 MHz AOM) to become the repumper. Amplitude control is provided by a single-pass AOM for both lasers. Taking the -1 order (-80 MHz) of each, the beams are then combined and sent via fiber to the apparatus table. Approximately 3 mW of combined light is injected into a double-pass TA (Eagleyard EYP-TPA-0765-01500) setup to provide ~ 300 mW of cooling light to the MOT. As much as 500 mW has been generated with careful tuning of the system.

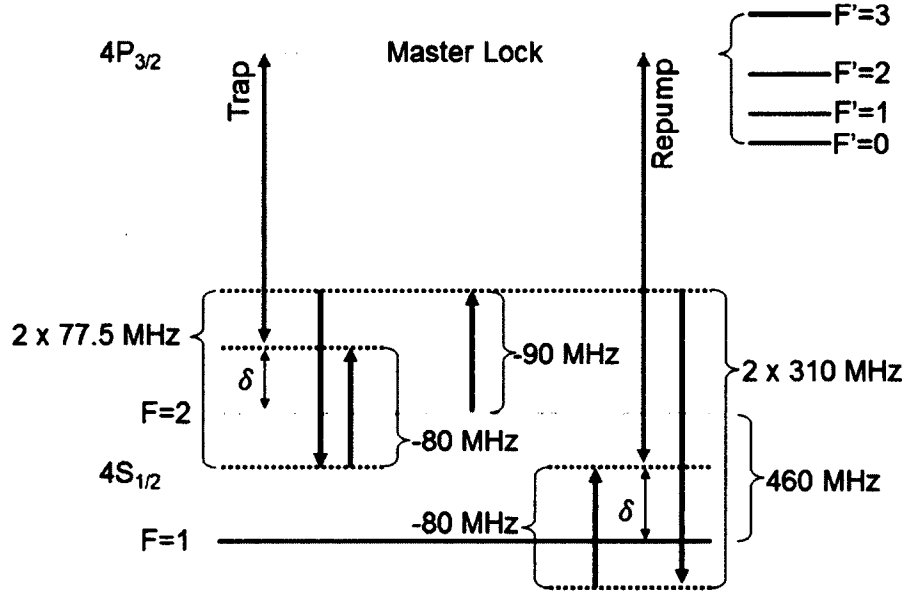


FIG. 4.5: Lock Scheme of the Potassium laser cooling system. The Potassium system is quite a bit more complicated than the canonical Rubidium system. The master laser is offset from the $|F = 2\rangle$ ground state to the unresolved $4P_{3/2}$ excited states by -90 MHz, highlighted in orange. From here, the *trap* laser goes through a double pass AOM centered on 77.5 MHz before being coupled into an injection lock amplifier. Amplitude modulation is provided by an 80 MHz single pass AOM. Alternately, the *repump* laser is detuned from the master lock by a 310 MHz double pass AOM before it is coupled into a second injection lock diode amplifier. Amplitude modulation is provided by an independent 80 MHz AOM.

We find that a 2:1 ratio of trap to repumper light is necessary for reliable opera-

tion of the ^{39}K MOT. In principle, our laser system could be used to target ^{40}K (^{41}K) by replacing the 80 MHz trap double-pass AOM with a 320 MHz (110 MHz), and locking the ECDL master laser to the cross-over transition of ^{39}K . A small portion of the combined cooling light is split off and mixed with rubidium optical pumping and probe light for similar functions. Lab-built mechanical shutters are used to gate these signals before they are sent to the apparatus table via optical fibers. Further details on the potassium laser cooling system are provided in Chapter 8.

Double Pass Tapered Amplifier

Initially, the potassium TA was installed on the laser table and seeded with ~ 15 mW of combined cooling light to generate ~ 200 mW. The output was coupled via fiber to the apparatus, however it only supplied up to 60 mW to the MOT. In order to raise the atom number, we resorted to “daisy-chaining” the potassium light into the rubidium TA. Due to the mismatch of the 767 nm light to the 780 nm-centered gain curve of the rubidium TA, an injection power of 30 mW only resulted in a total cooling power of 200 mW. This configuration prevented the independent operation of potassium and rubidium species but was necessary to raise the atom number sufficiently high to image magnetically trapped ^{39}K on the atom chip.

Our potassium TA was reconfigured into a double-pass system (shown in Figure 4.6) which is currently providing ~ 300 mW total cooling power from a 3mW seed based on the work of [63] and [64]. This system provides enough power for the ^{39}K to be cooled and trapped simultaneously and independently of rubidium isotopes. The tapered amplifier system is described in much more detail in Chapter 8.

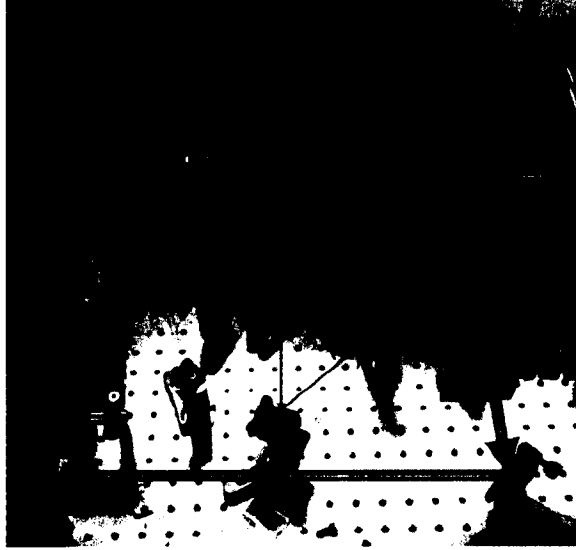


FIG. 4.6: Double Pass Tapered Amplifier Setup. The seed light is coupled via fiber into the rejection port of a faraday optical isolator. ~ 3 mW is sent into the TA in reverse and amplified to ~ 30 mW. This power is monitored via a photodiode on a pick off beam, and then retro-reflected back into the TA. The second pass produces up to 300 mW of usable light for the ^{39}K cooling beams.

4.3 Magnetic Trapping and Transport

The second step in the ultracold quantum gases production process is to load the MOT-cooled atomic cloud into a magnetic trap in preparation for transport to the science cell. As shown in Figure 4.7, we extinguish the MOT light, quickly turn off the MOT anti-Helmholtz coil current (referred to as the MOT coils), and subsequently turn the MOT light back on for 5 – 12 ms to further cool the atomic cloud through optical molasses (see also Figure 6.2 for additional details). Next, we apply a ~ 1 ms pulse of optical pumping light to preferentially populate the $F = 2, m_F = 2$ hyperfine state, just before quickly turning on the magnetic trap at 60 G/cm (strong axis) with 70 A in the MOT coils. The 30 G/cm (weak axis) vertical gradient is sufficient to counter gravity for the $F = 2, m_F = 2$ state of ^{87}Rb , but not the $F = 2, m_F = +1$ or $F = 1, m_f = -1$ state, which ensures a pure spin-polarized ^{87}Rb cloud. In ^{39}K , both equivalent states would be trapped by the 30

G/cm gradient, however the optical pumping process is sufficiently efficient due to smaller cloud size and lower atomic density to produce a magnetic trap of primarily $F = 2, m_F = 2$ atoms.

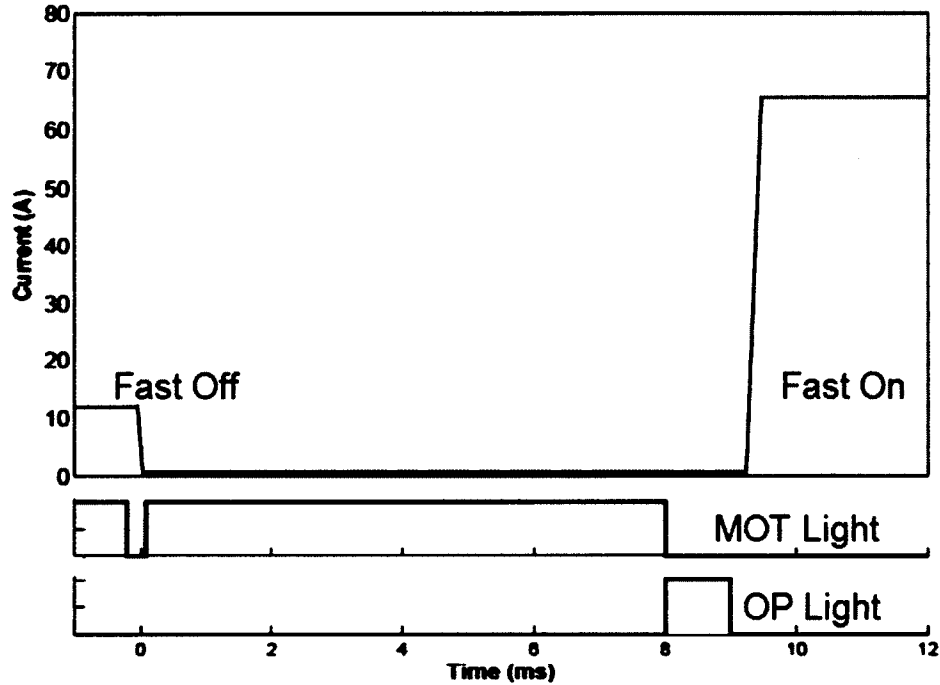


FIG. 4.7: MOT coil current switching scheme for loading the magnetic trap. (Top) Diagram of target MOT coil current versus time for the MOT, fast turn-off, molasses, fast turn-on and magnetic trap stages. This diagram is a representation of the desired current as programmed by the Adwin control software. (Bottom) Timing diagrams for the Rb MOT and molasses light and the Rb optical pumping (OP) light. Figure 6.2 and Chapter 6 discuss this scheme in greater detail.

Atoms are transferred from the MOT cell magnetic trap to the atom chip in the science cell by a transport system comprised of seven staggered quadrupole magnetic traps without any moving parts. Seven identical anti-Helmholtz coil pairs are interleaved over the 60 cm L-shaped path from the MOT to the atom chip: four from the MOT cell to the corner and three from the corner up to the science cell. The transport coil pairs overlap each other according to the arrangement shown in Figure 4.8 (a). This configuration ensures that a magnetic quadrupole potential can be translated along the common weak axis of the coils through careful ramping of

the the currents of three adjacent coil pairs. A large Helmholtz-style push coil pair (labeled P1 in Figure 4.1), which produces a quasi-uniform magnetic field along the z-axis, assists the transfer of atoms from the magnetic trap into the first quadrupole trap of the transport system. Similarly, a single large water-cooled push coil (labeled P2 in Figure 4.1), positioned above the atom chip, produces a vertical magnetic field to assist with loading atoms into the micro-magnetic trap of the atom chip located 1.5 cm above the center of the final transport pair.

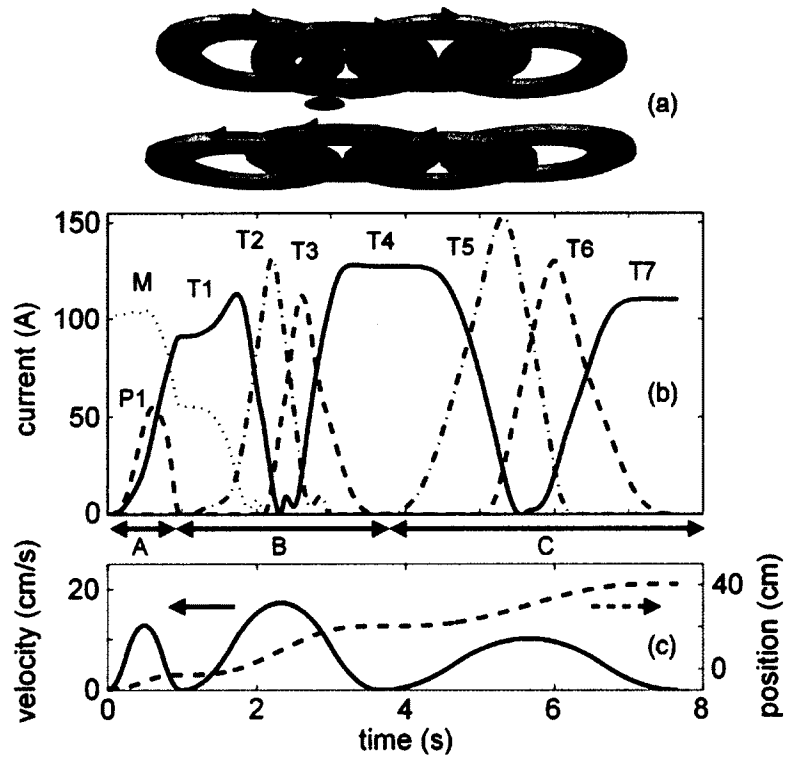


FIG. 4.8: Transport system current sequence. (a) Diagram of the transport coils, demonstrating how the coils overlap. This configuration ensures that a magnetic quadrupole potential can be translated along the common weak axis of the coils through careful ramping of the the currents of three adjacent coil pairs. (b) Coil current sequence. M: magnetic trap current provided by power supply PS-1. P1: Push coil current (MOT cell). T1-T7: Transport coil currents. The linestyle (dotted, dashed, solid, and dash-dot) represents which of four power supplies is used to drive the labeled coil. The loading sequence from coil T7 to the atom chip trap is not shown (involving push coil P2 and the chip magnetic fields). (c) Simulated velocity and position trajectories for the current sequence. (a) Magnetic trap to transport trap handoff. (b) Transport to corner. (c) Transport from corner to atom chip.

4.4 Atom Chip

The atom chip is the primary location of experiments in this apparatus. It features a number of DC and RF magnetic fields for producing a micro-magnetic trap for RF evaporation to quantum degeneracy, as well as for future experiments. Additionally, the atom chip has several optical probes and imaging system directed at it for *in situ* and time-of-flight measurements. The tight confinement of the chip trap ensures fast re-thermalization times for rapid RF evaporation. The atom chip is well suited for experiments requiring highly elongated or pseudo-1D traps, RF near-field potentials, or a nearby surface for atom-surface force studies. Generally, a more advanced experiment would require modification to the atom chip and not the entire apparatus.

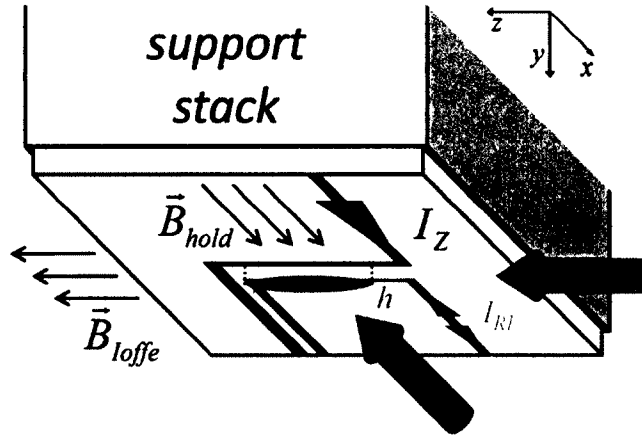


FIG. 4.9: Atom chip Z-wire diagram. The magnetic field of the Z-wire current I_z and the external bias magnetic field B_{Hold} generate a cigar-shaped Ioffe-Pritchard style trap, represented by the blue cloud, at a distance h below the central Z-wire segment. B_{Ioffe} is directed along the long axis of the trap and sets the magnetic field at the bottom of the trap. The red arrows indicate absorption imaging beams. While the representation is not to scale, the coordinate system matches that of Figure 4.1.

In order to produce a BEC, the atoms are confined in the Z-wire trap produced by a thin Z-shaped wire on the chip, as shown in Figure 4.9. The central portion of the wire is $50 \mu\text{m}$ wide, while the endcap leads are $200 \mu\text{m}$ wide. The wire has

a vertical thickness of just over $3\ \mu\text{m}$. A cigar-shaped Ioffe-Pritchard style trap is produced directly below the Z-wire, when a DC current is directed through it in combination with an external magnetic bias field B_{hold} , parallel to the plane of the chip and transverse to the central wire segment. The endcap leads ensure that the trap minimum occurs at non-zero magnetic field, and we add a longitudinal magnetic field B_{Ioffe} , parallel to the central wire, to increase this magnetic minimum. The trap is harmonic in all directions: for a wire current $I_Z = 1\ \text{A}$, $B_{hold} = 20\ \text{G}$, and $B_{Ioffe} = 4.9\ \text{G}$, the calculated axial and radial trap frequencies for Rb (K) are $\omega_z = 2\pi \times 9.3\ \text{Hz}$ ($2\pi \times 13.9\ \text{Hz}$) and $\omega_r = 2\pi \times 1.1\ \text{kHz}$ ($2\pi \times 1.6\ \text{kHz}$), respectively; the trap is $100\ \mu\text{m}$ from the chip surface. We use a U-shaped wire to produce a RF magnetic field in the 1-20 MHz range for forced evaporation of chip-trapped atoms. In addition to the U and Z wires, the atom chip features a number of additional wire structures for future manipulation of the trapped atoms with magnetic biases, gradients, and RF fields that are not shown in Figure 4.9.

The chip is connected by screws at its corners to an aluminum support stack, which is mounted on a vacuum flange above it. This structure serves as a heatsink for power dissipated in the chip wires and as a support for the wire leads that feed the chip. A small amount of vacuum compatible epoxy (model: FO-EPXY-UHV, Accu-Glass Products, Inc.) bonds the chip to the stack for improved thermal conductivity. The support stack is attached to a multiport flange that provides DC and RF (SMA) electrical connections. Kapton-insulated wires and coaxial cables connect the electrical feedthroughs to the chip. These wires are attached to the backside of the chip with vacuum-compatible, electrically conductive epoxy (EPO-TEK H21D, Epoxy Technology, Inc.).

The Z-wire trap is powered by a fast, high stability, precision bipolar current source (High Finesse, BCS 5/5). In order to suppress noise and ground loops, the current source is galvanically isolated from the analog control signal ground. One

side of the chip wire is explicitly grounded to the optics table and the multiport flange. An over-current protection interlock system ensures that the Z-wire current I_Z remains at or below 1 A for at most 10 s, which we have determined to be safe based on resistive heating measurements. Two compact Helmholtz-style coil pairs (blue in Figure 4.1), positioned a few millimeters from the science cell and centered on the chip, provide the holding field B_{hold} along the x-axis and a Ioffe field B_{Ioffe} along the z-axis, as shown in Figure 4.9. A single horizontal coil (blue in Figure 4.1) above the chip provides a modest vertical magnetic bias field. These three bias coils are powered by high speed bipolar current sources (Kepco BOP series) for rapid modulation and turn-off on time scales of 100-200 μ s.

4.4.1 RF Evaporation System

A 16 dBm RF signal is generated by a direct digital synthesis function generator (Berkeley Nucleonics, model 645). We control the RF amplitude with an analog voltage controlled attenuator and a TTL RF switch. The RF signal is sent to the chip via an isolation transformer and a 50 Ω series resistance for impedance matching. Forced evaporation frequency sweeps of 19 to 3 MHz are produced in linear stages by frequency modulating the RF source with an analog ramp signal. A RF amplifier is not necessary due to the proximity of the atoms to the U-wire.

4.5 Imaging

We use absorption imaging for *in situ* and time-of-flight measurements of atomic cloud parameters, such as temperature, density and atom number. As shown in Figure 4.9, probe lasers are directed parallel to the chip along the axial and radial axes to image the atoms with CCD cameras. We employ industrial grade cameras (Unibrain, Fire-i 530b and Fire-i 701b) with the CCD chip cover glass removed to

avoid interference fringes from it. The cameras are each fitted with 1:1 achromatic doublet pair imaging systems (Thorlabs, MAP10100100-B) with a 10 cm imaging distance. While these probe lasers can be used for fluorescence imaging of very small clouds, we typically use absorption imaging for high fidelity measurements. We employ a double-shot imaging method where a reference image without atoms is taken 0.3-0.5 s after taking an image of atoms. Beer's Law can be used to extract an accurate measure of atom number and density by dividing the absorption image by the reference image. This technique minimizes non-atomic variations in between the imaging and reference probe pulses.

Despite the Gaussian laser profiles that are produced from the single mode polarization maintaining fibers, we find that the probes that impinge upon the CCDs contain several interference fringe patterns. The glass cell presents four non-anti-reflection coated surfaces, and we see interference fringes due to these, though they are quite stable over the double-shot imaging duration. Experimentally, we find that the reflections between the imaging systems and other optical elements in the absorption probes' paths, such as the glass cell, produce high-frequency interference fringes that are not stable over the course of the double-shot period. However, careful adjustment of the imaging systems' orientation and position can minimize these fringes significantly.

We monitor the MOT with a top view CCD camera similar to those used for the atom chip. The camera is used for aligning the MOT with the magnetic trap and for temperature measurements of the cold atoms. This CCD camera can also be used for absorption imaging of MOT-region atoms using resonant light directed along the optical pumping laser path with which it is aligned. We also use two black and white TV cameras for general monitoring of the MOT.

4.6 Optical Dipole Trapping

The apparatus includes two optical dipole traps: a low power trap in the vicinity of the atom chip, and a high power crossed dipole trap in the MOT cell. The chip dipole trap is based on a 1.5W 1064 nm fiber laser (NovaWave Technologies). We use about 1 W of optical power, controlled by an 80 MHz AOM, to form the trap. The output power of the laser is sufficiently stable that no active power stabilization is necessary. The chip dipole trap has an estimated trap depth of 20 μK for a 60 μm waist and is aligned with the main axis of the Z-wire trap for approximate mode-matched transfer between them. Conveniently, a $\lambda/2$ waveplate and a polarizing beamsplitter cube can be used to direct this dipole trap light at the chip region or the MOT cell.

The crossed dipole trap in the MOT cell is formed by two lasers: a 10W 1064 nm Nd:YAG laser (Spectra-Physics, model 3800, on loan from C. Sukenik, ODU) and light re-directed from the 1064 nm fiber laser. We use about 6 W of the Nd:YAG light, controlled by a high-power 40 MHz AOM, for the dipole trap. We actively stabilize the Nd:YAG laser power to better than $\pm 0.6\%$ (pk-pk) over a bandwidth of 10 kHz. We use a 30 cm achromat lens to focus the Nd:YAG laser down to a somewhat elliptical waist with a mean radius of 120 μm to form a dipole trap. We form a crossed dipole trap by folding the trapping beam back on itself through a second 30 cm lens, but with a small angle between the two beams. The broadband nature of the laser and the 1.4 m distance over which the laser is folded back on itself combine to partially suppress the formation of an optical lattice at the trap: Based on first-order coherence measurements, we estimate the lattice fringes to be on the order of 20% of less of the total trap laser intensity and are working on additional mechanisms to further suppress these. In the limit of no lattice fringes, the trap has an estimated depth of 50 μK . Optionally, the 1064 nm fiber laser can

be focused onto the Nd:YAG trap to form a tighter crossed dipole trap. All of the dipole laser beams are directed horizontally into the MOT cell at small angles from the two horizontal MOT beams.

We have successfully loaded near-degenerate thermal ^{87}Rb atoms from the Z-wire trap into the atom chip dipole trap, which we are using for experiments in the vicinity of the atom chip. In the MOT cell, we have successfully loaded atoms into the crossed dipole trap from the magnetic trap by operating both traps simultaneously and performing RF evaporative cooling, following the method of Spielman and Porto [65], we obtain a phase space density of 10^{-4} with up to 6×10^6 ^{87}Rb at μK -level temperatures and a 14 s lifetime in the retro-reflected 6 W dipole trap.

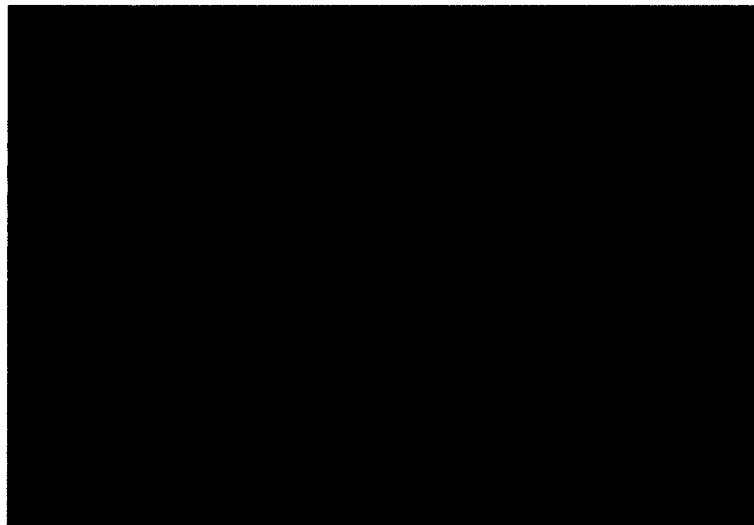


FIG. 4.10: Dipole Trap using the 1W Novawave 1064nm Fiber Laser in the MOT cell. The dipole trap was loaded directly from the ^{87}Rb molasses stage, with a beam waist of $54\mu\text{m}$.

It is worth noting that before the arrival of the Spectra-Physics 10W laser for use in the MOT cell, the Novawave 1.5W Fiber laser was used to load ^{87}Rb atoms into a single-pass dipole trap directly from the MOT. Though the number of trapped atoms were not very useful at the time, the technique was established early on, provided dipole trap experience, and paved the way for both current optical

dipole traps. The first evidence of this MOT to dipole trap loading is presented in Figure 4.10.

CHAPTER 5

System Performance

The apparatus functions as designed and produces quasi-pure BECs within a 40 s cycle time. I will first outline the performance of the apparatus from MOT to BEC on the atom chip for ^{87}Rb and then present details on the dimple trap of our Z-wire chip trap. I will then describe the ongoing progress with ^{39}K from MOT to atom chip magnetic trap.

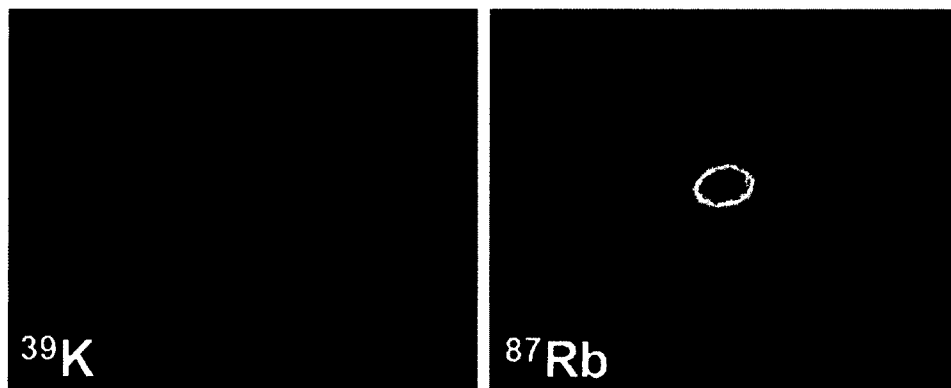


FIG. 5.1: Simultaneously MOT-trapped rubidium and potassium were imaged independently using the same imaging system (same vantage point and resolution).

5.1 Rubidium: MOT to BEC

The MOT collects several 10^8 ^{87}Rb atoms within 25 s at a temperature of about $60\ \mu\text{K}$ with a detuning of $21\ \text{MHz} \approx 3.5\Gamma$ and a peak intensity per beam of $1.4\ \text{mW}/\text{cm}^2 \approx 0.8I_{sat}$; Γ and I_{sat} are the linewidth and saturation intensity for the D_2 cycling transition. After turning off the MOT light and magnetic gradient, we apply a 5-12 ms molasses stage by turning the MOT light back on at reduced power and a detuning of $56\ \text{MHz} \approx 9.2\Gamma$ with the repumping power reduced. As shown in Figure 6.2, we then apply a 1.1 ms optical pumping pulse to preferentially populate the $F=2$, $m_F = 2$ hyperfine ground state and load up to 3×10^8 atoms into the magnetic trap at $80\ \text{G}/\text{cm}$. At this point the atoms have a temperature of about $50\ \mu\text{K}$, a phase space density (PSD) of 2×10^{-6} , and a collision rate of $6\ \text{s}^{-1}$. The atoms are then transferred to the transport system, which conveys them around the corner of the tube connecting the two cells and up to the atom chip in the science cell in just under 8 s.

We load over 5×10^6 ^{87}Rb atoms into the chip Z-wire trap by adiabatically ramping up the chip current to $I_Z = 1\ \text{A}$ and the magnetic holding field to $B_{hold} = 20\ \text{G}$ while slowly turning off the transport quadrupole trap and push coil over the course of 450 ms. We also apply an axial magnetic field $B_{Ioffe} = 4.9\ \text{G}$ to protect against spin-flip loss from low-frequency RF noise. Once the atoms are fully loaded into the chip trap, the PSD is 5×10^{-6} with a peak collision rate of at least $30\ \text{s}^{-1}$ per atom. We observe a chip trap lifetime of about 7 s. Next, we compress the atoms to increase the collision rate by ramping up the holding field to $B_{hold} = 46.4\ \text{G}$, resulting in a radial trapping frequency (calculated) of $\omega_r = 2\pi \times 4.5\ \text{kHz}$. The compression occurs over 1 s and results in some evaporation, yielding a PSD of 8×10^{-6} with $4 - 5 \times 10^6$ atoms. We turn on the RF evaporation knife produced by the U-wire current I_{RF} at 19 MHz during the chip loading and begin to ramp it

down after the compression stage.

After reaching a PSD of 10^{-2} with 3×10^5 atoms, we relax the chip trap by ramping down B_{hold} to 20 G to produce a more relaxed trap at $100 \mu\text{m}$ from the chip surface. We perform the final evaporation to BEC in the relaxed trap by ramping the RF knife from 3.8 MHz down to 3.4 MHz over the course of 2 s, with the final 50 kHz covered in 0.8 s. The entire evaporation process takes 6 s from compression to BEC. Figure 5.2 shows the phase space density (PSD) as a function of atom number for the evaporative cooling path of ^{87}Rb in the Z-wire trap.

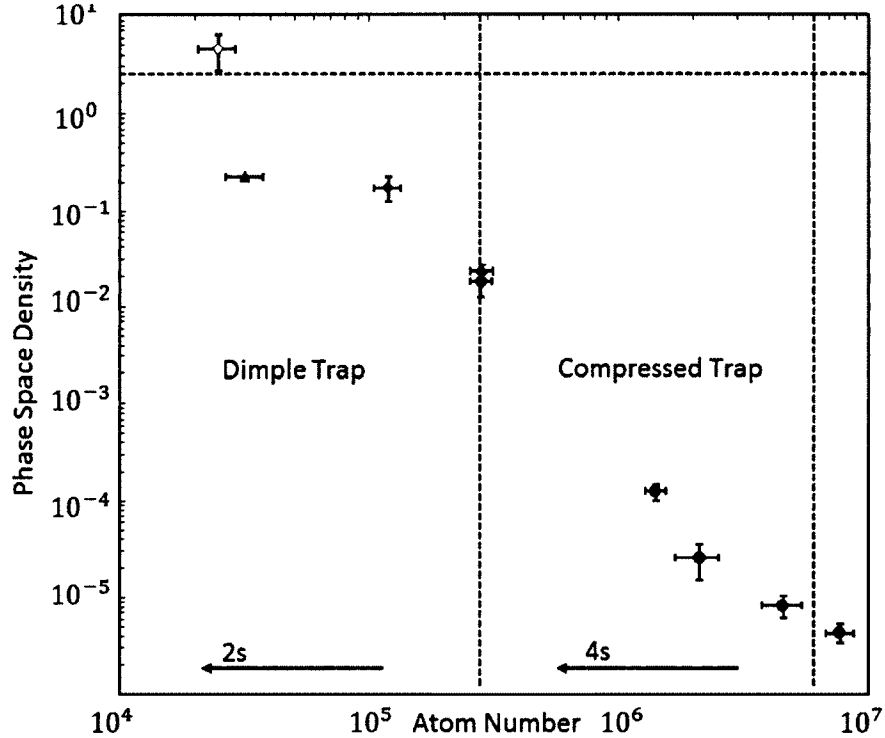


FIG. 5.2: Evaporative cooling path to ^{87}Rb BEC in the Z-wire trap. Plot of phase space density as a function of atom number from the initial loading into the Z-wire trap, through 4 s of RF evaporation in the compressed trap, to the final 2 s of RF evaporation in the dimple trap to quantum degeneracy. The final point above the BEC threshold has been obtained using the same semi-classical definition for PSD as the other points. The outlying triangular point represents the highest achievable phase space density before the dimple was discovered and leveraged.

We observe the BEC transition at $T \sim 0.3\mu\text{K}$ with $2 - 4 \times 10^4$ atoms and

produce quasi-pure BECs with 10^4 atoms.

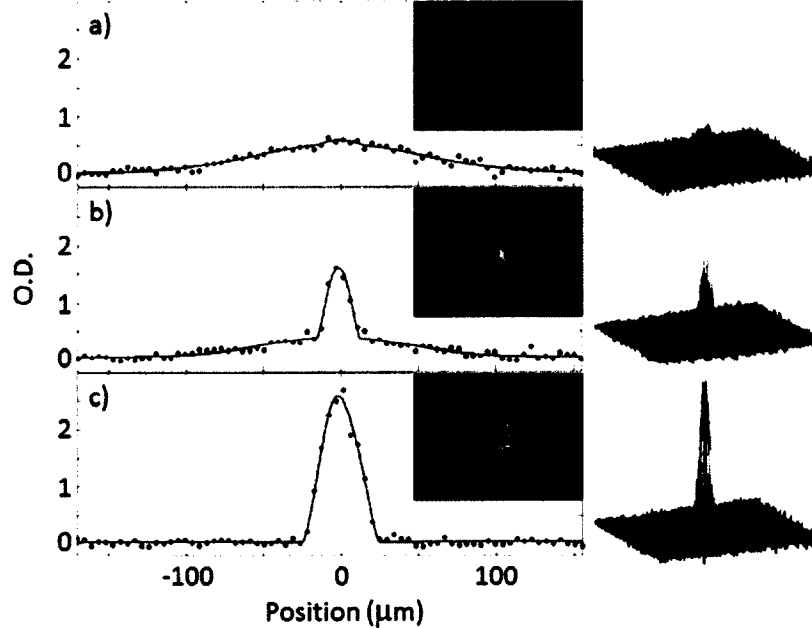


FIG. 5.3: Three views of the transition to quantum degeneracy in ^{87}Rb including optical density cross-sectional plots, and 2D and accompanying 3D absorption images. (a) Thermal atoms with $N_{Total} = 3.7 \times 10^4$ at $T = 0.44(3)\mu\text{K}$. (b) Partially condensed atoms with $N_{BEC} = 3.6 \times 10^3$ and $N_{Thermal} = 1.6 \times 10^4$ at $T = 0.28(2)\mu\text{K}$. (c) A quasi-pure BEC with $N_{BEC} = 1.3 \times 10^4$. Inset images of the BEC show the signature trap aspect ratio inversion while the thermal cloud has an isotropic momentum distribution. The cross-section plots show the bi-modal distribution of the atomic momenta as the BEC emerges from the thermal Gaussian cloud. The red line is a bi-modal fit using Gaussian and Thomas-Fermi distributions integrated along the optical probe axis (x-axis) and is provided merely as a guide for the eye. These fits were provided by M. Ivory.

5.2 Dimple Trap

Atom chip micro-magnetic traps frequently exhibit potential roughness features, and our Z-wire trap is no exception. Evaporation in the compressed trap quickly loses efficiency at temperatures below $3 \mu\text{K}$ (as measured after decompression to the relaxed imaging trap, discussed in Section 4.4) due to the presence of a small localized potential well, or dimple in the magnetic potential. These dimples

cause density irregularities that are visible as faint clumping in the atomic density distribution along the axial trapping potential. These irregularities impede the thermalization processes in the axial direction and can lead to heating when the trap is decompressed.

By applying a modest magnetic gradient along the Z-axis of the trap using coil pair T7 of the transport system, the atomic cloud can be centered on the largest dimple present. By performing this action at the end of the compressed trap stage, we find that it is sufficient to push most of the atoms into this dimple. While the dimple is a little under $2 \mu\text{K}$ deep, it benefits from a relatively high axial trapping frequency: we measure the radial trapping frequencies of this dimple to be $\omega_z = 2\pi \times 53\text{Hz}$ and $\omega_r = 2\pi \times 1.04\text{kHz}$, respectively, by observing axial and radial oscillations of excited clouds. The final evaporation benefits from enhanced rethermalization due to the tight axial confinement of the dimple. In Figure 5.2, the outlying triangular point represents the result of the evaporation path before the discovery of the dimple feature.

5.3 Potassium: MOT to Atom Chip

We have laser cooled a sample of ^{39}K atoms, loaded them into the magnetic trap, transported them to the atom chip, and successfully loaded them into the Z-wire trap. We operate the potassium MOT in two stages: a collection stage (KMOT) uses far-detuned trapping light to maximize the number of trapped atoms, after which a short stage of near-detuned trapping light further cools and compresses the atoms (CMOT) to $70 \mu\text{K}$ for loading into the magnetic trap. Both MOT stages use a magnetic gradient of 8 G/cm . Table 5.1 summarizes the optical parameters of the potassium MOT operation.

After fast turn-off of the MOT coils, we use a 1.5 ms optical pumping pulse

Stage	Time	δ_t	δ_r	I_{tot}	$I_t : I_r$	T (μ K)
KMOT	10-30s	-2.8	-3.6	18	2:1	1000
CMOT	0.1s ramp	-0.8	-3.6	11	12:1	≤ 70
1D MOT	20ms	-2.1	-3.3	10	2:1	-

TABLE 5.1: ^{39}K Cooling Parameters - The trap and repumper lasers were tuned to the $4S_{1/2}$ to $4P_{3/2}$ transitions, and their detunings given by δ_t and δ_r , resp. in terms of the transition linewidth, $\Gamma = 6.1\text{MHz}$. The total and relative intensities, I_{tot} and $I_t : I_r$ are given in units of $I_{sat} = 1.8\text{mW/cm}^2$.

to preferentially populate the $|F = 2, m_f = +2\rangle$ state and then quickly load the atoms into the magnetic trap. Once in the magnetic trap (60 G/cm), the atoms have a temperature of about 60 μK . The mechanism that causes the extra 10 μK of cooling is unknown at this point. The atoms are then transferred to the transport system, delivered to the chip region and loaded into the chip Z-wire using the ^{87}Rb procedure.

Successful chip loading requires low temperatures and large atom numbers: the image in Figure 5.4 was obtained with a large ^{39}K MOT enabled by increasing the total MOT trapping power to 200 mW by seeding the fiber-coupled output of the single-pass K tapered amplifier into the Rb tapered amplifier for further amplification. We capture approximately 6×10^6 ^{39}K atoms in the MOT magnetic trap for transport to the chip where nominally 6×10^3 atoms are transferred in to the atom chip micromagnetic trap (compare to the roughly 5 million ^{87}Rb atoms).

Imaging such a small number of atoms requires extreme patience and cunning. We image the atoms at the chip trap by applying a circularly polarized, retro-reflected, red-detuned probe laser along one of the absorption imaging paths and observing the fluorescence with the camera transverse to the beam. We refer to this method as 1D MOT imaging, as the setup mimics a MOT with two counter-propagating trap beams and a magnetic field minimum provided by the Z-wire trap ($I_Z = 1\text{A}$, $B_{hold} = 11.6\text{ G}$, $B_{Ioffe} = 2.5\text{ G}$). Figure 5.5 illustrates the 1D MOT

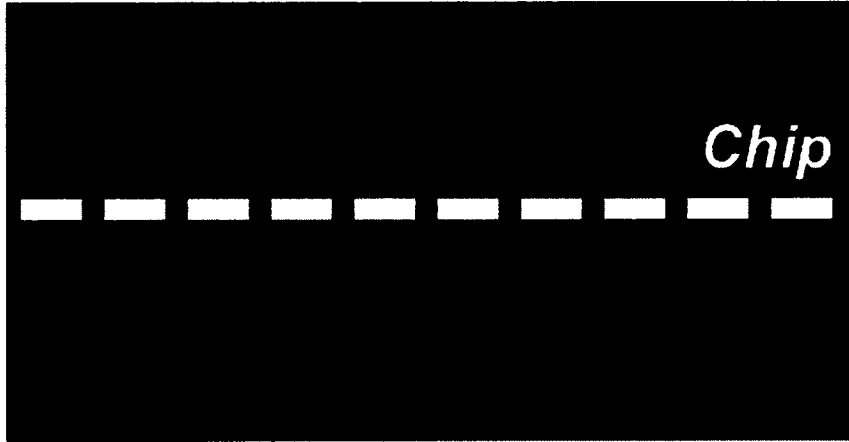


FIG. 5.4: Fluorescence Image of 6×10^6 ^{39}K 1D Chip MOT. This fluorescence image was created by directing circularly polarized light horizontally across the atom cloud and retro reflecting the beam back in the opposing direction to create a 1D MOT. The atom chip provides the conservative magnetic potential.

imaging technique, including the magnetic field lines provided by the atom chip Z-wire.

We observe a Z-wire trap lifetime of about 9 s for ^{39}K , comparable to that of ^{87}Rb lifetime (12 s as of April 2015). Figure 5.6 show the exponential decay of detected ADC counts as a function of Z-wire trap hold time.

5.3.1 Atom Number Analysis

As fluorescence imaging was our only option due to power limitations, extracting the atom number from the 1D MOT image was somewhat tedious. First the camera was calibrated using a well known laser power and attenuation factor to define the CCD output as 0.760 ± 0.128 counts per photon. As the atoms emit photons in all directions and the camera captures only a fraction of them, we must

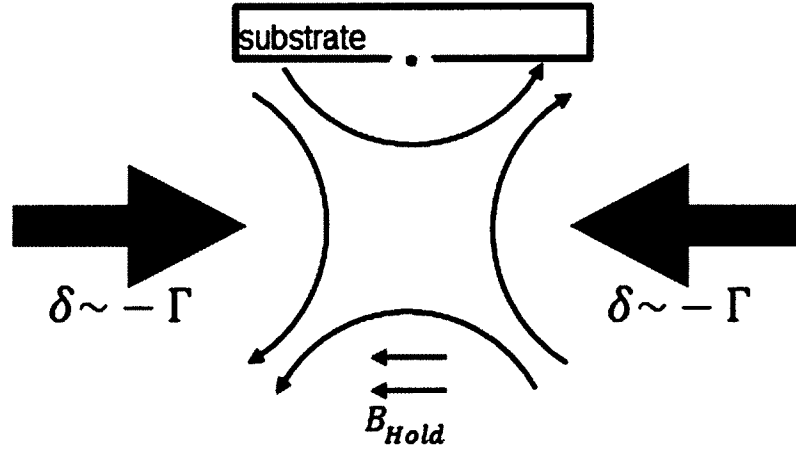


FIG. 5.5: Diagram of the 1D chip MOT technique. Although the diagram is upside-down from the real life orientation of the atom chip, the principles remain the same. Opposite circular polarization is applied through careful alignment of a retro reflection. The magnetic trap created from the combination of the atom chip and B_{Hold} provides the spatially varying detuning necessary to mimic a traditional MOT.

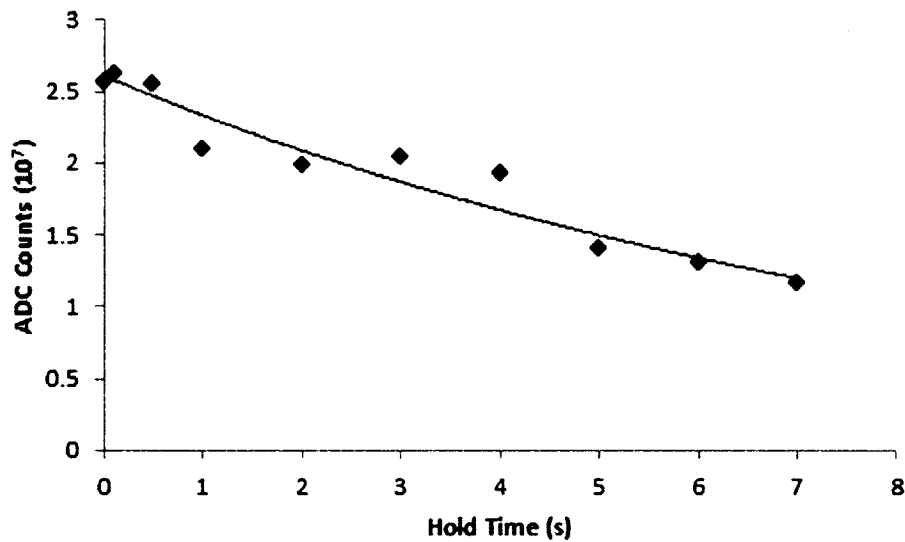


FIG. 5.6: Lifetime of the ^{39}K chip trap as recorded using the 1D chip MOT imaging technique. The fit gives a lifetime τ of 8.9s. This is consistent with the ^{87}Rb lifetime of 7s recorded two years prior to this data set, and a more recent lifetime of 12 s reported in April 2015.

compute the collection efficiency from the solid angle that the camera sees

$$\frac{A_{aperture}}{A_{sphere}} = \frac{\pi r^2}{4\pi L^2} \quad (5.1)$$

where r is the radius of the camera lens and L is the atom-to-lens distance. For this camera, the collection efficiency was $(3.53 \pm 0.04) \times 10^{-3}$. The image itself was imported to MATLAB for analysis, and the total number of ADC counts from the atom cloud was computed to be 1.688×10^6 , which together with the counts per photon and collection efficiency gives a total count of 6.2863×10^8 photons emitted by the cloud. The remainder of the analysis involves the scattering rate defined by

$$\gamma_s = \frac{s}{1 + s + (2\delta/\gamma)^2} \frac{\gamma}{2} \quad (5.2)$$

where $\gamma = 2\pi \times \Gamma$ is the transition linewidth ($\Gamma = 6.1$ MHz) (see also Equation 2.17). The detuning used in this image was $\delta = -2.1\gamma$ which yields a scattering rate of $\gamma_s = 4.8564 \times 10^6$ photons per atom per second, however this naive statement does not account for a energy level shift due to the magnetic field of the chip. We estimate this shift, γ_B to be at most $+1.56\gamma$. As the image had an exposure time of 10.5 ms, the calculation becomes

$$\text{atom number} = \frac{\text{total photons}}{\gamma_s \cdot \text{exposure}} \quad (5.3)$$

which yields roughly 12,000 atoms without the magnetic field correction and 4,000 atoms with it. We settled on 6,000 atoms for reporting purposes as it is within a factor of two of both results. A more exhaustive error analysis showed that the shift due to the magnetic field was infact the biggest contributor to the error budget.

5.3.2 Performance Comparison

It is helpful to see how the apparatus stacks up against our atom chip competitors across the world. As there are on the order of a dozen labs with atom chip experiments, I have compiled five examples that outline the flexibility and performance through such parameters as BEC size and repetition rate, atom chip lifetime and species options. One can see that some systems can be faster, or produce a larger BEC though no one system has a monopoly on performance.

PI	Aubin	Thywissen	Schmiedmayer	Anderson	ColdQuanta
Affiliation	W&M	U. of Toronto	Vienna U.	JILA	Commercial
BEC	^{87}Rb	^{87}Rb	^{87}Rb	^{87}Rb	^{87}Rb
DFG	-	^{40}K	-	-	-
Size (10^4)	2 – 4	4.5 – 200	5		3.4
Rep. Rate	20-40 s	5-15 s		3 s	1 s
Lifetime	12 s	5 s		3 s	5 s
Chambers	Dual	Single	Single	Dual	Single
Notes	^{39}K	[66]	Dual Layer Chip	[67]	Cs/K [68]

TABLE 5.2: An at a glance comparison of our apparatus to a handful of competitors throughout the world [66, 69, 67, 68]. This list is not exhaustive, and plenty of other quality systems exist including those run by A. Aspect, T. Hänsch, P. Treutlien, J. Reichel, E. Hinds, C. Zimmermann, and J. Fortágh. Note: the W&M apparatus numbers have been updated to include the latest performance available at the time of submission of this dissertation.

CHAPTER 6

Magnetic Trapping System

In this chapter, I discuss in detail the magnetic trapping system used to run the MOT coils (affectionately known as the BEC Apparatus Magnetic Field Switch, or BAMF Switch). The high power magnetic switch was designed to control the current through the MOT coils for both magneto-optical trapping and magnetic trapping operations. It is capable of stopping the current in the coils in less than $100\mu s$ and is capable of fast turn-on in less than $250\mu s$. The operation is crucial to the proper function of the apparatus and the design was based on previous work by A. Stummer [70] with modifications to suit our specific needs. I thankfully give credit to A. Garcia for designing and winding the four main MOT coils. From these coils, I was able to create a set of MOT coils where each coil consisted of two ribbon wire coil pairs for the MOT current and two flattened 1/4" copper piping coils for water cooling. A mounting system was designed out of TIVAR and commercial off-the-shelf hardware.

6.1 Motivation

Laser cooling via optical molasses requires that the atoms see no magnetic field. Atom trapped in a MOT experience a magnetic field of ≈ 6 G/cm generated by 8-12 A in a set of anti-helmholtz coils. In the time between the MOT and optical molasses stages, the atoms are not trapped; as a result, the magnetic field must be turned off as fast as possible in order to limit the expansion of the cold cloud and corresponding decrease in atomic density between the MOT and molasses stages. The magnetic field must be turned off while the lasers are blocked; otherwise, the atoms will experience a spatially varying optical force. It is also useful to zero the magnetic field quickly before other processes such as imaging and optical pumping.

6.2 Coil and Mount Design

Coil	MOT	Push (P1)	MOT Bias	Push Bias	Vertical Bias
R_{Inner} (cm)	5.5	12.5	5.5	12.5	
R_{Outer} (cm)	8.3	15.2	8.3	15.2	
$(G/cm)/A$	0.86(4)	2.12(9)	0.66(7)	0.63(6)	0.66(5)
N_{turns}	26	25	6	4	
Sep. (cm)	9	8	10	9	
Wire Thick. (mm)	1.09	1.09	1/4 in	1/4 in	
Inductance	0.6 mH	-	-	-	303 μ H

TABLE 6.1: Details of the MOT cell coils. The MOT and push bias coils were constructed from 1/4 in copper pipe that was bent, isolated from itself with Kapton tape and epoxied to the MOT and push coils, respectively. These coils provide both water cooling and environmental magnetic field compensation. The Vertical bias coils were constructed by J. Field using enamel coated copper wire and epoxied into shape to fit the perimeter outline of the rectangular MOT cell.

The anti-Helmholtz MOT coil pair is comprised of two multi-layer coils, each constructed from two insulated single-layer copper ribbon wire coils and two insulated copper tubing coils, forming a wire-water-wire-water stack. The water cooling

layers were wrapped from 0.25 in. copper tubing that was pressed thinner after being formed to allow for maximum surface area contact with the ribbon wire coils. Each wrap of the water coils was manually insulated with Kapton tape as they are electrically connected in a Helmholtz configuration to provide magnetic bias field trimming along the x-axis.

The Helmholtz-esque push coils (labeled P1 in Figure 4.1) are constructed in the same manner, albeit with a single layer of each type (wire-water). The water cooling portion of the push coils are again used to provide magnetic field trimming along the z-axis. A small rectangular coil pair (purple in Figure 4.1 is used for vertical field adjustments along the y-axis). This coil was designed to provide a uniform field at the center while remaining out of the diagonal MOT beam paths.

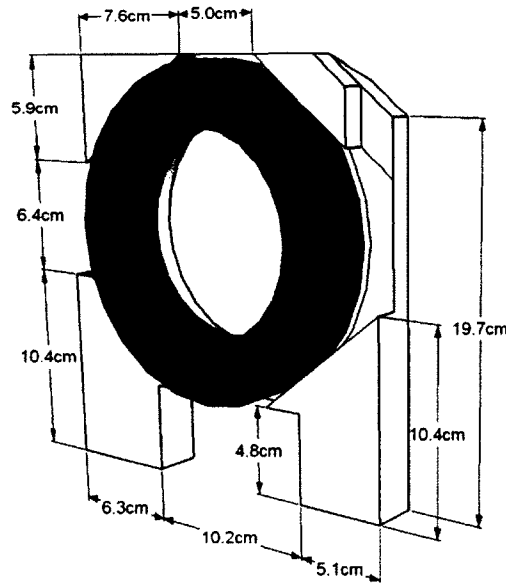


FIG. 6.1: TIVAR Mount for MOT Coils. To avoid undue eddy currents in the vicinity of the MOT cell, a non-metallic, yet thermally conductive mount for the MOT coils was machined out of 1" TIVAR.

The MOT coils are easily the most used high current component of the apparatus, and require special consideration for power dissipation during operation. The

fast turn off and on operation can easily lead to unwanted eddy currents which must be avoided by eliminating electrical conductors in the coil mount design. The MOT coils are held using custom mounts made of 1" TIVAR, a strong and thermally conductive plastic. The shape of the design has been carefully constructed and modified in place to allow for the proper installation and positioning of the MOT, push and vertical bias coils, all from the same structure, as shown in Figure 6.1. The MOT coils are snug inside the TIVAR mount and are secured with several zipties. The push coils are held in place by a set of TIVAR blocks that bolt to the main MOT coil mount, fixing the Push coils into place. A pair of cross bars is attached to the end closest to the dispensers to fix the distance between MOT coils as well as support one end of the rectangular vertical bias coils. The opposite end of the vertical bias coils is held by a post to the optics table. A machined bar of blue TIVAR is placed at the corner opposite of the post held end, held in place by the compression from the MOT mount.

The MOT and push coils feature coiled copper tubing layers for thermal cooling as well as bias field trimming. These coils are connected in series via Swage-Lock and 1/4 in flexible PVC tubing and are supplied with 8 psi differential pressure (according to W&M facilities management) held at 16 °C from the building's chilled water send and return connections. The apparatus is always operated with the water cooling.

6.3 Magnetic Switch Driver

A lab-built high current switch controls the MOT coil current for both the MOT and magnetic trap. Despite the 0.6 mH inductance of the MOT coils, the switch allows a rapid turn-off from 100 A in less than 100 μ s (time t_{off} in Figure 6.2). The rapid turn-off is essential for maintaining the density of the atomic cloud

prior to the optical molasses technique and enabling reliable absorption imaging of the MOT and magnetic trap. A second function provides fast turn-off of the MOT coils to minimize heating of the atoms during loading of the magnetic trap. The switch circuit (shown in Figure 6.3) is based on that of [70], but it has been adapted to accommodate two power supplies. Our high current supply (Agilent, 6571A-J03, labeled PS-1 in Figure 4.1 and 6.3) cannot respond to programming changes faster than ~ 50 ms, constraining the rate of magnetic field changes during the MOT to magnetic trap transition. We circumvent this limitation by introducing a second power supply that is a modest current source (Kepco, ATE6-25M, labeled PS-2 in Figures 4.1 and 6.3) dedicated to MOT operation only. The system switches in the high current supply to run the magnetic trap. The pre-programmed PS-1 high current supply is connected to the system through a high current MOSFET (STMicroelectronics STV270N4F3) between times t_{off} and $t_{on,1}$ of Figure 6.2; during this time the voltage of power supply PS-2 is programmed to zero to ensure that it outputs no current.

6.3.1 Design and Theory of Operation

The ability to control the current in the MOT coils quickly is as important to the apparatus as the lasers themselves. Without it, the apparatus is limited to static MOT physics only. The coil driver has been designed to safely and consistently provide the desired operation within its constraints. As such, it is important to understand its operation before it can be modified, repaired, or reconfigured for anything other than its intended use.

The coil driver uses a solid state transistor switch to make and break the connection to the coil pair. By electrically breaking the circuit, the coil is forced to dissipate its stored energy through voltage clamping diodes, and the magnetic field

is reduced to zero extremely fast. To kickstart the coils to high current, the inductance of the coils themselves are used to create an LC resonant circuit operating at high voltage. The details of these circuits are discussed in the following sections.

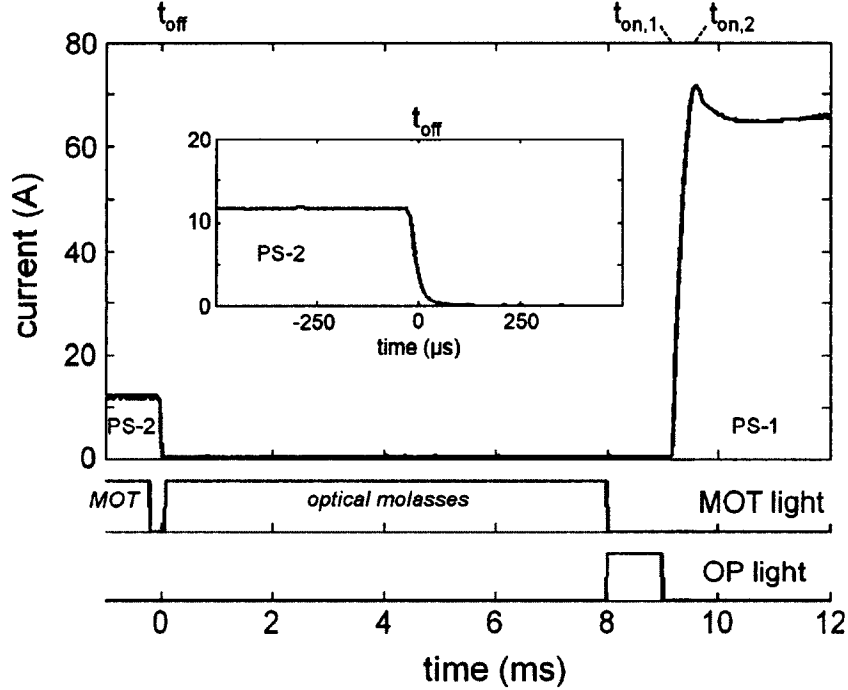


FIG. 6.2: MOT coils current switching sequence for loading the magnetic trap. *Top* Plot of MOT coil current versus time for the MOT, fast turn-off, molasses, fast turn-on, and magnetic trap stages. The current was measured using an isolated current monitor (see Figure 6.3) and a low-pass filter ($15 \mu\text{s}$ time constant). The vertical gray bands show the times during which the *fast on* and *fast off* electronics are in operation (see Figure 6.3): power supply PS-2 provides the current before the *fast off* at time t_{off} , while power supply PS-1 serves as the current source after the *fast on* operation, which starts and ends at times $t_{on,1}$ and $t_{on,2}$, respectively. The inset shows a zoomed in view of the fast turn-off. *Bottom* Timing diagrams for the Rb MOT and molasses light and the Rb optical pumping (OP) light.

Fast Off

The fast switch electronics consist of a bank of six insulated gate bipolar transistors (IGBTs) in parallel that act as a high current switch to provide the fast on and fast off operation of the MOT coils. At time t_{off} in Figure 6.2, the fast off electronics are triggered and break the circuit with the IGBTs, which causes a

high voltage inductive spike ΔV across the coils given by $\Delta V = L \cdot \frac{dI}{dt}$, with L and I the inductance and current of the coils respectively. The faster the current is turned off, the higher the voltage will spike, as described by $\frac{dI}{dt} = \frac{\Delta V}{L}$. The IGBTs (International Rectifier, IRG4PSH71UDPbF) can tolerate up to 1.2 kV when the current is blocked, so we have a stack of high power transient voltage suppression (TVS) diodes to clamp the voltage to 1 kV. By breaking the circuit with the IGBTs, the coil is forced to dissipate its stored magnetic energy through the TVS diodes, and the magnetic field is reduced to zero extremely fast. The PS-1 and PS-2 are protected by individual power diodes (1N3296A) with a reverse breakdown voltage in excess of 1.2 kV.

Fast On

After optical molasses, the magnetic field must be increased to its desired value in much less than 1 ms; however, the inductive load of the coils will resist a fast change in current. Fast on operation of the magnetic trap requires the application of a large voltage to the MOT coils to drive the initial current ramp, since $\frac{dI}{dt} = \frac{\Delta V}{L}$. We use a $C = 150\mu F$ capacitor pre-charged to 180 V by an 8.5 W DC-DC converter and held behind a silicon-controlled rectifier diode (SCR) to act as a temporary high voltage current source. Charging is done for several seconds during the MOT phase. The PS-1 high current power supply is programmed as a voltage source and connected to the circuit through the MOSFET switch during the optical molasses stage. With the IGBTs off, the MOSFET switch connects the high current power Agilent supply (PS-1) to the circuit. The SCR is triggered by a digital pulse within 100 μs of using the IGBTs to close the circuit. A full schematic of the magnetic switch system is depicted in Figure 6.4. 100 μs after the SCR trigger, the IGBT switch is closed at time $t_{on,1}$ in Figure 6.2. PS-2 is held at lower voltage behind its isolation diode and does not conduct. The capacitor and MOT coils act as a

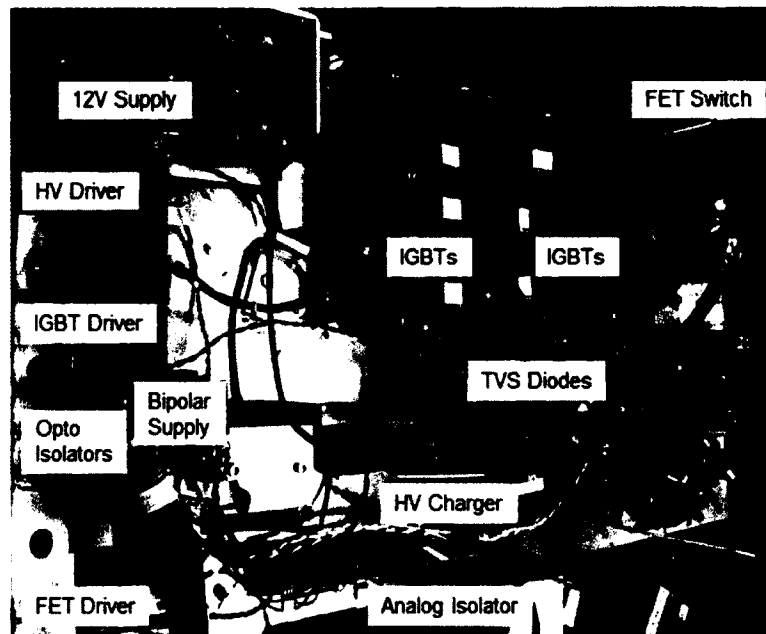
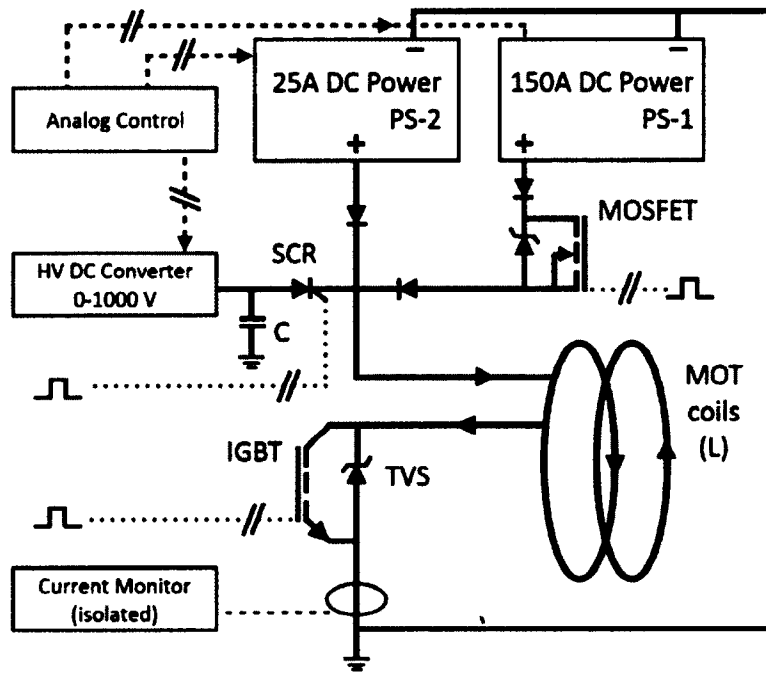


FIG. 6.3: *Top* Circuit used for the rapid *turn on* and *turn off* of the MOT magnetic coils. The circuit ground is floating with respect to the main apparatus ground. All analog and digital control and monitoring signals are isolated: Optical digital isolation is represented by $\cdots//\cdots$ symbol, whereas analog isolation is represented by the $--//--$ symbol. The IGBT symbol represents six such devices in parallel. The TVS symbol represents a stack of TVS diodes with a total clamping voltage of 1 kV. The MOSFET symbol represents two such devices in parallel. The SCR symbol represents a silicon-controlled rectifier diode. *Bottom* Photo of the magnetic switch layout as it is currently constructed.

High Power Magnetic Switch

2011, Austin Ziegler, William S. Merry, Andrew Ulmer, Ultracold Atomic Research Group
 *Based on Previous Work by A. Blumstein, University of Toronto, Quantum Optics Group

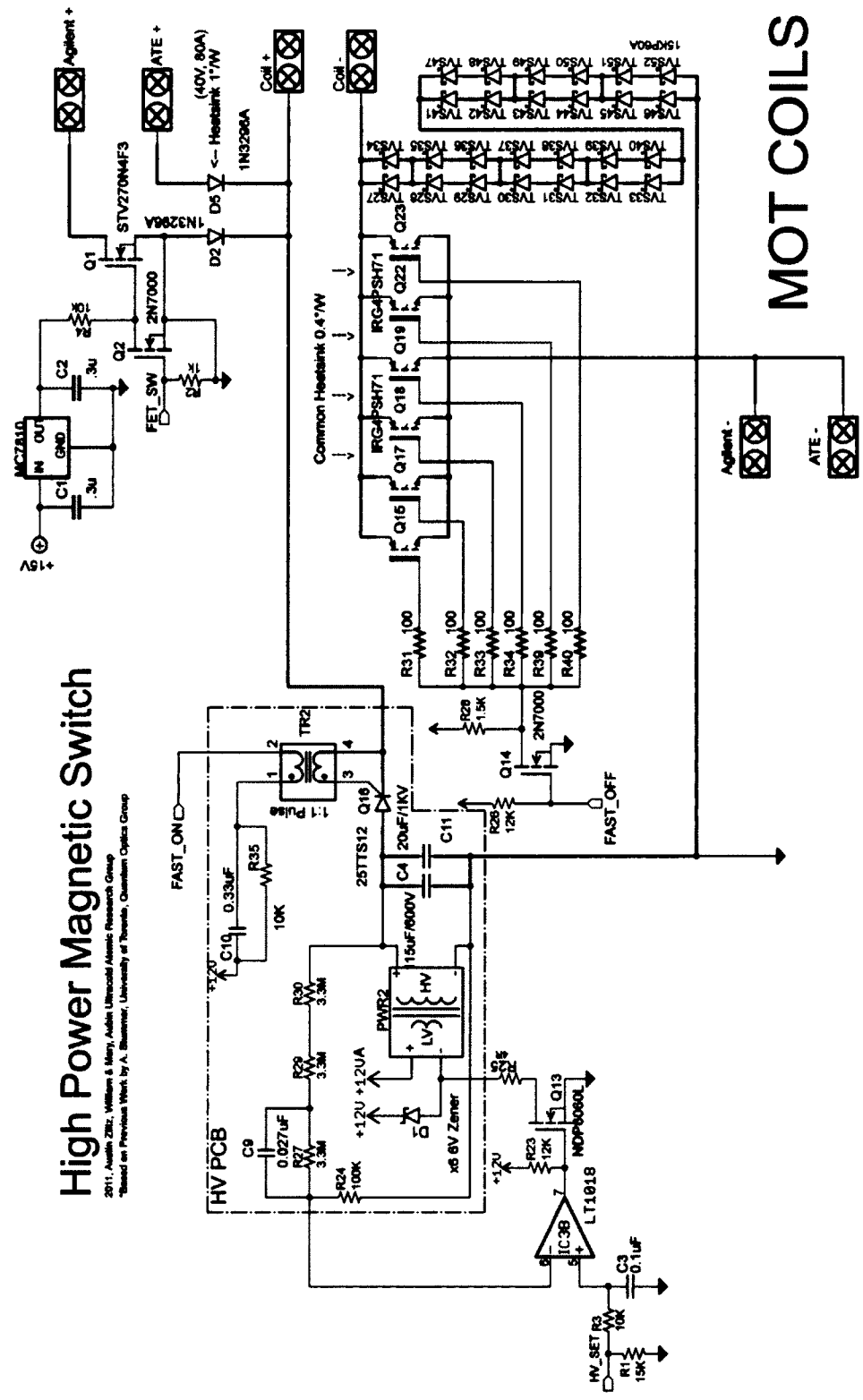


FIG. 6.4: Schematic of the magnetic switch, including the high voltage charging circuit, IGBT switches, TVS protection diodes and the MOSFET isolation switch for the second power supply.

resonant LC circuit with frequency $f = \frac{1}{2\pi\sqrt{LC}}$. After a quarter period or $t = \frac{1}{4f}$, the current peaks at 70 A, and the voltage (coil and capacitor) has dropped low enough for the PS-1 high current supply to power the coils in constant voltage mode. The SCR latches up and isolates the capacitor from the circuit, leaving the Agilent supply to maintain the current through the coils. At time $t_{on,2}$ in Figure 6.2, as the current from the HV cap drops to zero, the SCR latches up to isolate the capacitor from the coils and the PS-1 high current supply becomes the only current source. The magnetic trap is held at 70 A for 500 ms to allow any untrapped atomic states to fall away and during this time the power supply transitions to constant current operation. We then compress the trap to 80 G/cm (strong axis) at 95 A for transfer to the transport system.

6.4 Power Supply Considerations

The high current MOT coil system utilizes two power supplies to operate the different functions of the coils. The ATE6-25M (PS-2) is a unipolar supply which is dedicated to all MOT operations while the more powerful Agilent 6571A-J03 (PS-1) is used strictly for the high current magnetic trap. PS-1 cannot respond to programming changes faster than 50 ms, which puts a limitation on the timing between the MOT and magnetic trap functions. Nevertheless, it can respond to load changes much faster. The solution to this limitation is to isolate PS-1 from the coils using a MOSFET switch while programming it remotely for the magnetic trap conditions. When it is needed, the MOSFET switch connects PS-1 to the circuit and the IGBTs create a load change that it can drive efficiently and quickly.

Prior to magnetic trapping, PS-1 is isolated by the MOSFET switch, but programmed empirically to be barely in constant current mode at the desired fast on parameters. During fast on operation, the power supply is in constant voltage mode

as the current is ramping up, and the amount that the voltage drops when transitioning to constant current mode determines the damping and possible overshoot of the current. PS-2 is set such that it is just below constant voltage mode, operating in constant current. Under these conditions, PS-2 will successfully stop outputting current as PS-1 kicks in for magnetic trapping via the fast on function as the PS-2 protection diode (D5) becomes reverse biased.

One caveat to this shared power supply operation is that PS-2 will turn back on if the voltage across the coils drops below its set voltage and the forward voltage V_{diode} of its protection diode. It is good practice then to downprogram its voltage setting from the Adwin controller shortly after the Fast On operation. This is crucial for proper operation of magnetic transport as well as any magnetic trapping tests where the current is ramped down to determine what spin states are trapped.

6.5 Isolation and Remote Control

As stated previously, the MOT coil uses an Agilent 6571A-J03 (PS-1) and a Kepco ATE6-25M (PS-2), however similar power supplies are used throughout the apparatus and comments presented here can be generalized for any use with these supplies. The current and voltage settings of the power supplies are independently controlled by the Adwin sequencer. The Agilent 6571A-J03 power supplies' have a connect/disconnect button in addition to the front panel power switch. The default setting after power up is disconnected. This is a convenient way to disable the power supply without turning it completely off.

Great effort has been taken to ensure that the remote programming inputs are electrically isolated from the experimental ground and Adwin sequencer for safe, proper operation. An obvious reason for this is the prevention of ground loops, which can be a source of noise and other problems, however the specifics of program-

ming the Agilent 6571A-J03 presents an additional precaution. The programming input grounds on the 6571A-J03 are directly connected to the power supply positive output. This is not normally a problem, but if any of our coils were to contact each other or the optics table, it could potentially send high current back through the Adwin computer. This unfortunate event has happened to the Thywissen group at University of Toronto [71] and so we have taken extra precautions to prevent the chance for such a catastrophic failure in our lab. There is a dedicated bank of analog isolation buffers designed and constructed by Seth Aubin in the main rack beneath the Adwin sequencer used to decouple the Agilent (PS-1) and ATE (PS-2) voltage and current control signals from the sequencer.

All digital inputs to the coil driver are also isolated via optical isolators, and the HV Set input has an analog isolation circuit on board as depicted in Figure 6.5. This isolation buffer is identical to the bank built into the rack system. BNC cables are routed directly to the power supplies and magnetic switch, bypassing all cable patch panels to avoid accident connection mistakes. This applies to all analog voltage and current control signals for both Agilent and ATE power supplies running the MOT coils.

6.6 Calibration and Usage Notes

This system contains high voltages and high currents and should not be modified or troubleshot while in operation. The HV capacitor used for the fast on operation can be safely discharged using the low resistance static foam that integrated chips are often stored in. It is recommended that the HV set voltage be set low unless cycling the system to prevent the circuitry from constantly charging the capacitor.

If the system is not behaving as expected, it is best to test each component circuit individually, starting with the front panel control of the power supplies. Use

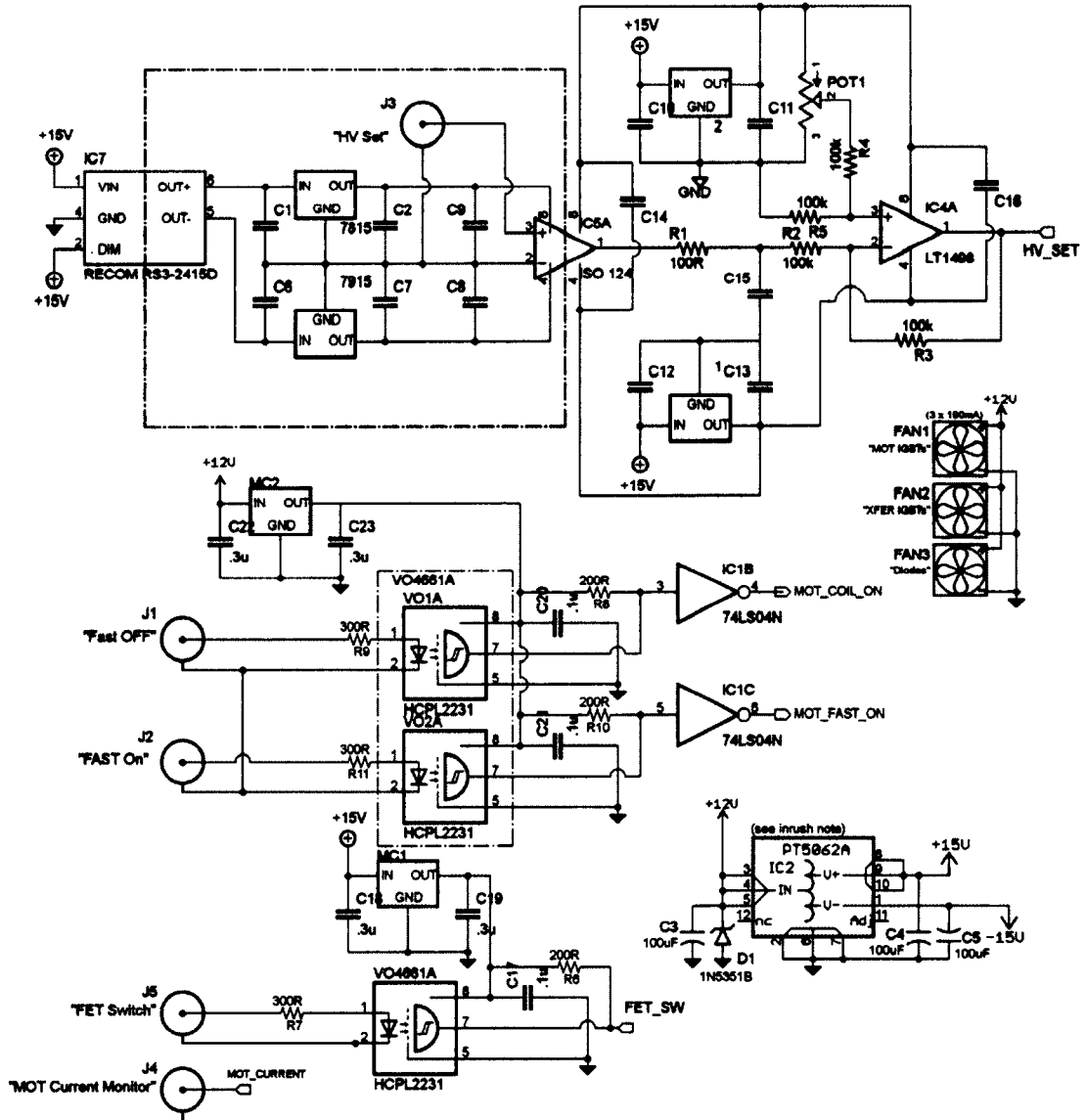


FIG. 6.5: Schematic of the magnetic switch isolation circuitry including optical isolation on the digital inputs and galvanic isolation on the high voltage set point input. Also shown are the fans, and the isolated power supply for the current monitor.

the current sensor to monitor the coils. Verify that the IGBTs and FET switch are responding to the Adwin correctly before testing any Fast On or Off operations. ALWAYS test at low power, current and voltage. During normal operation, 180 V and 1 kV are present on certain circuit components, including the MOT coils.

There have been two recorded failures of the IGBTs: one due to incorrect wiring to the coils during the initial construction and testing of the system and the second resulting from a failure of the HV circuit. In the first case, the IGBTs were connected between the power supply and the coils, instead of between the coils and ground: the IGBTs failed and cracked open as a result. In the second case, the IGBTs simply became permanently open circuit without any visible damage, a condition that was much more difficult to diagnose. This prompted a more robust rewiring of the magnetic switch system.

One of the first quantum signals to be achieved with the apparatus was the signature stair step created by lowering the magnetic trapping gradient to a point where $m_f = 1$ falls away under gravity while $m_f = 2$ remains trapped. First performed in rubidium, this technique is very useful to verify the success optical pumping as it conveys the relative population size of the two trappable m_f ground state sublevels. This was also performed on ^{39}K as shown in Figure 6.6.

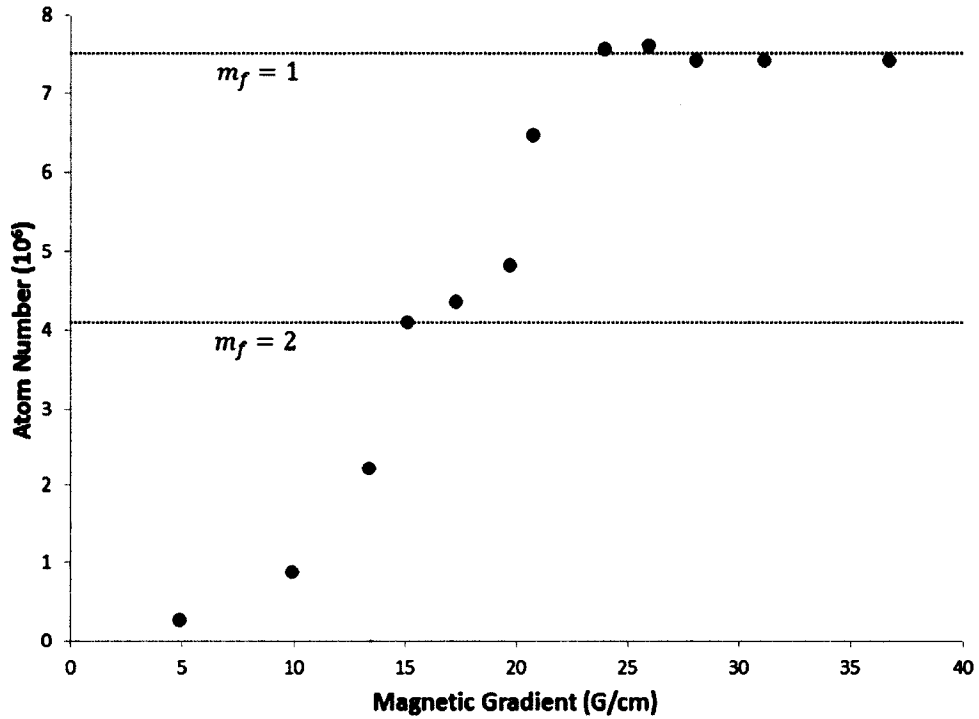


FIG. 6.6: Potassium magnetic trap atom number as a function of magnetic field gradient in the MOT coils. Un-optically pumped potassium is loaded into the magnetic trap from the MOT to create a mixed population of states. The magnetic field is turned on fast to 70 A to capture all Zeeman m_f sublevels. The gradient is subsequently lowered until the $m_f = 1$ level falls away due to gravity (< 25 G/cm). Eventually, the $m_f = 2$ also falls away. A similar signal was captured for ^{87}Rb , albeit it at twice the magnetic gradient due to the doubled mass of rubidium compared to that of potassium. This was the first quantum signal achieved in the lab.

CHAPTER 7

Magnetic Transport System

As the vacuum system was designed with two chambers, a method of delivering MOT-cooled atom clouds to the atom chip is required. Our apparatus requires a system to transport cold atoms over a distance of 60 cm with minimal heating. The length traversed is complicated by a right angle. Our research interests necessitate the ability to simultaneously transport multiple species as quickly as possible to maintain manageable experimental repetition rates. The system must also provide for ample optical access both at the chip and in the MOT cell.

There are several methods for transferring an atomic cloud from one area to another. The most basic method would be to simply drop the cloud and let it fall under gravity to a secondary location (A. Steinberg, University of Toronto). An extension of this would use an optical force to push the atoms horizontally (Trinat at TRIUMF, [13]). Although straight-forward, these methods require the atoms to then be re-trapped in a MOT at the secondary location as they have been experiencing ballistic expansion over the transport distance. Another technique includes optical tweezers [72], where optical dipole forces are used to control the motion of atoms from one location to another. Unfortunately, turning a corner using optical tweezers is

experimentally challenging and impractical.

Mechanical translation designs exist [73, 74], but they are not without their drawbacks. Simply translating a pair of anti-Helmholtz coils along a track around the vacuum system can effectively transport atoms without added heating. It could also effectively navigate a corner; however, the presence of a moving coil at both ends would severely hinder optical access. It would be near-impossible to install permanent optics closer to the vacuum system than the moving coils. Mechanical failures can be catastrophic [75] and pose a serious safety hazard.

Our non-mechanical system was designed based upon the previous work of [76, 77] but adjusted to our geometry. The system features seven identical anti-Helmholtz coil pairs in addition to two perpendicular push coils, all driven by only three high current Agilent power supplies (6571A-J03). The use of three coil pairs simultaneously allows three degrees of freedom to be controlled independently. In principle, the three variables are the trap center position, the vertical magnetic gradient and the trap aspect ratio. Depending on the coil geometry, there is a lowest aspect ratio value that allows all coils to be operated using unipolar current sources. This is determined analytically and chosen as the preferred aspect ratio.

This chapter first identifies the magnetic transport constraints and the preferred transport velocity and path, then explains the recipe for simulating the transportation. Next, the hardware and coil structures are detailed along with installation and testing information before reporting the performance and results of the system. Again, credit is due to the excellent work of A. Garcia, who designed and constructed the transport coils; S. Aubin, who constructed the current multiplexer used for the transport system; and Megan Ivory, who designed, constructed and installed the Chip push coil (P2 in Figure 4.1).

7.1 Magnetic Transport Constraints

The method for determining a sequence of current ramps that will translate neutral atoms across a series of quadrupole traps is as follows:

1. A set of time-dependent constraints for the three degrees of freedom must be established (trap position, vertical gradient, aspect ratio).
2. These constraints must be manipulated into a system of equations that can be solved for a set of operating currents at every point along the transport path,
3. The coils must be effectively modeled so that the off-axis magnetic fields can be accurately calculated,
4. A transport trajectory must be specified such that the solutions are a set of currents as functions of time and not position, and
5. Finally, the solutions must be discretized to be accurately reproduced by the Adwin sequencer, after which the sequence can be stretched or compressed in time as needed.

The current ramps (see Figure 7.1 (b)) necessary for transporting the atoms by adiabatic translation, with minimal heating are determined by maintaining three conditions:

1. The total magnetic field at the (moving) trap center must be zero,
2. the vertical gradient must remain fixed at a value strong enough to hold the atoms against gravity, and
3. the aspect ratio between the remaining two orthogonal axes must remain fixed at an optimal value significantly determined by the coil geometry.

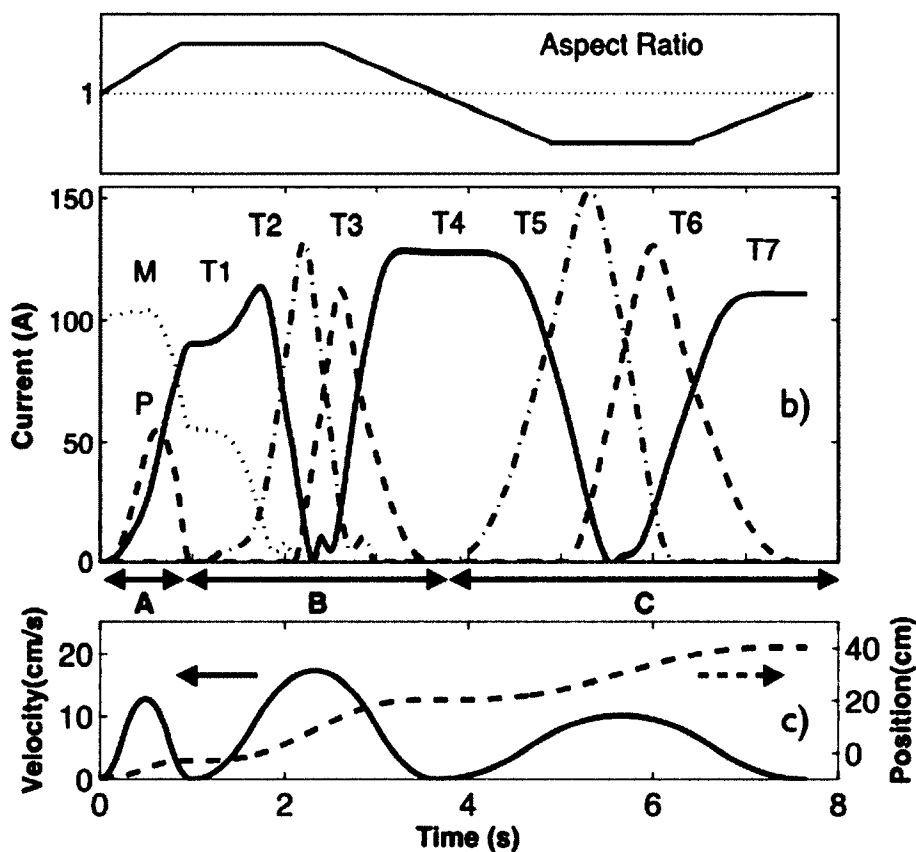


FIG. 7.1: Transport system operation. (a) Diagram of the constraint placed on the aspect ratio A_0 . (a) Diagram of the aspect ratio as it changes throughout the transport sequence. Values above one refer to an aspect ratio stretched along the horizontal transport axis. Values below 1 refer to an aspect ratio stretched along the vertical transport axis. (b) Coil current sequence. M: magnetic trap current provided by power supply PS-1. P1: Push coil current (MOT cell). T1-T7: Transport coil currents. The linestyle (dotted, dashed, solid, and dash-dot) represents which of four power supplies is used to drive the labeled coil. The loading sequence from coil T7 to the atom chip trap is not shown (involving push coil P2 and the chip magnetic fields). (Bottom) Simulated velocity and position trajectories for the current sequence. (a) Magnetic trap to transport trap handoff. (b) Transport to corner. (c) Transport from corner to atom chip.

Previously, two coils have been shown to be insufficient [78], thus the conditions can be met by using three pairs of coils simultaneously and following a predetermined position and velocity curve (see Figure 7.1 (c)) to generate the current ramping sequence displayed in Figure 7.1 (b). The overall timing is scaled experimentally to maximize speed and efficiency while minimizing heating of the atomic cloud.

The first condition is the most obvious. In order to successfully translate a quadrupole trap, a magnetic field of zero must be maintained the trap location r_0 as it moves along the translation axis

$$\vec{B}(r_0) = 0. \quad (7.1)$$

7.1.1 Vertical Gradient

The second condition required to translate a quadrupole trap is that the vertical gradient $\frac{\partial B_z}{\partial z}$ must remain large enough to support the atomic cloud against the force of gravity. This condition also sets the overall scale of the current and magnetic fields during operation. In a quadrupole field, $\vec{B} = B_z \hat{z}$ everywhere along the \hat{z} axis. However, it is simply not enough to keep $\frac{\partial B_z}{\partial z}$ greater than some minimum value as any variation will modulate the size of the atomic cloud itself and cause heating, as adiabatic compression and decompression are not possible in a linear potential. As such, $\frac{\partial B_z}{\partial z}$ should remain constant (G_0) throughout the entire transfer.

$$\left. \frac{\partial B_z}{\partial z} \right|_{r_0} = G_0 = \text{constant} \quad (7.2)$$

7.1.2 Aspect Ratio

A constant aspect ratio is important to avoid modulation of the trap shape and the subsequent heating of the atoms it could cause. Ideal transport would then fulfill

the following conditions for an arbitrary transport position \vec{r}_0 along the common coil axis. Depending on the coil geometry, there is a maximum aspect ratio that allows all coils to be operated using unipolar current sources. This is determined through simulations to be $A_0 = 1/1.44$ and chosen as the optimal aspect ratio.

$$\begin{aligned}
\frac{\partial B_x}{\partial x} &= G_x \\
\frac{\partial B_y}{\partial y} &= G_y \\
\frac{G_x}{G_y} &= \left(\frac{\partial B_x}{\partial x} / \frac{\partial B_y}{\partial y} \right) \Big|_{r_0} = A_0 \\
&\Rightarrow \left(\frac{\partial B_x}{\partial x} - \frac{\partial B_y}{\partial y} A_0 \right) \Big|_{r_0} = 0
\end{aligned} \tag{7.3}$$

Where $A_0 \neq 1$ is expected as the cylindrical symmetry of the quadrupole field is broken by the use of adjacent anti-Helmholtz coils. The magnetic fields are determined by the currents in the anti-Helmholtz coils to satisfy equations 7.1, 7.2, 7.3. Three degrees of freedom demand that three currents are required.

7.2 Transport Velocity

Now it is possible to solve equations 7.1, 7.2, 7.3 for all points along the transport axis, resulting in three equations for current I as a function of position, r . However, we do not process control signals in position but rather in time. This necessitates a predetermined position function for the atom cloud, $r(t)$ providing its position as a function of time. With this path, we now have solutions for the three currents as a function of time t .

In practice, an acceleration and deceleration scheme is chosen and used to generate the velocity and position functions shown in Figure 7.1 (c). After the system

currents are solved along the transport path as a function of time, the sequence is approximated with linear segments in the Adwin sequencer and empirically scaled in time to determine an optimal transport speed that avoids heating as well as losses due to vacuum lifetime.

Following the work of Battelier [76] and Winkler [77], an acceleration path is chosen that consists of linear segments creating a triangular wave of sorts. This results in the smooth velocity and position paths shown in Figure 7.1. Although the transport system has two distinct arms for horizontal and vertical motion, the handoff from the MOT to the transport system is quite irregular and requires special consideration. Normally, the geometry of our system would require a very sharp change in the currents. In order to minimize any complications due to this, the velocity of the atoms slows almost a halt through this section, essentially splitting the horizontal leg into two independent sections. Although this compromise lengthens the overall transport sequence, it reduces the constraints on the power supplies to avoid a sharp change in current.

In order to satisfy all three conditions, three coils and thus three currents are required. Expanding equation 7.1 to encompass the field from three separate coils yields the expression,

$$I_n \tilde{B}_n \Big|_{r_0} + I_{n+1} \tilde{B}_{n+1} \Big|_{r_0} + I_{n+2} \tilde{B}_{n+2} \Big|_{r_0} = 0 \quad (7.4)$$

where \tilde{B}_n is the Gauss/Amp of transport coil n at the point r_0 and all I_n are positive. For horizontal transport, coils 1 – 4 are used as well as the MOT coil and MOT push coil (P1). Vertical transport uses coils 4 – 7 plus the chip push coil (P2). Next the vertical gradient constraint can be written as

$$I_n \frac{\partial \tilde{B}_{z,n}}{\partial z} \Big|_{r_0} + I_{n+1} \frac{\partial \tilde{B}_{z,n+1}}{\partial z} \Big|_{r_0} + I_{n+2} \frac{\partial \tilde{B}_{z,n+2}}{\partial z} \Big|_{r_0} = \frac{\partial B_{z,target}}{\partial z} = G_0 \quad (7.5)$$

Furthermore, Maxwell's equations state the divergence of the magnetic field is zero:

$$\begin{aligned}\nabla \cdot \vec{B} &= 0 \\ \frac{\partial B_x}{\partial x} + \frac{\partial B_y}{\partial y} + \frac{\partial B_z}{\partial z} &= 0 \\ \frac{\partial B_x}{\partial x} + \frac{\partial B_y}{\partial y} &= -\frac{\partial B_z}{\partial z}\end{aligned}\tag{7.6}$$

Substituting equation 7.6 into the expression of 7.5 yields,

$$\begin{aligned}I_n \left(\frac{\partial \tilde{B}_{x,n}}{\partial x} + \frac{\partial \tilde{B}_{y,n}}{\partial y} \right) \Big|_{r_0} + I_{n+1} \left(\frac{\partial \tilde{B}_{x,n+1}}{\partial x} + \frac{\partial \tilde{B}_{y,n+1}}{\partial y} \right) \Big|_{r_0} \\ + I_{n+2} \left(\frac{\partial \tilde{B}_{x,n+2}}{\partial x} + \frac{\partial \tilde{B}_{y,n+2}}{\partial y} \right) \Big|_{r_0} = -\frac{\partial B_{z,target}}{\partial z} = -G_0\end{aligned}\tag{7.7}$$

Lastly, expanding equation 7.3 to include three coils yields the final equation to be solved.

$$\begin{aligned}I_n \left(\frac{\partial B_{x,n}}{\partial x} - \frac{\partial B_{y,n}}{\partial y} A_0 \right) \Big|_{r_0} + I_{n+1} \left(\frac{\partial B_{x,n+1}}{\partial x} - \frac{\partial B_{y,n+1}}{\partial y} A_0 \right) \Big|_{r_0} \\ + I_{n+2} \left(\frac{\partial B_{x,n+2}}{\partial x} - \frac{\partial B_{y,n+2}}{\partial y} A_0 \right) \Big|_{r_0} = -\frac{\partial B_{z,target}}{\partial z} = -G_0\end{aligned}\tag{7.8}$$

All together, expression 7.4, 7.7 and 7.8 form the system of equations that represent our chosen transfer constraints. Given r_0 , A_0 , and G_0 , we can solve for I_n , I_{n+1} , and I_{n+2} .

7.3 MOT to Transport Handoff

An interesting situation arises at the beginning of the transport process where the MOT coil-based magnetic trap must interface with the transport system while adiabatically stretching the aspect ratio from $A = 1$ to A_0 . The aspect ratio is

constrained to follow a fixed linear path from an initial value of 1 at the center of the MOT cell to the ideal value of A_0 at the center of the first transport coil T1. The constraint follows the form,

$$A(r) = 1 + (A_0 - 1) \frac{r + y_0}{y_0} \quad (7.9)$$

where r is the position of the translating trap, and $r = -y_0$ is the location of the center of the MOT coils where $A(-y_0) = 1$. In this frame, the first transport coil (T1) is centered at $r_0 = 0$ where $A(0) = A_0$. A similar constraint can be placed on the target z-axis gradient, as our MOT coil power supply is voltage-limited to a maximum output of 14 V and 100 A and a corresponding gradient of 86 G/cm. The transport system can operate at higher gradients and so that $\frac{\partial B_{z,target}}{\partial z}$ is constrained to follow

$$\frac{\partial B_z}{\partial z} = \frac{\partial B_{z,initial}}{\partial z} + \left(\frac{\partial B_{z,target}}{\partial z} - \frac{\partial B_{z,initial}}{\partial z} \right) \frac{r_0 + y_0}{y_0} \quad (7.10)$$

As the MOT Push coil P1 is a helmholtz coil centered on the transport axis, its contribution to the translating quadrupole potential is somewhat different from the overlapping anti-helmholtz coils. As the trap center reaches the handoff where the current in P1 drops to zero and T2 takes over, the current solution is quite stringent resulting in a sharp feature in the required currents and can be difficult to reproduce experimentally. The cause of this feature has more to do with the geometry and design of the Push coil P1 than anything else, but the simplest solution is just to slow down the translation of the trap as it passes through the handoff. Unfortunately, we found that slowing down the transport through this area was detrimental to its operation. After much head banging, it turns out that the MOT coils were installed about 1 cm too far away from the transport system. As a result, the current solution was invalid for the handoff region as installed. Simulations showed that the MOT

coil location was problematic and so the decision was made to move the MOT coils and optics to satisfy the originally intended separation between the MOT coils and transport system. The system worked like a charm after this.

7.4 Simulation

While the on-axis magnetic field of a Helmholtz or anti-Helmholtz coil pair is a simple calculation, moving off of the strong axis is another method altogether. It is possible to calculate the field using the exact equations for the field from a single-turn infinitely thin wire coil of radius R , perpendicular to the z axis and centered at $z = A$, $B_\phi = 0$. Following the work of [40], the transverse and axial field components in cylindrical coordinates (ρ, z, ϕ) are,

$$\begin{aligned} B_z &= \frac{\mu I}{2\pi} \frac{1}{[(R + \rho)^2 + (z - A)^2]^{1/2}} \left(\frac{R^2 - \rho^2 - (z - A)^2}{(R - \rho)^2 + (z - A)^2} E(k^2) + K(k^2) \right) \\ B_\rho &= \frac{\mu I}{2\pi\rho} \frac{z - A}{[(R + \rho)^2 + (z - A)^2]^{1/2}} \left(\frac{R^2 + \rho^2 + (z - A)^2}{(R - \rho)^2 + (z - A)^2} E(k^2) - K(k^2) \right) \end{aligned} \quad (7.11)$$

where the argument of the elliptic integrals $E(k^2)$ and $K(k^2)$ is defined as,

$$k^2 = \frac{4R\rho}{(R + \rho)^2 + (z - A)^2}. \quad (7.12)$$

Although the expressions of 7.11 describe the field of a single wire loop exactly, the geometry of the transport system requires solutions in cartesian coordinates so that the field from multiple coil pairs can be superimposed. Therefore the following

coordinate transformation is used,

$$\begin{aligned}\rho &= (x^2 + y^2)^{1/2} \\ \tan(\phi) &= \frac{y}{x}\end{aligned}\tag{7.13}$$

The magnetic field components can then be extracted in cartesian coordinates using the following,

$$\vec{B}_{x,y,z} = (B_x, B_y, B_z) = (B_\rho \cos(\theta), B_\rho \sin(\theta), B_z)\tag{7.14}$$

Forming a realistic coil pair requires more than a single turn in each coil, so a summation is used to approximate the spiral coil with an equal number of concentric rings of varying radii, taking the difference between two opposing coils to form the anti-Helmholtz pair,

$$\vec{B}_n = \sum_{i=1}^{N_T} \left(\vec{B}_{upper} - \vec{B}_{lower} \right)\tag{7.15}$$

where N_T is the number of turns in coil pair, the separation between the coils is $2A$ as \vec{B}_{upper} is located at $z = A$ and \vec{B}_{lower} is at $z = -A$.

In the simulations of the transport system, all magnetic field components are analytically described above while the gradients (partial derivatives) are computed numerically using,

$$\frac{\partial B_x}{\partial x} = \frac{B_x(x) - B_x(x + \delta x)}{\delta x}\tag{7.16}$$

where delta is a step size typically chosen to be 1-2mm. This same approximation is used for the y and z gradients as well.

7.5 Design and Theory of Operation

7.5.1 Current Multiplexer

Since the transport system requires only three or fewer coils to be supplied with current simultaneously, three high current power supplies are used (Agilent, 6571A-J03) that are multiplexed to the seven transport coil pairs (T1-T7) and the two push coils (P1 and P2). As shown in Figure 7.2, a power supply is connected to three transport system coil pairs that can be selected or deselected through use of a MOSFET-based high current switch (two STV270N4F3 MOSFETs in parallel). A 2-bit selector guarantees that only a single switch of the three can be on at any one time. During the transport sequence ramping, shown in Figure 7.1 (b), the multiplexer switches from one coil to another when the current is brought to zero. A bank of six bi-directional TVS diodes protect each MOSFET switch and its power supply against the inductive voltage spike produced if a coil is switched before current has reached zero. Moreover, these protection diodes also ensure a sub-millisecond turn-off time for each fully powered coil pair, if requested. All digital control lines feature optical isolation to limit the possibility of ground loops. Furthermore, due to the high currents involved, the transport system is fully isolated from the apparatus ground: The analog control lines for the high current power supplies are attached to the main sequencer through galvanic isolation buffers (Texas Instruments, ISO124); the MOSFET switches are powered by floating DC-DC voltage regulators; and the coils are electrically isolated from their heatsink frame.

7.6 Transport Coils Design and Mount

Each of the transport coil pairs consists of two 26-turn coils of copper ribbon wire. These coils are mounted into a water-cooled copper and thermoplastic heatsink

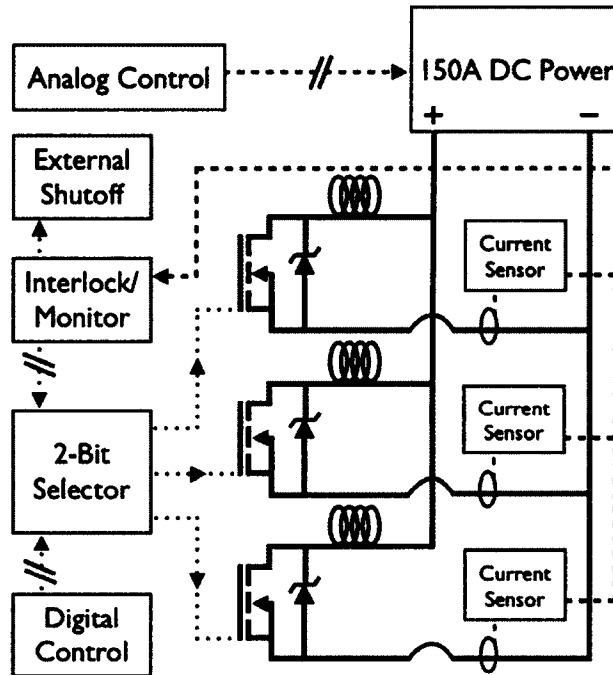


FIG. 7.2: Multiplexer block diagram for the transport system. The circuit directs up to 150 A of current from a high current power supply to one of three transport coils based on a two-bit digital control signal. A fourth back-up output is not shown. Three such circuits allow three power supplies to direct current to the seven transport coils and two push coils. The MOSFET symbol represents two such devices in parallel. The TVS symbol represents six such devices in parallel with a bidirectional 15 V clamping voltage. Optical digital isolation is represented by the $\cdot\cdot//\cdot\cdot$ symbol, and analog galvanic isolation is represented by the $- - // - -$ symbol.

Coil	T1	T2	T3	T4	T5	T6	T7
R_{Inner} (cm)	3.75	3.75	3.75	3.75	3.75	3.75	3.75
R_{Outer} (cm)	6.75	6.75	6.75	6.75	6.75	6.75	6.75
$(G/cm)/A$	0.92(5)	0.80(6)	0.98(5)	0.87(4)	0.72(8)	0.83(4)	1.01(3)
N_{turns}	26	26	26	26	26	26	26
Sep. (cm)	3.875	4.425	3.875	4.425	4.975	4.425	3.875
Thick. (mm)	1.153	1.153	1.153	1.153	1.153	1.153	1.153

TABLE 7.1: A summary of coil parameters used in the transport system. Each pair is identical, differing only by the separation, which in turn affects the gradient. Each pair is wired in series internally. Great care has been taken to guarantee and preserve the isolate between coils and the heatsink mount for safety and proper operation.

frame to dissipate up to 1.5 kW of peak power consumed by the coil pairs. The coils were first encased in a thin layer of hard epoxy (Epoxies Etc., 50-3150) before they were secured into their frames with a semi-permanent, rubber-textured thermal epoxy (Epoxies Etc., 50-3170BK). The frames were prepared with an automotive wax compound (TurtleWax) so as to insure the coil assembly can be disassembled should it ever encounter problems. Thermoplastic is used as the frame material for the first and last coils (T1 and T7 in Figure 4.1) to minimize the risk of eddy currents in the vicinity of the MOT and the atom chip although the transport current ramps shown in Figure 7.1 (b) are too slow to produce any significant eddy currents. The heatsink frame shown in Figure 7.3 is constructed of 3 individual copper plates. The main plate holds 3/8" copper tubing for water cooling and coil T5; it is also attached to the thermoplastic ends holding coils T1 and T7. The secondary plate holds coils T2-4 and is bolted to the primary plate. Coil T6 is held in place by a smaller copper block that bolts to the main plate. A thermally conductive gap filling material (Bergquist, 3500S35), shown in Figure 7.4, was used in between all three of these plates to eliminate airgaps and improve thermal dissipation.

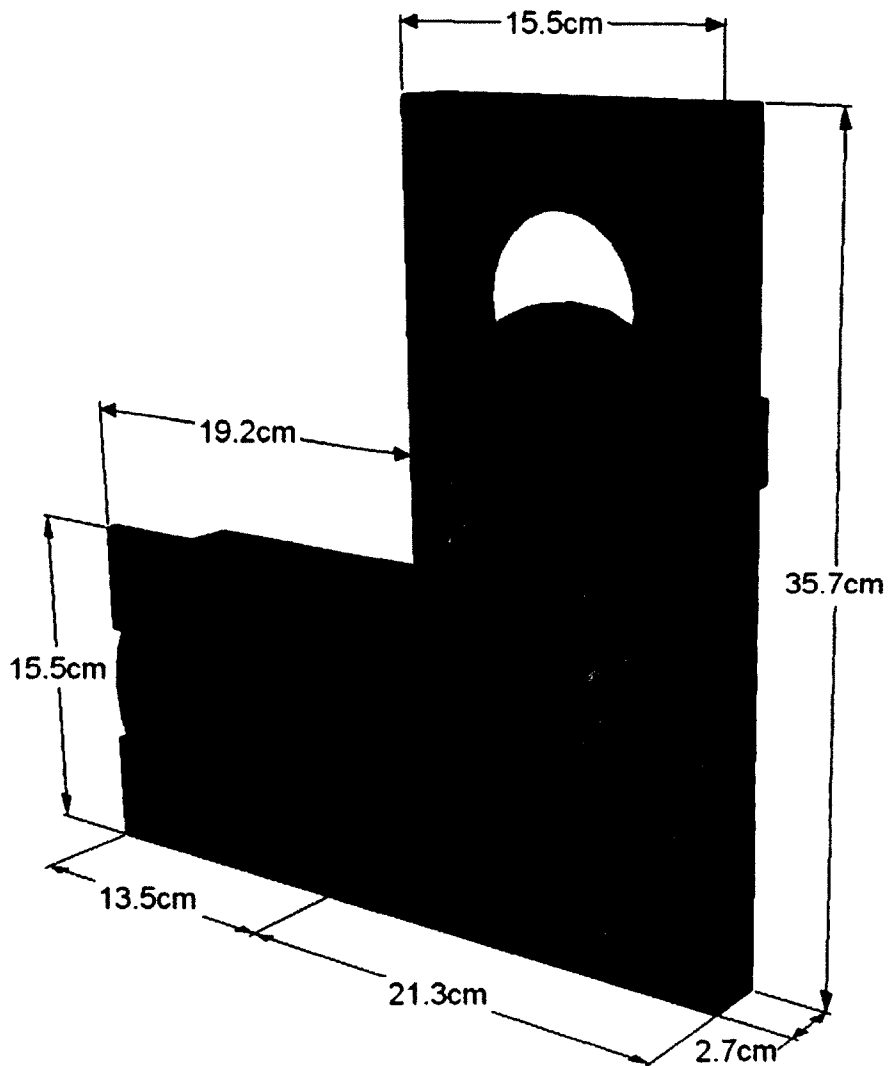


FIG. 7.3: Copper and thermoplastic transport mount. As the transport system requires serious thermal dissipation, a hybrid system of copper and thermoplastic was designed to hold each set of seven transport coils. Thermoplastic (shown in gray) was used at the ends of the transport system where excess metal would contribute to unwanted eddy currents during the *fast on*, *fast off*, and atom chip loading processes.



FIG. 7.4: Thermal compound as applied between the copper plates of the transport system.

7.7 Electrical Connections

The ribbon-shaped wire leads used in the transport coils are brought out of the frame and soldered to two 6 AWG stranded copper wire taken from standard three phase cabling. The other end of these cables were tinned and connected to industrial terminal blocks (Bussman #16204-2). From the terminal blocks connections are made to the multiplexer and the Agilent power supplies with 000/6 AWG copper wire. These measures allow for the eventual disassembly of the transport system to install a different atom chip. The terminal block set screw should occasionally be tightened up to prevent intermittent connections from cropping up over time.

7.8 Thermal Concerns

While the transport system is thoroughly heat sunk and water cooled, the coils dissipate sufficient power that thermal damage remains a significant danger. As depicted in Figure 7.2, the multiplexer circuit includes isolated current sensors for each coil pair that are monitored by a safety-interlock circuit. This safety system imposes a global total maximum current threshold of 200 A as well as local and global current-time integration thresholds. If any of these thresholds are crossed, the system will fault, turning off all the MOSFET switches. As an added precaution a trip signal is also sent to an external safety-interlock system (built by C. Fancher) that monitors the temperatures of the transport system and other apparatus coils. When this external protection system detects an over-current or over-temperature condition, it turns off all the high current power supplies via solid state relays installed on the AC power lines of these devices (built by A. Pyle).

Additional testing was performed on the coils themselves to monitor the performance of the heat sink configuration. By monitoring the voltage across the coils

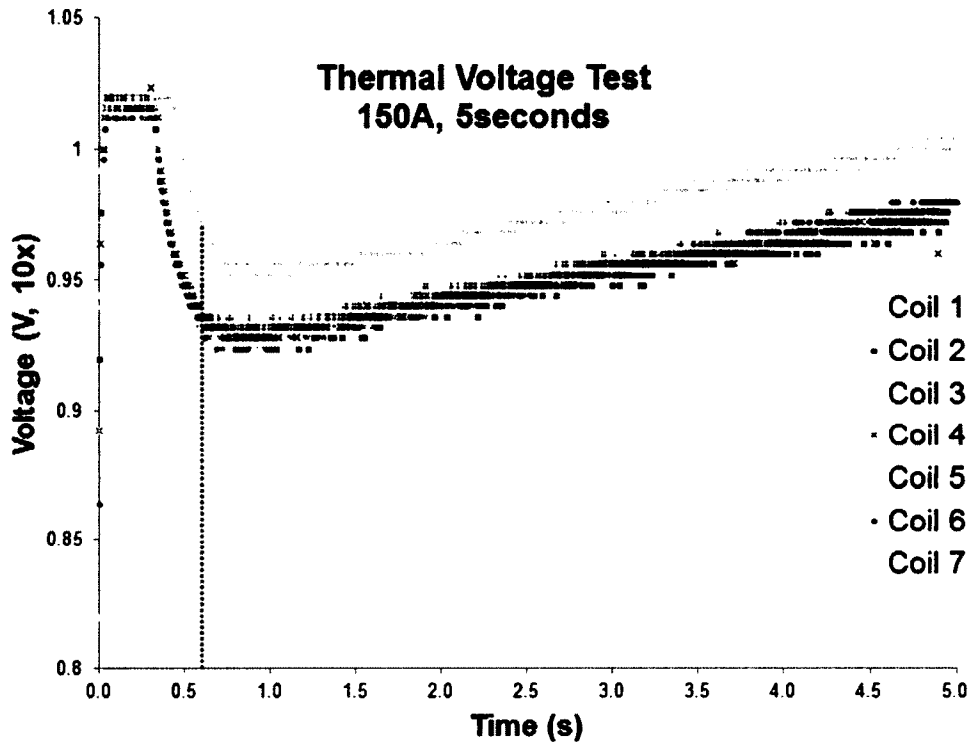


FIG. 7.5: Thermal voltage testing of the transport coils. Each coil was driven with 150 A in constant current mode for up to 5 s as voltage across the coil was monitored with a four point measurement. The change in voltage signifies a change in resistance as the coils heat up. All seven coils respond without unexpected anomalies in the thermal response. The droop in the curves at the dotted line indicate the Agilent power supply is slipping from constant voltage into constant current operation.

at high current, the thermal conductivity of the system can be qualitatively evaluated. As the coils heat up the resistance will increase, causing the voltage to rise. Presented in Figure 7.5, this diagnostic shows that all seven transport coils respond to a high current (150 A) with similar thermal behavior.

7.9 Installation

The transport system underwent an initial dry run installation separate from the vacuum system where the wiring between power supplies, the multiplexer and the transport coil assembly. Industrial terminal blocks were used to mitigate wiring connections with 000/6 AWG cables from the power supplies, 0/6 AWG cables to and from the multiplexer and 6 AWG flexible cables to the coils and other locations where flexibility is a concern. This wiring can be seen in Figure 7.6 as well as the final installation shown in Figure 7.7.

In the mockup installation, a Gaussmeter was used to calibrate and map the magnetic field of each coil along its transport axis as a function of position, in order to extract the gradient $\frac{\partial \vec{B}_z}{\partial z}$ as a function of current. Figure 7.8 shows these magnetic field measurements for T1-T4. The results of this mapping were used to adjust the current sequence to better match the real world current-to-gradient properties of the coils. A similar mapping was performed for the vertical leg (coils T5-T7). The gradient measurements are included in Table 7.1.

7.10 Performance

After calibrating the transport system using the mock installation, the system was installed on the main apparatus. The transfer sequence was first implemented in segments. Atoms were transported to the corner of the vacuum system before



FIG. 7.6: Transport system installation mockup outside of the vacuum system. The wiring and water cooling connections were finalized in this mockup as well as thermal testing.

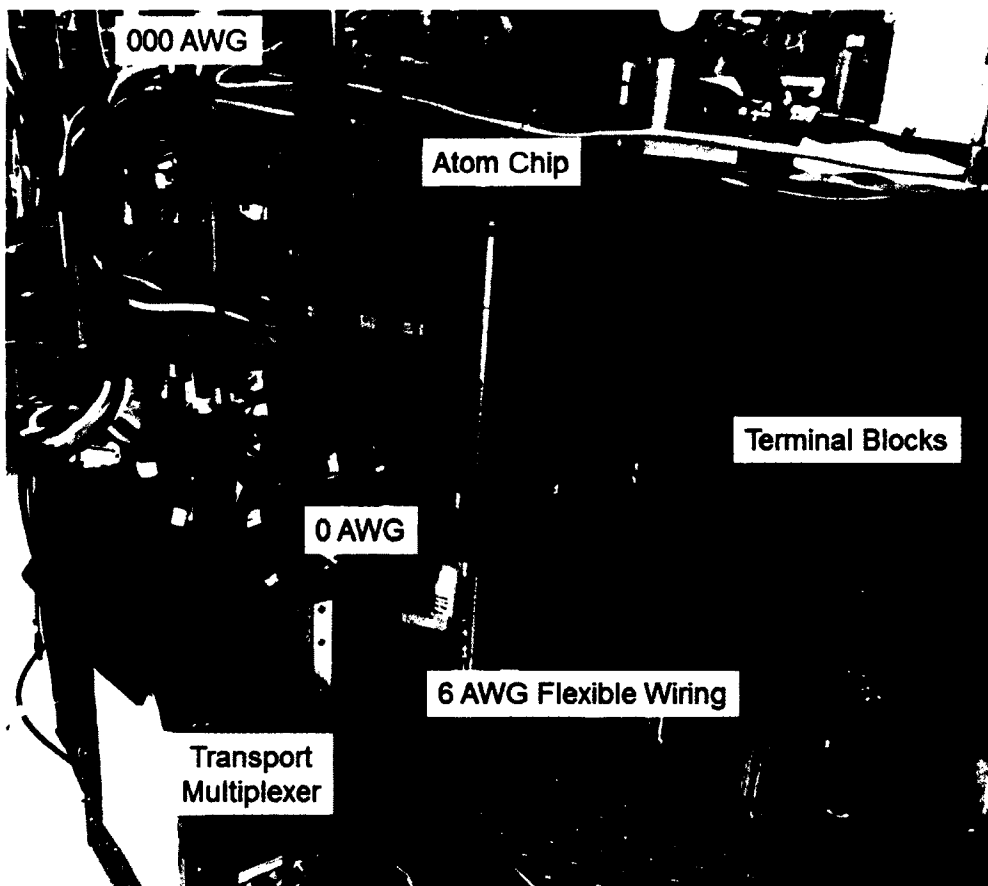


FIG. 7.7: Transport and wiring in relation to apparatus and atom chip. Flexible 6 AWG wiring (red,white,green,black) was used from the coils to terminal blocks and to mechanically decouple the cloud-mounted power supplies from the apparatus optics table. 000 AWG cable (thick, black) was used from the power supplies to the multiplexer and 0 AWG (medium, black) was used from the terminal blocks to the multiplexer.

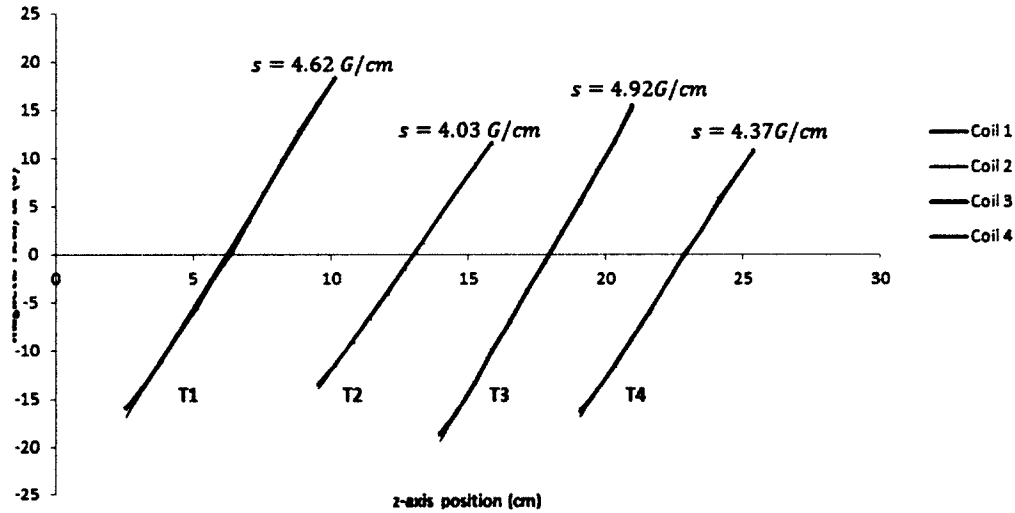


FIG. 7.8: Gradient testing of coils $T1 - T4$ of the installed transport system. The magnetic field gradients were mapped with the system in its mockup installation at a current of 5 A. Similar data was taken for Coils $T5 - T7$. The results are summarized in Table 7.1.

returning to the MOT cell: this intermediate step allows the technique to be empirically tested for heating or atom loss effects. With the first tests of this *corner and back* technique, no heating or atom losses were detected and the overall time scale was subsequently shortened by 15% as a result. The lifetime of the transported atomic cloud was found to be consistent with that of the MOT cell magnetic trap as shown in Figure 7.9 which is a testament to the design and implementation of the system.

Although the safety thresholds of the transport system prevent any measure of the lifetime while atoms are held by coil $T7$, the system was successful enough not to warrant further study of its effect on the transported atoms. Figure 7.10 is a fluorescence image of ^{87}Rb atoms trapped both by the transport system and the Z-wire of the atom chip. Once on the chip, the atoms have a lifetime of 7 – 9s as discussed in Chapter 5.

The magnetic transport system as described here provides consistent transfer of ultracold rubidium and potassium from the MOT cell to the science cell in 7 s.

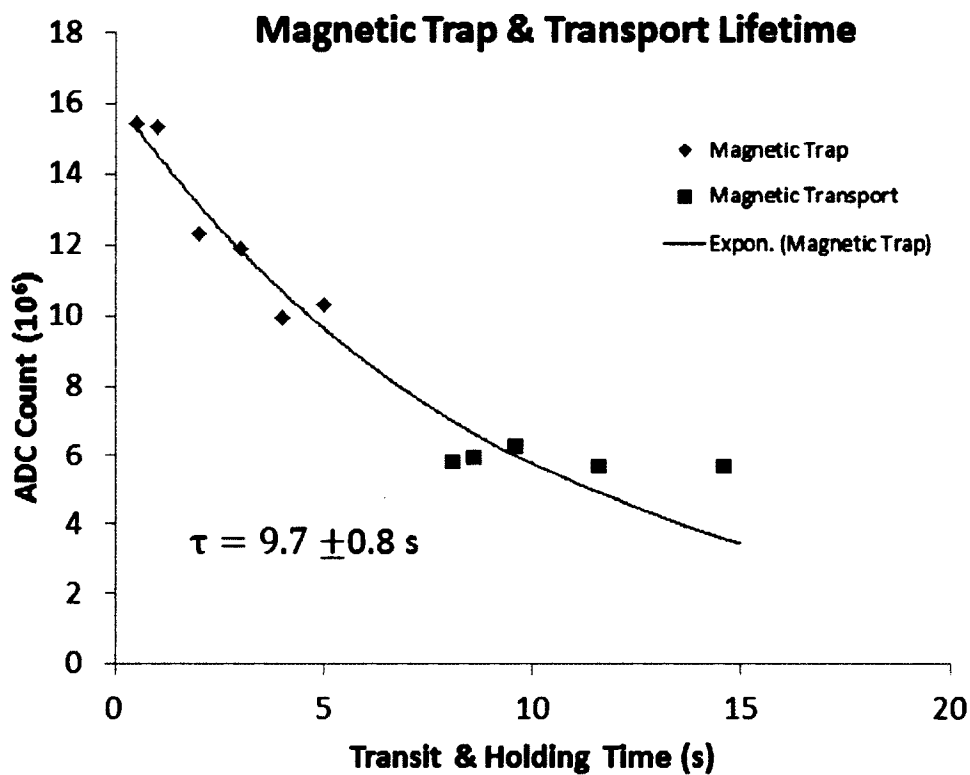


FIG. 7.9: Lifetime of ^{87}Rb atoms in the transport system as compared to those held in the MOT cell magnetic trap. The atoms are taken to the corner region, where they are held briefly before returning to the MOT cell for imaging. The atom numbers of transported atoms are consistent with the 9.7s lifetime measured in the MOT cell. The solid line is an exponential fit to the B-trap data shown in blue. This is the lifetime measured at the time of the transport testing, and not necessarily indicative of the typical MOT cell lifetime.

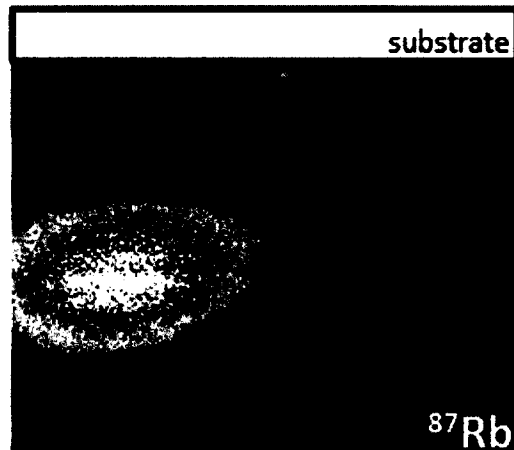


FIG. 7.10: Fluorescence image of transport and chip trap atoms during the handoff from the transport system to the atom chip.

As the transport coils cool down during the MOT and atom chip stages, the system can cycle indefinitely if programmed with a 30 second sequence from the start of the MOT to the atom chip experiment and imaging, a duty cycle of 23%.

CHAPTER 8

Potassium Laser Cooling System

The power of the trapping beam affects the number of atoms collected in the MOT. In the special case of potassium, the cooling transition is not as closed as that of rubidium, and so the repumping light also provides some cooling, and thus requires more power. With more available power, the MOT can be operated at higher detunings or with larger trapping beams. Both of these techniques yield higher atom numbers, thus an amplifier is used to provide enough power to achieve favorable MOT efficiency.

In the case of rubidium, our 780 nm diode lasers are capable of providing approximately 25 mW of post-fiber coupled seed light to a single-pass tapered amplifier resulting in an output power up to 380 mW of usable power. In practice, this system provides enough power to effectively collect several 10^9 ^{87}Rb atoms in just under 20 seconds; however, the lower output of the 767 nm potassium laser diodes results in significantly less available post-fiber seed light. To remedy this, the system was initially configured to daisy chain the 767 nm TA into the 780 nm TA, yielding 220 mW of 767 nm MOT light. This was enough to successfully trap and load ^{39}K onto the atom chip, but it prevented the simultaneous operation of both

species. To remedy this situation, the 767 nm TA was eventually reconfigured as a double-pass amplifier capable of similar power output to the MOT while requiring significantly less seeding power. This chapter provides discussion of the necessary trap and repumper frequency tunability, schemes for single-pass and double-pass tapered amplifiers, and a characterization of the potassium MOT performance.

8.1 Trap and Repumper Tunability

In rubidium, Doppler cooling is usually performed in the large detuning regime, $\delta \ll \Gamma$, so as to keep the scattering rate low enough that spontaneously emitted photons do not rescatter and interfere with the cooling operation. Spontaneously emitted photons from the center of the cloud can rescatter on their way out, effectively creating a repulsive heating force that works against the cooling light. The rescattering can be reduced by increasing the detuning δ thereby improving the cooling efficiency. Many atomic structures are not two level systems, and it is naturally assumed that the detuning must also be less than the hyperfine splitting Δ to the next lower level. The presence of blue detuned transitions tend to lead to a heating mechanism, though this is not always the case. One counter example has come to be known as grey molasses [79, 80].

The narrow hyperfine structure of the ^{39}K D2 transition, depicted in Figure 8.1, severely limits the ability to detune δ to reduce the scattering rate of the cooling light, and thus sub-Doppler cooling is not observed in the same straight-forward manner that it is for isotopes with larger hyperfine splittings, such as ^{87}Rb . Work has been done to explore regions between nearby D2 hyperfine levels of ^{39}K where the cooling force will provide usable sub-Doppler cooling as well as methods of leveraging those regions to cool large density samples [35]. For this reason we have designed our potassium trap detuning range to fully span the entire 33.5 MHz D2

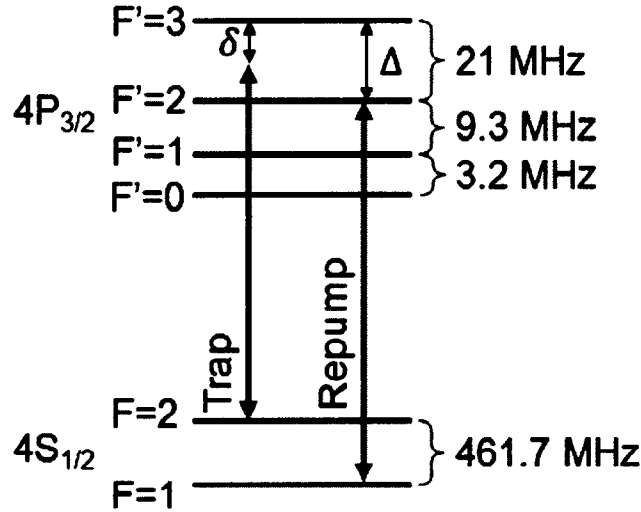


FIG. 8.1: The relevant energy levels for the laser cooling of ^{39}K . This diagram has been generalized from that Figure 2.4 where the trap laser is traditionally detuned from the unresolved excited state. In this case, we anticipate the ability to tune the *trap* laser between the hyperfine levels.

hyperfine splitting of ^{39}K .

The double pass AOM that provides the seed for the trap injection laser outlined in Figure 4.3 has been carefully aligned to maintain lock from the $4S_{1/2}F = 2$ to $4P_{3/2}F = 3$ resonance to well below the $4P_{3/2}F = 0$ hyperfine level (approximately 90 to 66 MHz AOM drive frequency). The power available from the double pass detuning AOM directly affects the quality of the injection lock and thus the tunable range of the laser is limited by the efficiency of the AOM setup. Figure 8.2 plots the double pass efficiency of the 80 MHz AOM used for the potassium trap injection lock detuning.

The repump laser detuning is somewhat independent of the trap, allowing it to remain detuned from the $F = 1$ to $F' = 2$ transition while the trap detuning is adjusted. This is an important difference between the laser systems of the two species. The rubidium laser system uses an offset to lock the repumper to the master trap itself and needs no external optimization for operation. ^{39}K requires a significantly

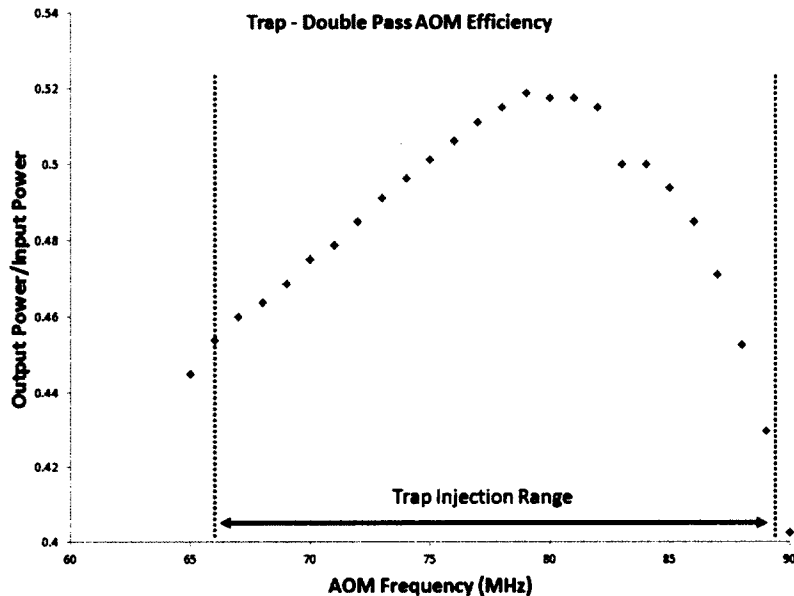


FIG. 8.2: Efficiency as a function of frequency for the ^{39}K trap double-pass AOM. The quality and range of the trap injection lock diode laser depend on the alignment and power from the double-pass AOM that is used for frequency control.

higher repumper to trap power ratio (1:2) for laser cooling as the repumper itself provides some additional cooling force. This also means that the repumper detuning must be controlled and optimized for all optical processes including the MOT, molasses, optical pumping and imaging. The double pass AOM that provides the seed for the repumper injection laser has been carefully aligned to maintain lock over a ± 5 MHz range centered on the $4S_{1/2}F = 1$ to $4S_{3/2}F = 2$ resonance. Figure 8.3 plots the double pass efficiency of the 310 MHz AOM used for the potassium repumper injection lock detuning.

8.2 Single-Pass Tapered Amplifier

Alignment of the traditional single-pass tapered amplifier (TA) requires several considerations that can be generalized to the alignment procedure of a double-pass

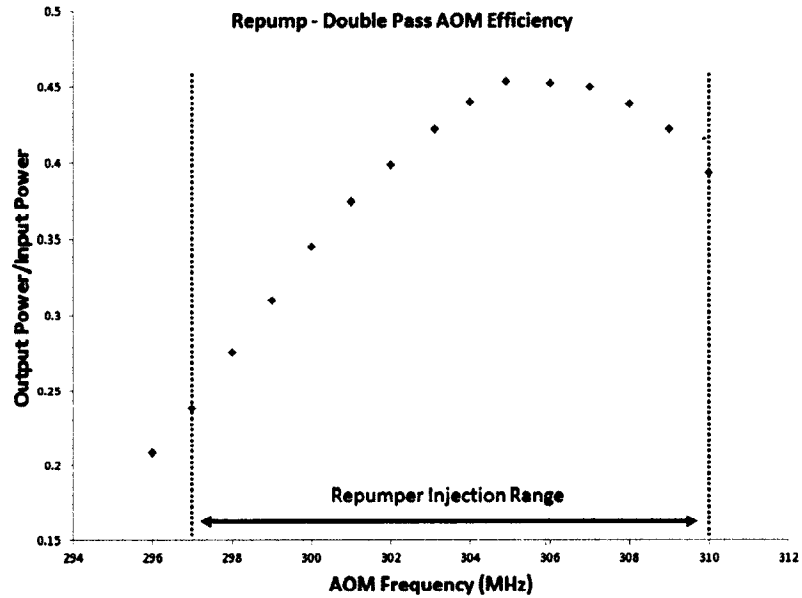


FIG. 8.3: Efficiency as a function of frequency for the ^{39}K repumper double pass AOM. The quality and range of the repumper injection lock diode laser depend on the alignment and power from the double-pass AOM that is used for frequency control

system. Naturally, to achieve a high coupling efficiency, we want as much seed light to be incident on the active region of the rear facet of the TA (small side). We use a TA mount design modified from the work of [81]. An aspheric lens is mounted directly to the copper TA mount, centered on the small side. I have found it helpful to add teflon tape to the threads of the lens mount to help secure it snugly. With the TA laser diode current (I_{LD}) set between 0.75 to 1 A, the input aspheric lens should be used to collimate the back fluorescence from the unseeded TA as well as possible, while also avoiding clipping from the aspheric lens mount.

It is sometimes necessary to use an IR viewer to see the far-field mode of the beam. It is recommended that a seed beam, ideally from a fiber, is mode-matched to the back fluorescence and co-aligned using two mirrors as shown in Figure 8.4. The seed power should be kept below 30 mW (50 mW max).

The seed beam should then be “walked” using two steering mirrors to maximize

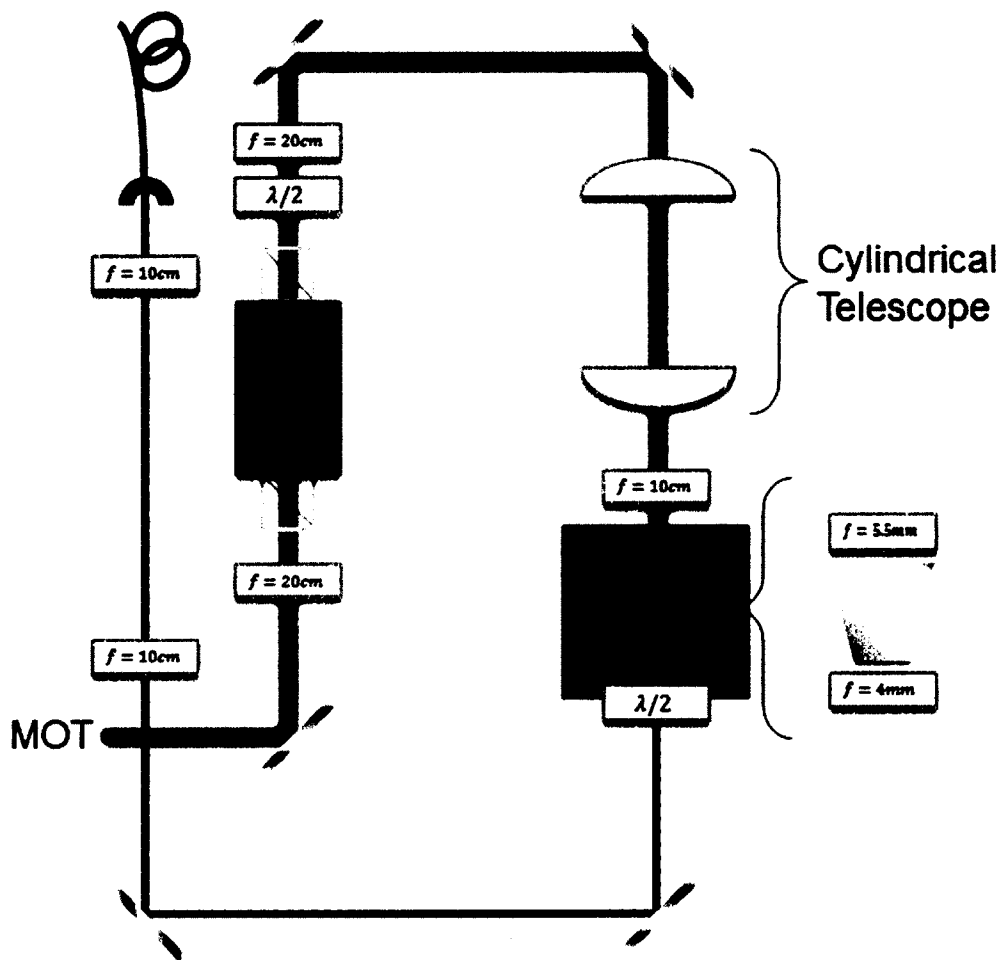


FIG. 8.4: Block Diagram of the Single Pass Tapered Amplifier (rubidium and potassium). A fiber coupled seed beam is coupled into the small side of the tapered amplifier via two-lens telescope and two steering mirrors. The anisotropic output of the tapered amplifier is collimated through the use of a cylindrical lens telescope, and then isolated through a Faraday optical diode.

the coupling efficiency of the seeded light to the amplifier. It is often helpful to put in a temporary lens and focus the outgoing light onto a power meter to monitor the input coupling. This must be done at low I_{LD} (< 1 A). A good efficiency is a gain of roughly $10\times$ at $I_{LD} = 1.6$ A.

The output side of the TA is tapered and the amplified light produced is astigmatic, and it diverges much more rapidly in the horizontal direction than the vertical. The mount is designed to hold a second aspheric lens on the output side which is used to collimate the vertical axis of the seeded light. An externally mounted cylindrical lens is then used to collimate the horizontal axis. Although in practice we have found it more helpful to use a two lens cylindrical telescope.

The near-field mode of the amplified light is not ideal, so all collimation of the output beam should be done while looking > 1 m away. With the output collimated, the beam is then sent through an optical isolator centered on a 1:1 telescope equipped with a shutter before being sent to the MOT distribution optics.

I have found that it is sometimes not possible to select an aspheric lens that will appropriately collimate one axis without clipping the light on the lens mount. In this case, a plano-convex lens is mounted externally to form a telescope with the on-board aspheric lens. The K TA uses this scheme and also requires the use of a cylindrical telescope to then collimate the horizontal axis. When implemented on the laser table, 15 mW of available seed power generated 300 mW of output power, however poor output beam mode, probe beam requirements, and 50% fiber coupling efficiency delivers a best-achieved scenario of 65 mW delivered to the apparatus table. For this reason, the potassium trapping results reported in Chapters ?? and 5 were achieved by daisy-chaining the single-pass potassium TA into the Rb TA. When transplanted to the apparatus table, the seed power dropped to 3 mW after the fiber as the seed beam now drives the probe paths as well.

8.3 Double-Pass Scheme

The double-pass scheme and alignment as depicted in Figure 8.4 is not that different from the single pass system although the differences make it much more difficult to align. It is best to start from a single-pass system in order to collimate the amplified light as well as possible. In a double-pass configuration, the seed beam is coupled in through the rejection port of the optical isolator. Alignment should be done with less than 1 A. The optical isolator is centered on a 1:1 or 2:1 telescope for the output of the TA. It is best to first align the seed beam to the TA without a lens through the rejection port of the optical isolator. Using ~ 3 mW, walk the seed beam using mirrors before the isolator to align it to the output of the TA. Reverse amplified light can be monitored at the small side of the TA using a power meter. Once it is maximized, a lens is placed on the seed beam path before the rejection port of the isolator and adjusted using a X-Y translation lens mount (Thorlabs LM1XY), which forms a telescope with the lens on the input side of the isolator. This lens is used to collimate the seed beam post isolator with fine control over its X-Y alignment to the TA.

Once the reverse pass coupling is maximized and stabilized, the outgoing beam is sent through a cube and $\lambda/2$ waveplate to monitor the power. The light should still be collimated from the single pass procedure and can be retro-reflected back into the TA. Care must be taken that the total light incident onto the TA is kept below the damage threshold of 50 mW. I have found that using a $f = 10$ cm lens to focus the reverse pass beam onto a premium stable mirror mount (Thorlabs POLARIS-K1-H) for retro-reflection results in much more stable coupling and higher efficiency. The second pass through the $\lambda/2$ waveplate rotates the retro beam polarization to realign with that of the TA. Double passed light can now be monitored at the output of the optical isolator. As described here, our K TA system generates 300 mW from

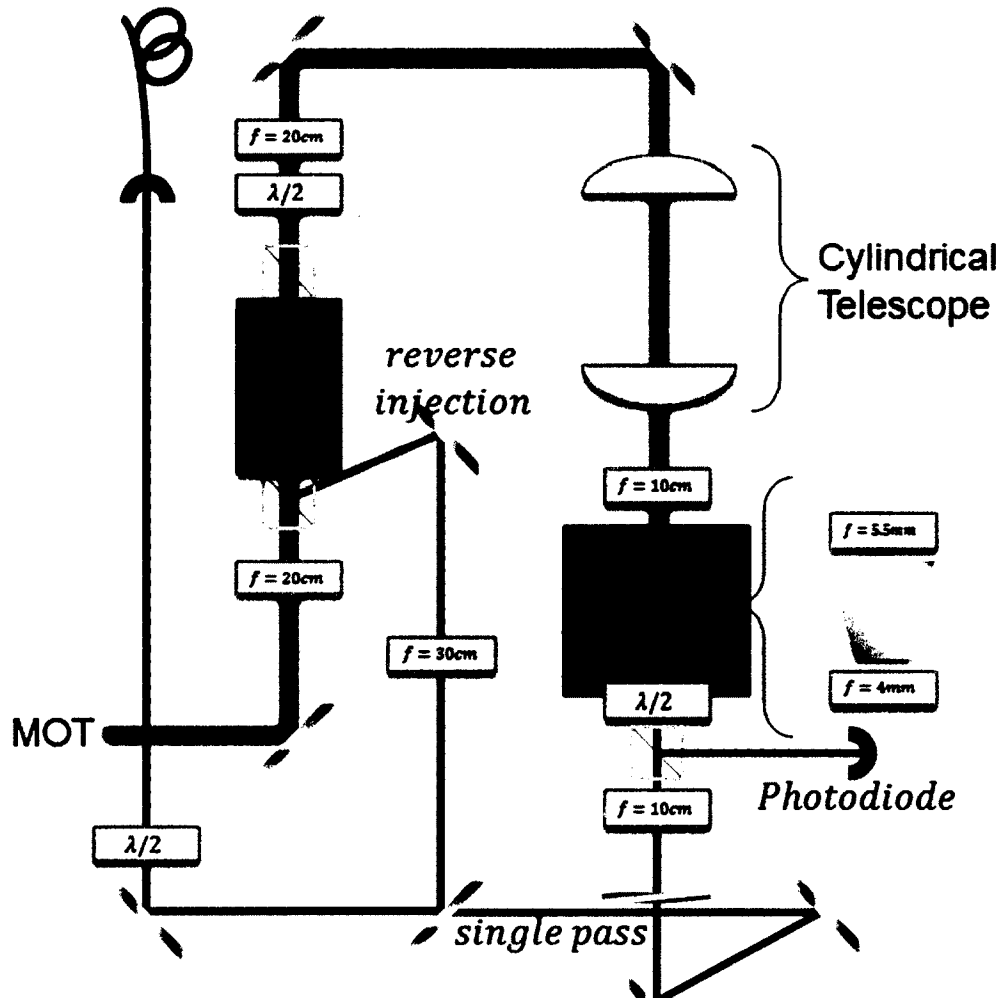


FIG. 8.5: Block Diagram of the Double Pass Tapered Amplifier used for potassium. A fiber coupled seed beam is coupled into the rejection port of a Faraday optical diode. The diode presents an interesting component of the tapered amplifier as there is a shared telescope both on the output path as well as the input path. The seed beam is coupled in reverse through the cylindrical telescope into the large side of the TA. Amplified seeded light emerges from the small side of the TA and is collimated and retro-reflected back into the TA, becoming further amplified on the second pass through the amplifier. The output beam is collimated by the cylindrical telescope and isolated by the Faraday optical diode. Alignment of a double-pass amplifier is very tedious and is best begun from an operational single-pass amplifier. As such, the single pass input beam is shown in this diagram as the dashed red pathway coupled into the small side of the TA.

3 mW seed power. Due to further beam shaping to improve the far-field mode and beam splitting to seed the Fabry-Perot cavity, the usable MOT power is $1/3$ to $1/4$ of the TA output.

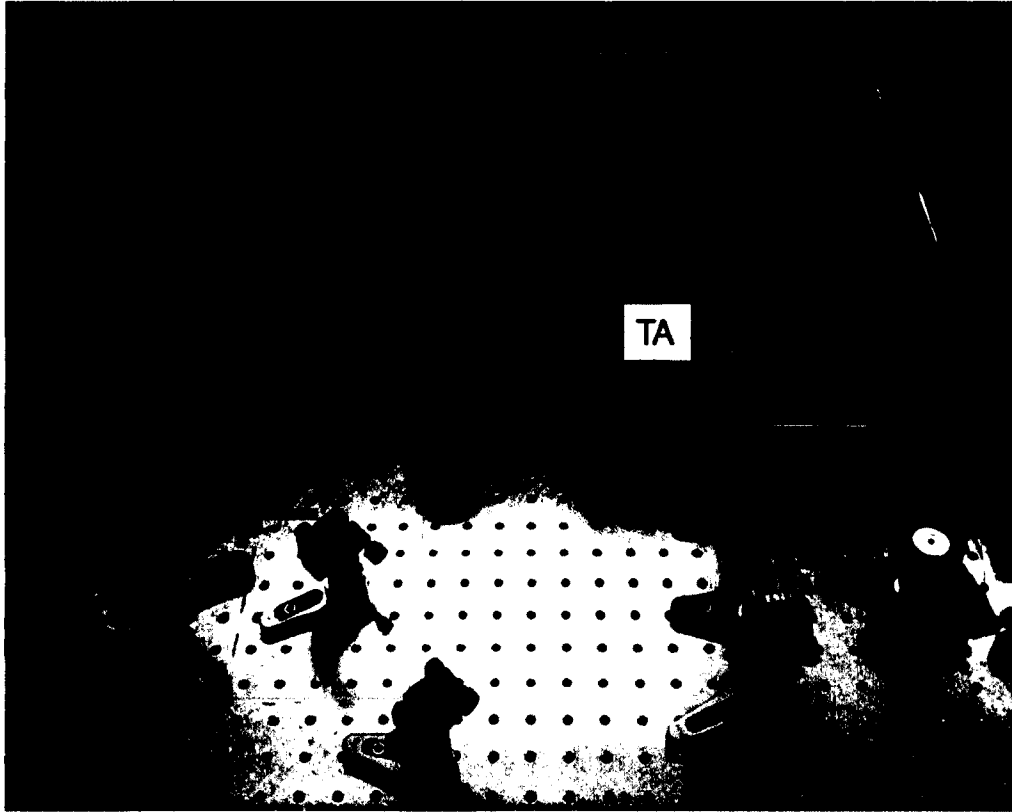


FIG. 8.6: A photo of the potassium double pass tapered amplifier as built on the apparatus table. The orange arrow represents the reverse-pass seed beam and the red arrow represents the output beam from the second pass through the amplifier.

8.4 ^{39}K MOT Loading Rate

The most noticeable impact of an increase in available trapping power is the effect on the MOT loading rate. Ideal behavior of the atom population trapped and cooled in a MOT resembles that depicted in Figure 8.7. The MOT population, $N(t)$, grows with a linear accumulation period before it begins to saturate from

density-influenced effects. The simplest model of MOT population is

$$N(t) = N_{sat}(1 - e^{-t/\tau}) \quad (8.1)$$

where τ represents the lifetime which depends on the vacuum quality and MOT density, more so at higher densities. The rate of change of atom number is then

$$\frac{dN}{dt} = \gamma - \frac{N}{\tau} \quad (8.2)$$

where γ is the loading rate, a quantity that depends on cooling beam intensity, size, detuning of both the trap and repumper components and the vacuum density of potassium. As $t \rightarrow \infty$, the population N saturates to N_{sat} and so the rate of change goes to zero. Writing this out for clarity yields the expressions

$$\begin{aligned} \frac{dN}{dt} = 0 &= \gamma - \frac{N_{sat}}{\tau} \\ \Rightarrow \gamma &= \frac{N_{sat}}{\tau} \\ N_{sat} &= \gamma\tau. \end{aligned} \quad (8.3)$$

It is worth noting that the saturation or equilibrium level is a complicated beast affecting many factors, including experimental limitations such as the geometric size of the MOT beams as well as the radiation pressure from spontaneously emitted photons. As the MOT collects and cools atoms, the atomic density increases and can eventually reach a point where the chance of a spontaneously emitted photon from the cooling process not escaping the cloud before interacting with another atom tends to one. At this point, the momentum kick transferred to the second atom can be seen as a repulsive force. This radiation pressure puts an upper limit

on the achievable atomic density. This is a far more complicated phenomenon to explore and is beyond the scope of this thesis.

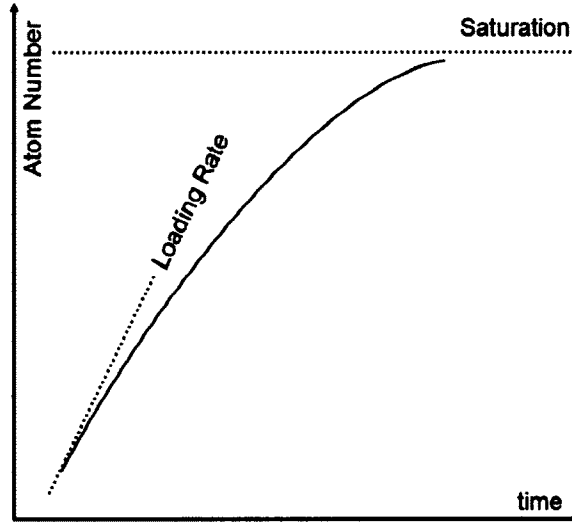


FIG. 8.7: Illustrative definition of MOT loading loading and saturation atom number.

With the available power from the double-pass tapered amplifier, a study was performed of the effect of cooling light intensity on the MOT loading rate. The KMOT parameters listed in Table 5.1 were maintained throughout, including the trap and repumper ratio; the only variable was the overall intensity. The loading rate was extracted from the behavior of the MOT at a range of cooling laser powers. The camera parameters were kept constant throughout the experiment and relative atom number was extracted from the camera ADC counts.

The relationship is clearly correlated, although a fit would be an inappropriate speculation in this data set. Wieman predicts a linear increase with beam power in rubidium [82]. Our system was limited by the amount of available power as well as the ability to image a lower power MOT (< 40 mW) using the common imaging parameters.

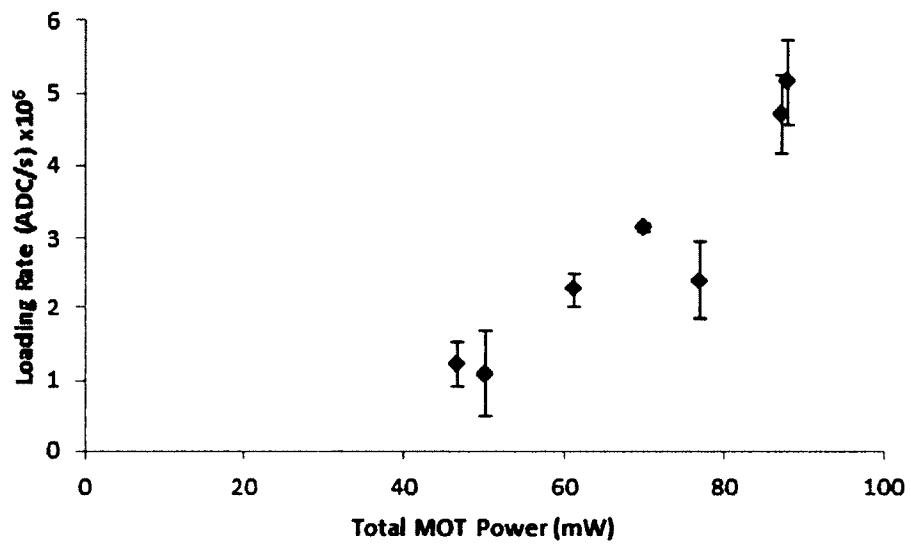


FIG. 8.8: ^{39}K MOT loading rate as a function of the total MOT beam intensity. Each data point in this set is a fit to the loading rate as defined in Figure 8.7. Each loading rate data point was recorded as an average of multiple data sets.

CHAPTER 9

Microwave Evaporation System

The original motivation for a dual-species apparatus was that potassium would be a smarter choice of atom for demonstrating μ /RF potentials on atom chips. Successes reported in Chapter 5 included a ^{39}K MOT, magnetic trap, and the transport and loading of the atom chip. The next logical step would be the sympathetic cooling of the limited ^{39}K by selectively evaporating ^{87}Rb , bringing the potassium to ultracold temperatures ($1\mu\text{K}$) for experiments with μ /RF potentials.

9.1 Evaporative Cooling

The laser cooling techniques (MOT and molasses) described in subsection 2.2.3 provides both cooling and trapping, but with an inherent lower limit on achievable temperatures (μK -level) and phase-space densities of 10^{-5} to 10^{-6} . It is worth noting that some hybrid techniques can reach phase space densities of 10^{-3} [83]. Magnetic trapping alone provides only confinement, with no cooling ability other than simple thermalization. An additional cooling technique was introduced to bridge the gap between MOT phase-space densities of $\rho \sim 10^{-6}$ and those needed to reach quantum degeneracy ($\rho \sim 1$).

First used to cool hydrogen atoms in 1988 [84], evaporative cooling is the selective removal of *hotter* or *faster* atoms from a trapped cloud. The subsequent rethermalization of the gas occurs via two-body elastic collisions, lowering the average kinetic energy while reaching a lower equilibrium temperature. The threshold at which atoms are removed is continuously lowered, allowing an arbitrary reduction in temperature at the cost of reduced atom number. The process as illustrated in Figure 9.1 is limited by the number of trapped atoms and the maintainable collision rate.

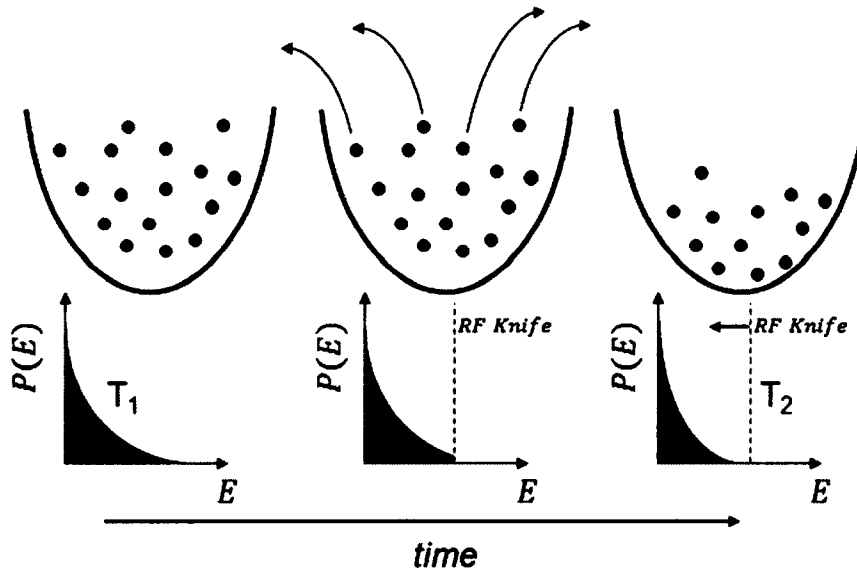


FIG. 9.1: Diagram of evaporative cooling. Removal of the hottest atoms can be done by lowering the trap depth or forcefully ejecting them through spin-flip transitions. If RF magnetic fields are used for the spin flip mechanism, it is known as an RF knife. The high energy tail of the T_1 is abruptly removed, and the system re-equilibrates via elastic collisions to a lower overall temperature, $T_2 < T_1$.

Evaporative cooling can be performed in a variety of ways. In optical dipole traps, the trap depth can be relaxed through reduction of the laser intensity and power, thus lowering the trap barriers and releasing the hottest atoms on their own recognizance. This also relaxes the confinement of the trap which can lower the

atomic density and reduce the collision rate. Furthermore, atoms held in an optical dipole trap are unpolarized, meaning a mixture of magnetic Zeeman sublevels are present. A method of evaporation through microwave or RF-induced spin flips is depicted in Figure 9.2.

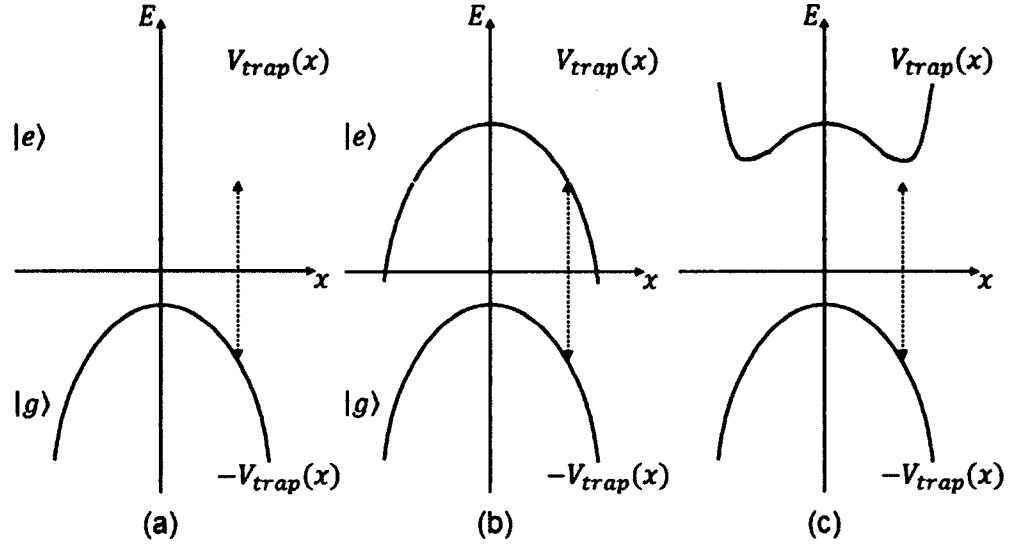


FIG. 9.2: (a) Diagram of evaporative cooling in the dressed atom picture (1D, spin = 1/2). Atoms are evaporatively cooled in trapping potential $V_{trap}(x)$ by coupling an μ RF field between the trapped and untrapped states. Atoms with enough energy to enter the region where the energy shift enters resonance with the μ RF field will release a photon through stimulated emission and escape from the trap. The orange curve describes the potential seen by the trapped state, whereas blue describes the anti-trapped state. (b) shows the crossover from trapped to anti-trapped and (c) depicts the potentials seen in the dressed atom basis.

Following a similar discussion of dressed atom theory as section 3.1, evaporation can be described by the Hamiltonian

$$\mathcal{H}_{rf} = \begin{bmatrix} -V_{trap}(x) & 0 \\ 0 & V_{trap}(x) \end{bmatrix} + \hbar\omega_{rf} \begin{bmatrix} N & 0 \\ 0 & N-1 \end{bmatrix} + \frac{\hbar}{2} \begin{bmatrix} 0 & \Omega_{rf} \\ \Omega_{rf}^* & 0 \end{bmatrix} \quad (9.1)$$

where $V_{Trap}(x)$ is the potential depicted in Figure 9.2, N represents the number of RF photons in the applied field, and Ω_{rf} is the Rabi frequency of the interaction. Resetting the energy offset allows Equation 9.1 to be simplified to

$$\mathcal{H}_{rf} = \begin{bmatrix} \hbar\omega_{rf} - V_{trap}(x) & \hbar\frac{\Omega}{2} \\ \hbar\frac{\Omega^*}{2} & V_{trap}(x) \end{bmatrix} \quad (9.2)$$

where the energy levels are

$$E_{e,g} = \frac{\hbar\omega_{rf}}{2} \pm \frac{1}{2} \sqrt{(\hbar\omega_{rf} - 2V_{trap})^2 + \hbar^2|\Omega|^2}. \quad (9.3)$$

9.1.1 Radio Frequency Evaporation

To effectively cool a magnetically trapped and *polarized* atomic sample, the atoms can be *forced* out through intentional spin-flipping with radio-frequency (RF) or microwave magnetic fields. *Forced evaporative cooling*, as it is known, is the primary mechanism employed in the system described in this work. Equating the average energy E_k with the magnetic Zeeman potential of Equation 2.33 yields the expression

$$E_k \approx g_F \mu_B m_F (B(\vec{r}) - B_{bottom}). \quad (9.4)$$

where the Landé g-factor g_F and magnetic moment μ_B are defined in Chapter 3. In other words, hotter trapped atoms tend to sample larger magnetic fields as they travel further out in the magnetic potential; these atoms can be selectively transferred into an untrapped magnetic state by an applied resonant RF magnetic field. The adjacent magnetic sublevels of the hyperfine state are often separated by almost identical *RF* transition frequencies, so they can easily be driven simultaneously. These $\Delta m = \pm 1$ transitions occur at a surface of constant energy described by the

expression

$$\hbar\omega_{RF} = \mu_B g_F B(\vec{r}) \quad (9.5)$$

where ω_{RF} is the frequency of the applied RF magnetic field.

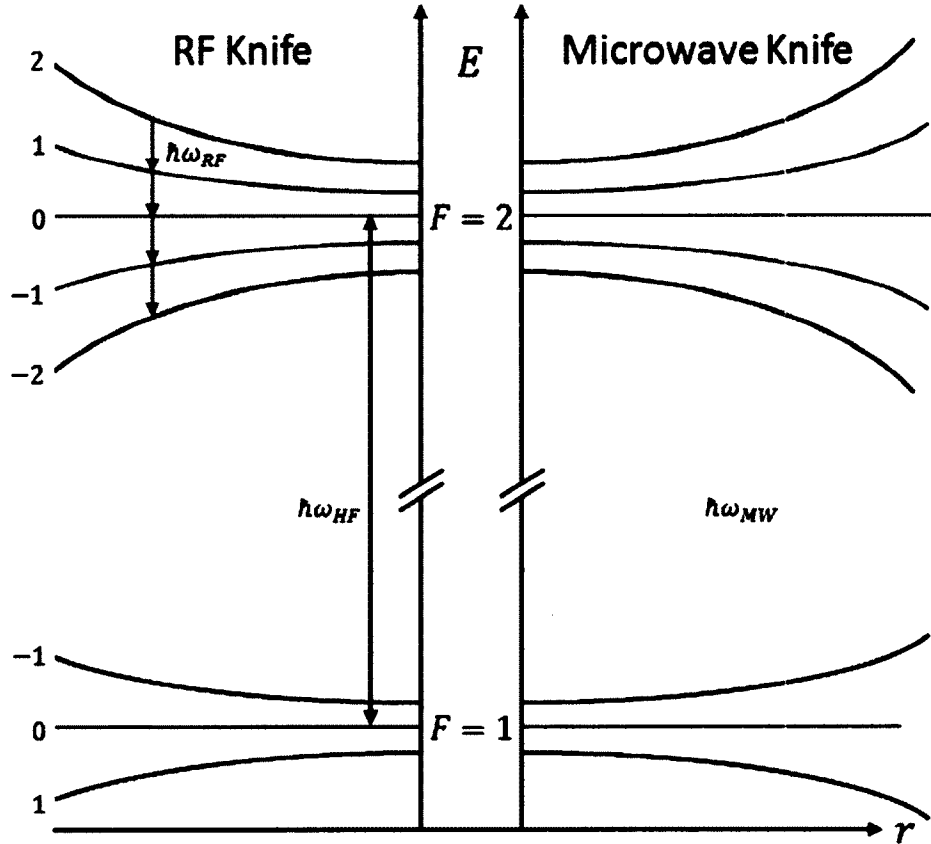


FIG. 9.3: Magnetic sublevels used in microwave and RF evaporation. Green arrows represent radio frequency transitions that are driven simultaneously for forced RF evaporation. Orange arrows represent a microwave transition that is selectively driven. The dashed orange arrow represents a path where ejected atoms can transition back to a trapped state, and must be avoided by other means.

In the $|F = 2, m_f = 2\rangle$ state of ^{87}Rb and ^{39}K , this technique, also known as an *RF knife*, drives sequential transitions between adjacent Zeeman sublevels as depicted in Figure 9.3, through the untrapped $m_F = 0$ state and into the anti-trapped $m_F = -1$ and $m_F = -2$ sublevels where the atoms are ejected from the trap. This

technique could also be described as a lowering of the trap depth without changing the shape of the center of the trap. The splitting between adjacent magnetic hyperfine states of ^{87}Rb ($5S_{1/2}$) and ^{39}K ($4S_{1/2}$) where $g_F = 1/2$ can be expressed as

$$\frac{E_{\text{potential}}}{B} = \frac{\mu_B g_F m_F}{h} \approx 0.7 \text{ MHz/G.} \quad (9.6)$$

While the RF knife is effective in cooling ^{87}Rb into a Bose-Einstein condensate, it is not without its drawbacks. Atoms transitioning through the $-|2, 1\rangle$ state can linger and collide with atoms in the desired $|2, 2\rangle$ state resulting in spin-flipping and heating. Furthermore, as the RF transition is almost exactly the same for both ^{87}Rb and ^{39}K , it is not possible to perform sympathetic cooling where one species acts as a coolant, undergoing RF evaporation while remaining in thermal equilibrium with the other species. A technique such as this is advantageous as it does not deplete the atom number of the secondary species.

9.1.2 Microwave Evaporation

Evaporative cooling can also be performed directly between the $F = 2$ and $F = 1$ hyperfine levels via microwave frequencies. In ^{87}Rb , this transition frequency is $\omega_{MW} \approx 2\pi \times 6.834 \text{ GHz}$, hence the term *microwave* evaporation. Usually the microwave signal is targeted from the trapped $|2, 2\rangle$ state to the anti-trapped $|1, 1\rangle$ state. In ^{87}Rb , this transition can be expressed as

$$\hbar\omega_{MW} = \hbar\omega_{HF} + 3\hbar\omega_{RF}. \quad (9.7)$$

In ultracold atomic physics, we often speak in terms of temperature depth

instead of energy. The evaporating knife edge could be described as

$$\begin{aligned}\frac{\omega_{RF}}{T} &= \frac{k_B}{2h} = 0.01\text{MHz}/\mu\text{K} \\ \frac{\omega_{MW}}{T} &= \frac{3k_B}{2h} = 0.03\text{MHz}/\mu\text{K}\end{aligned}\tag{9.8}$$

In practice, a starting frequency for the evaporation knife is chosen and it is ramped down to maintain continuous cooling of the atomic cloud. During microwave evaporation, there is still a mechanism for atoms transfer from the anti-trapped $|1, 1\rangle$ state into the usually unwanted $|2, 1\rangle$ state before they have left the trap, though it is somewhat mitigated by the presence of B_{offset} . Figure 9.3 illustrates this unwanted path that leads to heating and atom loss through spin-exchange collisions with the trapped and cooled $|2, 2\rangle$ state. A secondary frequency could be used to prevent this process from occurring, such as a microwave sweep targeting the transition from $|2, 1\rangle$ to $|1, 0\rangle$ [85, 86].

9.1.3 Sympathetic Evaporation

As motivated in the chapter introduction, the primary objective of the 6.8 GHz evaporatoin system is to provide sympathetic cooling of the limited ^{39}K by selectively evaporating ^{87}Rb , bringing the potassium to ultracold temperatures ($1\mu\text{K}$) for experiments with μ/RF potentials. In this configuration, rubidium is considered the *coolant* and undergoes standard forced evaporation while held in thermal contact with potassium. Collisions between the two species provide a mechanism for maintaining thermal equilibrium by the transfer of kinetic energy from potassium to rubidium as demonstrated in Figure 9.4. After the potassium is sufficiently cooled, any remaining rubidium is removed from the trap. The details of the interaction rely heavily on the collisional properties of the target isotopes, a topic that has been explored in depth [87, 88] although it is outside the scope of this thesis.

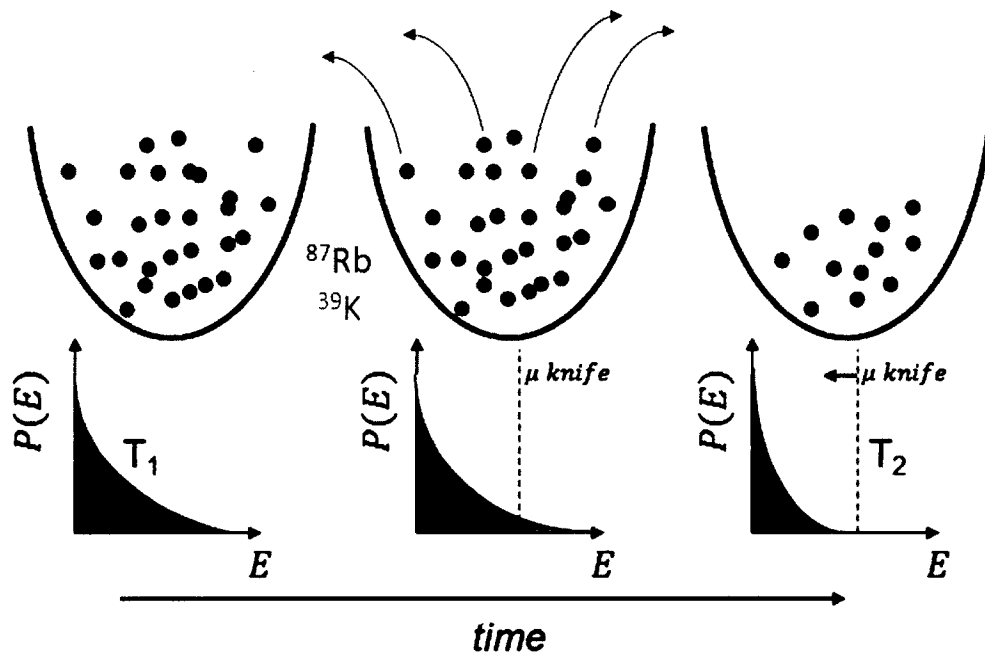


FIG. 9.4: Diagram of sympathetic evaporative cooling. Removal of the hottest atoms of one species (ie ^{87}Rb) can be done by lowering the trap depth or forcefully ejecting them through spin-flip transitions. The high energy tail of the T_1 is abruptly removed, and the system re-equilibrates with a second species (ie ^{39}K) via elastic collisions to a lower overall temperature, $T_2 < T_1$. As the coolant is evaporated, the sympathetic species maintains its atom number. Analogous to the RF case, this technique employs a microwave knife to perform the spin flipping.

9.2 6.8 GHz Evaporation System

This section is intended to describe the design and implementation of the 6.8 GHz evaporation system (affectionately known as *Dr. Watts*). At 6.8 GHz in the micro-magnetic trap of our atom chip we anticipate evaporation will require 1 W of microwave power delivered to the chip wires. Whereas the RF evaporation in atom chip worked efficiently in a sweep from 20 to 3 MHz, the microwave system requires a tunability that is three times larger to accommodate the DC Zeeman shift in the atomic hyperfine levels. Consequently, we have designed a system with at least 60 MHz of tunability at 6.834 GHz.

9.2.1 Design and Theory of Operation

A pair of 6.8 GHz 29 dBm nominal amplifiers were purchased on eBay (Terrasat PA5336-12-061-11). These amplifiers feature a voltage variable attenuator (VVA, 0.05 to 4.9 V), a TTL mute and a logarithmic power detector. The target input power range is -24 to -18 dBm with a gain of $+50$ dBm. As they require four different supply voltages to operate (5.5 V/2.5 A, 8 V/2.5 A, ± 12 V/1.8 A), support electronics were designed to power and interface with the amplifier. This amplifier was designed to drive both the atom chip wires as well as a waveguide-turned-horn for the MOT cell.

A temporary 6.8 GHz source that is stable to within 100 kHz was installed internally with the amplifier hardware (Mini-Circuits, ZX95 6840C+). The amplifier can be driven by this $+1$ dBm source or by a much more stable (1 Hz) external source (SynthNV). GHz-specific attenuators are used to bring the input power down to the specified -18 dBm level. The amplifier output is isolated using a 6.8 GHz circulator (Pasternack, PE8402) which prevents any reflections from the load from reaching the amplifier. The circulator also allows the frequency and power to be monitored

by sending the reflection signal to a microwave counter (HP 5342A).

The amplifier and its control and support circuitry was designed and assembled by A. Pyle under my guidance and testing. For this reason, I leave the specific circuits to be the subject of his dissertation while I present a block diagram of the design depicted in Figure 9.5. C. Fancher and AJ Pyle were also responsible for the assembly and testing of the SynthNV source.

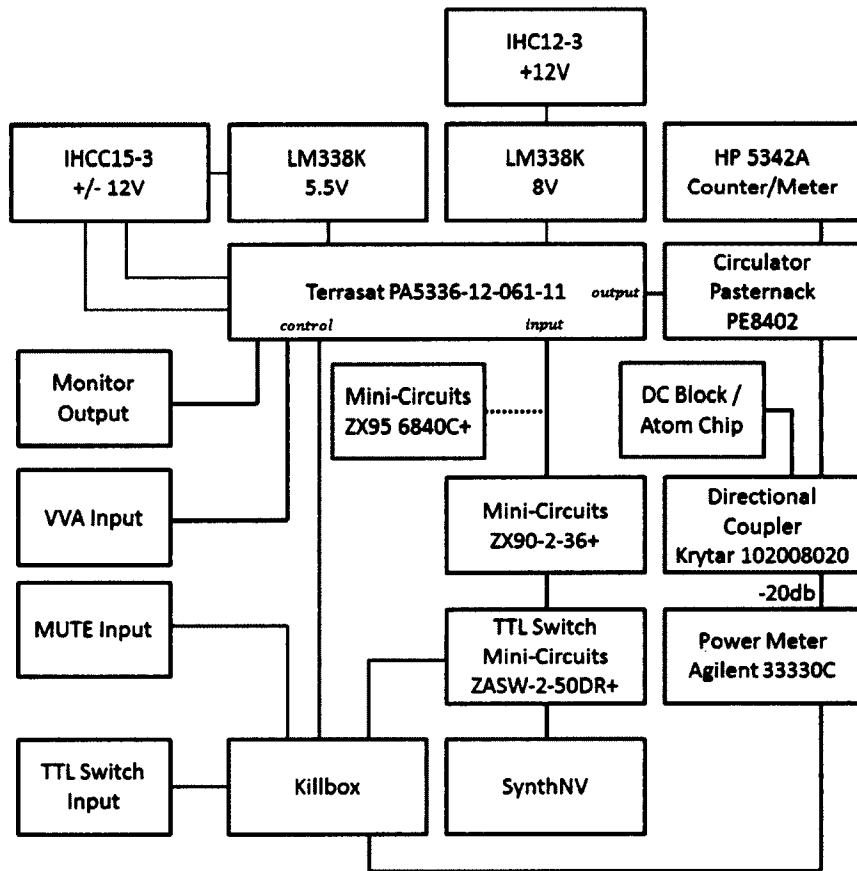


FIG. 9.5: Diagram of the 6.8 GHz Amplifier. Blue wires signify digital signals. Analog, power and GHz signals are shown in black. The lone dashed connection represents an alternate connection for the onboard 6.8 GHz source.

Care must be taken not to overdrive the load in any configuration. The atom chip wires have only been tested safely up to 1 A of DC current and these limits

must be respected.

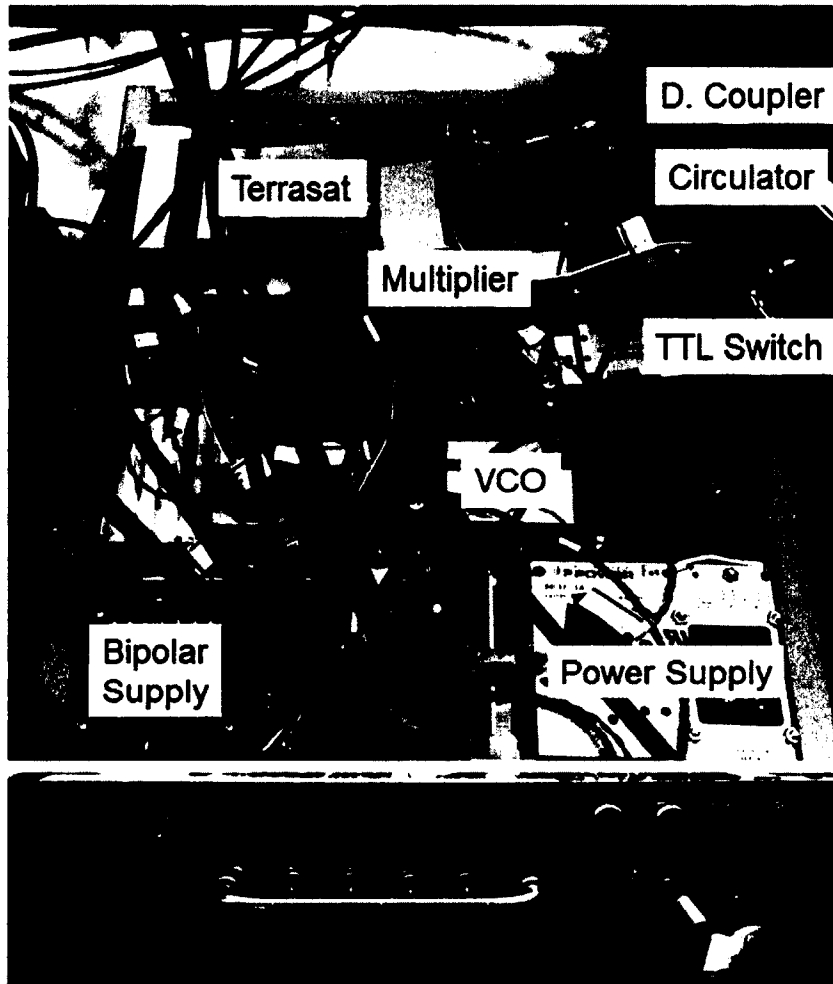


FIG. 9.6: Photo of the 6.8 GHz amplifier. This is a top-down view with the front panel shown below. Not shown is the SynthNV module and the Agilent 33330C counter and power detector.

9.2.2 Performance

The 6.8 GHz system is fully operational and has been used to evaporatively cool ^{87}Rb in the atom chip micro-magnetic trap. An example of this is shown in Figure 9.7 where a 2.5 s ramp from 6.891 to 6.858 GHz cools the atomic cloud while increasing the atomic density and subsequently the collision rate. In theory, the

microwave evaporation provides a cleaner method of cooling ^{87}Rb as it does not populate the $|2, 1\rangle$ state, which can cause heating through collisions with the target $|2, 2\rangle$ state.

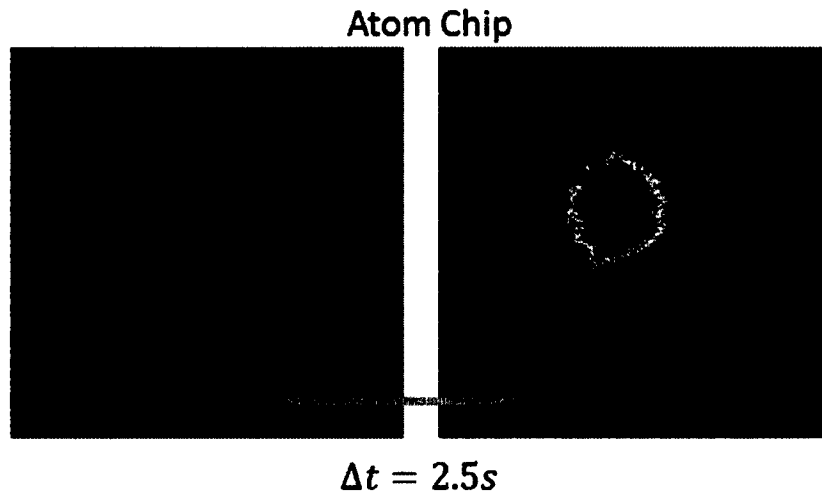


FIG. 9.7: First evidence of microwave evaporation at the atom chip. A 2.5 s ramp from 6.891 to 6.858 GHz cools the cloud while increasing the atomic density.

9.3 Ultracold Atomic Tests and Techniques

Although the 6.8 GHz system was constructed specifically for sympathetic cooling of potassium atoms, it also unlocks a specialized set of techniques for the manipulation of ^{87}Rb . In this section I describe how the microwave system is used to “clean” unwanted magnetic sublevels from the population, using Stern-Gerlach imaging as a diagnostic. Also presented here is adiabatic rapid passage, a technique developed in nuclear magnetic resonance that can be used to efficiently transfer a population of atoms between spin states.

9.3.1 Zeeman Level Cleaning and Stern-Gerlach Imaging

Certain experimental techniques result in a mixed population of magnetic sublevels in situations where the relative atom number is an important quantity. Perhaps one of the oldest magnetic techniques is the splitting of states by the application of a Stern-Gerlach field. By turning on the atom chip alone, a strong gradient is produced across the atomic cloud.

The various magnetic sublevels *see* different magnetic forces and are spatially separated. In our system, the $F=0, m_f < 0$ sublevels disappear from view as they are pulled into the chip surface, while the $m_f = 0$ remain round and untouched. The $m_f > 0$ sublevels are pushed away from the chip, spread out into an arc as the field from the Z-wire is circular in shape. The $m_f = 2$ magnetic sublevel is pushed twice as far as the $m_f = 1$ level and the $m_f = 0$ sublevel would remain unaffected.

Microwave evaporation can also be used to cleave unwanted states from a mixture, ensuring a pure sample remains. There are a multitude of mechanisms that cause a mixing of magnetic sublevels to occur. Regardless of the cause, unwanted states can be selectively removed by careful application of microwave evaporation. In one such case, atomic samples trapped on the atom chip contained $m_f = 2$ as well as an undesired population of $m_f = 1$ atoms. By introducing microwaves tuned to the $|F = 2, m_f = 1\rangle \Rightarrow |F = 1, m_f = 1\rangle$ transition where the final state is anti-trapped, these unwanted atoms can be selectively forced out of the trap. With careful tuning of the externally applied static magnetic field, this microwave field will remain sufficiently detuned from the $|F = 2, m_f = 2\rangle \Rightarrow |F = 1, m_f = 1\rangle$ transition, ensuring that the desired population remains intact. Absorption images of this *clean sweep* technique is shown are Figure 9.8.

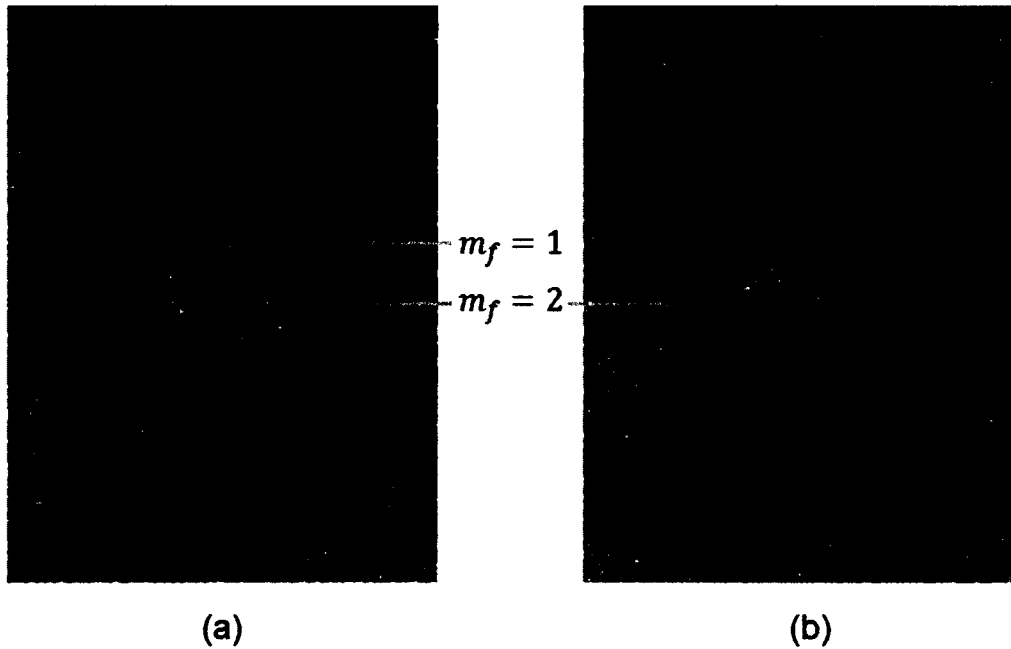


FIG. 9.8: Microwave level cleaning observed via absorption imaging of Stern-Gerlach separated spin states. During the time of flight, the atom chip is turned on to provide a gradient over the spatial extent of the atoms. The resulting force on the atoms causes different magnetic sublevels present to become spatially separated. Any $F=0$, $m_f < 0$ sublevels are subsequently pulled into the atom chip by the opposite sign of their Zeeman force. Multiple Zeeman levels are resolved in (a) including $|F = 2, m_f = 1\rangle$ and $|F = 2, m_f = 2\rangle$. b) Through careful introduction of microwaves tuned to the $|F = 2, m_f = 1\rangle \Rightarrow |F = 1, m_f = 1\rangle$ transition, the $|F = 2, m_f = 1\rangle$ states are selectively removed, or “cleaned”.

9.3.2 Adiabatic Rapid Passage

Adiabatic Rapid (Fast) Passage (ARP) is a staple technique of continuous wave nuclear magnetic resonance that allows an entire polarized population of states to transition seamlessly between magnetic sublevels through careful application of static and oscillating magnetic fields. As an alternative to a Rabi-flopping transition, ARP uses either a frequency sweep or a static field sweep over a range containing the transition resonance. In this application, the microwave frequency is swept while the static quantization field is held constant. The sweep range is much wider than the resonance width, and so the transfer efficiency is insensitive to small variations caused by stray magnetic fields.

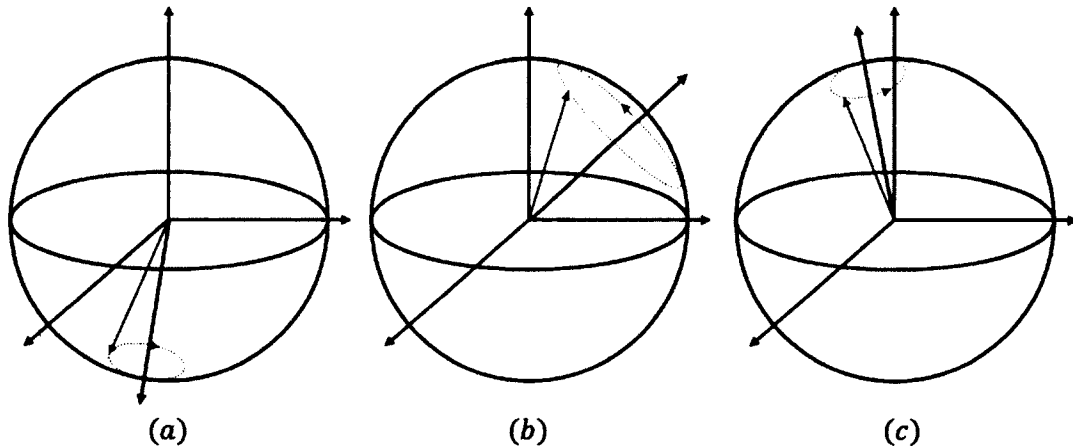


FIG. 9.9: Bloch Sphere depiction of adiabatic rapid passage of a two-level system. (a) The Bloch vector (red) precesses about the effective bias field or *torque vector* (blue). (b) Sweeping of the applied microwave frequency causes the *torque vector* to rotate to the opposite pole of the Bloch sphere, as the Bloch vector follows it. (c) The Bloch vector now represents a population in the opposite state than that of (a).

In adiabatic rapid passage, the applied static magnetic and microwave fields combine to form the effective bias field, sometimes called the *torque vector*, about which the Bloch vector precesses. By sweeping either the static field or the mi-

crowave field magnitude, the effective bias field is rotated to the opposite pole of the Bloch sphere. If the rotation is performed slow enough, the Bloch vector will follow the torque vector; though the precession arc grows as the field conditions sweep through resonance. As the sweep proceeds to the opposite far-detuned regime, the precession arc decreases as nearly all of the atoms have transitioned into the excited state. This technique is completely reversible and is an effective means of transitioning between different hyperfine magnetic sublevels.

CHAPTER 10

Summary and Outlook

I am hopeful that this thesis has met its arguably lofty goals. The first being a record of relevant and useful information regarding the benefits and uses of atom chip μ /RF potentials. Although the group has not yet demonstrated μ /RF trapping, we are well on our way to achieving that goal. Spin-dependent potentials, species- and spin-selective forces and tuneable Feshbach resonances are simultaneously available in a compact, efficient package provided that careful attention is paid to future atom chip designs. The result that potential roughness is significantly suppressed by not one, but two distinct mechanisms with μ /RF potentials makes them 300% more awesome. It is my desire that the results presented here will guide the design and use of new atom chip systems that unlock new and previously unreachable experimental techniques.

The second purpose of this thesis was to serve as a primer, manual, and blueprint for the apparatus described within. The two chamber design has fulfilled its desired capacity for a versatile, streamlined system that is both adaptable and expandable for the future while minimizing any performance compromises, a swiss army knife if you will. Impressive optical access, robust magnetic trapping systems,

flexible optical trapping and imaging capabilities, and the ability to simultaneously work with rubidium and potassium species should provide a nearly endless potential for successful experiments. The versatility of the system to be reconfigured for fermionic ^{40}K and bosonic ^{41}K and ^{85}Rb species combined with the option to use the atom chip or optical dipole traps of either chamber for scientific experiments heralds the great attention to detail in the apparatus design by those who came before me.

10.1 Summary of Results and Limitations

This system cools, traps, and magnetically transports two species of alkali metals to a second chamber where it produces Bose-Einstein condensates of ^{87}Rb on the atom chip as well as the first example of chip-trapped ^{39}K in the world, a result that required many late nights and crossed fingers. This feat requires careful tuning of potassium MOT parameters to achieve the described semi sub-Doppler cooling and atom number necessary for success. It is clear that production of ultracold ^{39}K samples will only improve with increased MOT power. This is as efficient as the potassium double pass tapered amplifier system is, it is clearly limited by lack of available seed power, a limitation that can easily be lifted with some key investments to the laser system, such as more powerful injection lock laser diodes at 767 nm.

10.2 Outlook and Potential Improvements

Although the system was designed to develop ultracold ^{39}K as the platform for the first μ/RF potential experiments, the coupling of the 6.8GHz amplifier to the atom chip may be strong enough to warrant a μ/RF demonstration attempt using ^{87}Rb . I believe the world's first on-chip degenerate ^{39}K sample can be achieved by

improving the atom number with the aforementioned laser system upgrades and carefully implementing on-chip sympathetic cooling at 6.8GHz with ^{87}Rb . A dual species sample on the atom chip is the ideal platform to start checking off the following incomplete list of μ/RF techniques and applications:

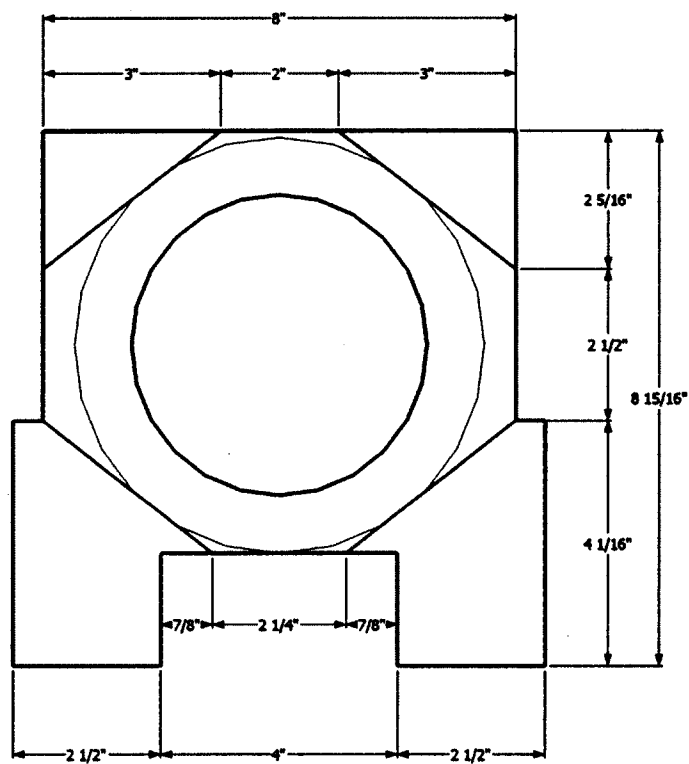
- Spin-dependent forces: use μ/RF to manipulate ^{39}K or ^{87}Rb ,
- Spin-selective forces I: independently manipulate $|\uparrow\rangle$ and not $|\downarrow\rangle$,
- Spin-selective forces II: independently manipulate both $|\uparrow\rangle$ and $|\downarrow\rangle$, and
- Isothermal Phase Space Cooling: sympathetic cooling without evaporation using K - Rb collisions [89, 90].

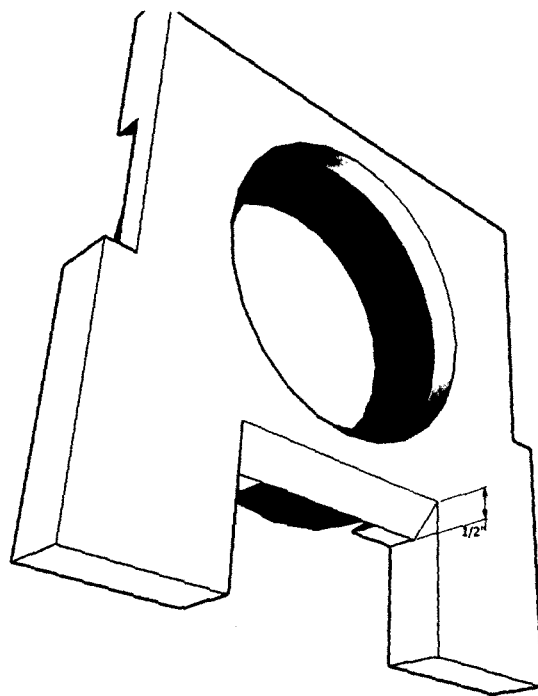
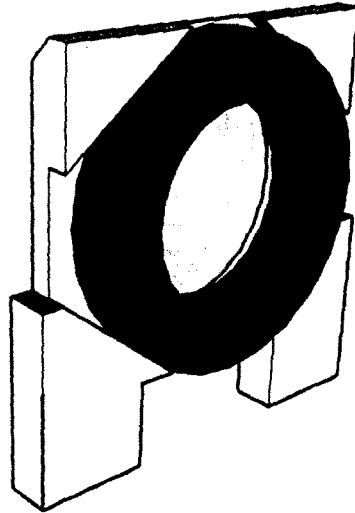
In the end, degenerate quantum gases remain a powerful platform with which to explore countless unanswered questions within many-body physics [91], fundamental quantum mechanics, precision metrology, quantum computing, and nuclear physics [13].

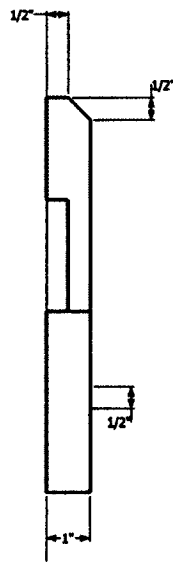
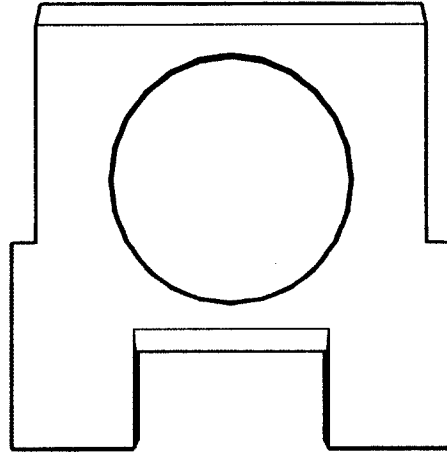
APPENDIX A

Engineering Designs

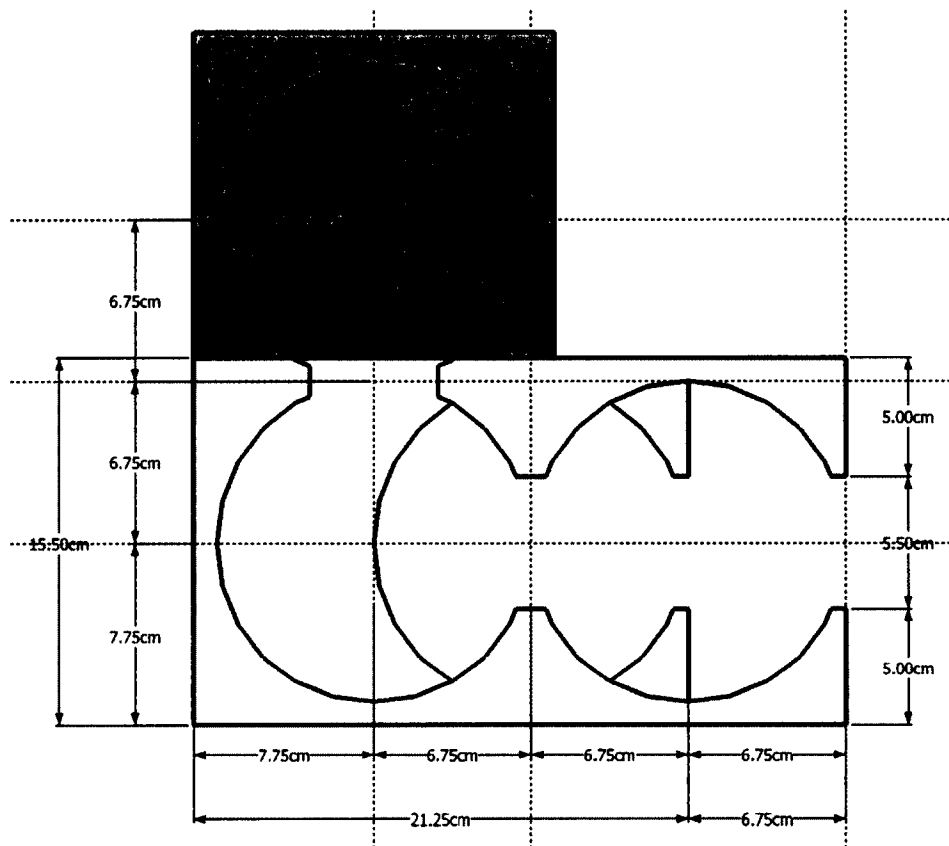
A.1 TIVAR MOT Coil Mount

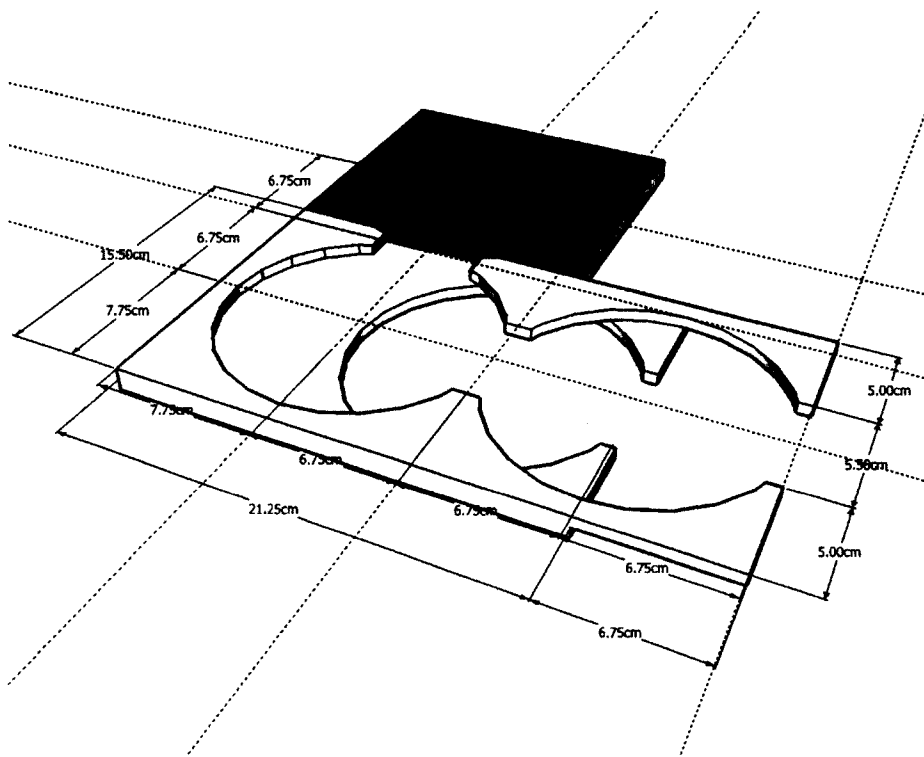
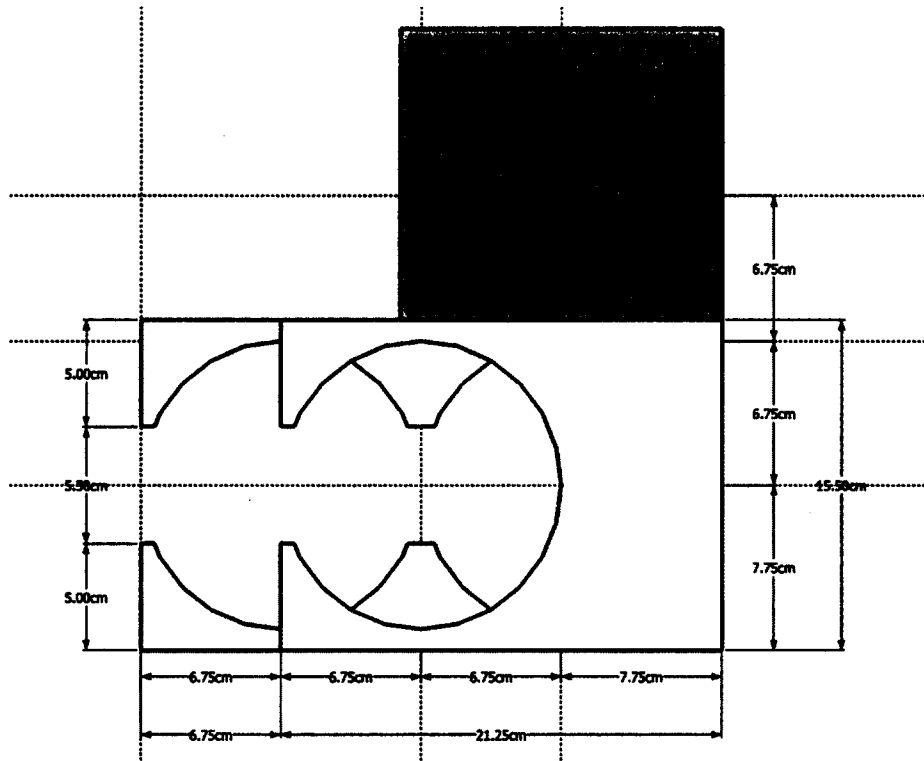


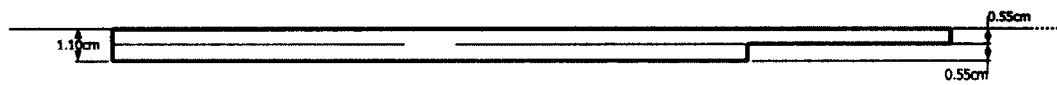




A.2 Copper Transport System Mount







BIBLIOGRAPHY

- [1] M. H. Anderson, J. R. Ensher, M. R. Matthews, C. E. Wieman, and E. A. Cornell, "Observation of Bose-Einstein Condensation in a Dilute Atomic Vapor," *Science* **269**, 198 (1995), <http://www.sciencemag.org/content/269/5221/198.full.pdf>, URL <http://www.sciencemag.org/content/269/5221/198.abstract>.
- [2] C. C. Bradley, C. A. Sackett, J. J. Tollett, and R. G. Hulet, "Evidence of Bose-Einstein Condensation in an Atomic Gas with Attractive Interactions," *Phys. Rev. Lett.* **75**, 1687 (1995), URL <http://link.aps.org/doi/10.1103/PhysRevLett.75.1687>.
- [3] K. B. Davis, M. O. Mewes, M. R. Andrews, N. J. van Druten, D. S. Durfee, D. M. Kurn, and W. Ketterle, "Bose-Einstein Condensation in a Gas of Sodium Atoms," *Phys. Rev. Lett.* **75**, 3969 (1995), URL <http://link.aps.org/doi/10.1103/PhysRevLett.75.3969>.
- [4] B. DeMarco and D. S. Jin, "Onset of Fermi Degeneracy in a Trapped Atomic Gas," *Science* **285**, 1703 (1999), <http://www.sciencemag.org/content/285/5434/1703.full.pdf>, URL <http://www.sciencemag.org/content/285/5434/1703.abstract>.
- [5] I. Bloch, J. Dalibard, and W. Zwerger, "Many-body physics with ultracold gases," *Rev. Mod. Phys.* **80**, 885 (2008), URL <http://link.aps.org/doi/10.1103/RevModPhys.80.885>.
- [6] M. R. Andrews, C. G. Townsend, H.-J. Miesner, D. S. Durfee, D. M. Kurn, and W. Ketterle, "Observation of Interference Between Two Bose Condensates," *Science* **275**, 637 (1997), <http://www.sciencemag.org/content/275/5300/637.full.pdf>, URL <http://www.sciencemag.org/content/275/5300/637.abstract>.
- [7] I. Bloch, T. W. Hänsch, and T. Esslinger, "Measurement of the spatial coherence of a trapped Bose gas at the phase transition," *Nature Physics* **403**, 166 (2000).
- [8] M. R. Matthews, B. P. Anderson, P. C. Haljan, D. S. Hall, C. E. Wieman, and E. A. Cornell, "Vortices in a Bose-Einstein Condensate," *Phys. Rev. Lett.* **83**, 2498 (1999), URL <http://link.aps.org/doi/10.1103/PhysRevLett.83.2498>.

- [9] P. Courteille, R. S. Freeland, D. J. Heinzen, F. A. van Abeelen, and B. J. Verhaar, "Observation of a Feshbach Resonance in Cold Atom Scattering," *Phys. Rev. Lett.* **81**, 69 (1998), URL <http://link.aps.org/doi/10.1103/PhysRevLett.81.69>.
- [10] H. Bethe, "Zur Theorie der Metalle," *Zeitschrift für Physik* **71**, 205 (1931), ISSN 0044-3328, URL <http://dx.doi.org/10.1007/BF01341708>.
- [11] M. A. Cazalilla, R. Citro, T. Giamarchi, E. Orignac, and M. Rigol, "One dimensional bosons: From condensed matter systems to ultracold gases," *Rev. Mod. Phys.* **83**, 1405 (2011), URL <http://link.aps.org/doi/10.1103/RevModPhys.83.1405>.
- [12] G. Sprouse, S. Aubin, E. Gomez, J. Grossman, L. Orozco, M. Pearson, and M. True, "Atomic probes of electromagnetic and weak interactions with trapped radioactive atoms," *The European Physical Journal A - Hadrons and Nuclei* **13**, 239 (2002), ISSN 1434-6001, URL <http://dx.doi.org/10.1140/epja1339-40>.
- [13] R. Collister, G. Gwinner, M. Tandecki, J. A. Behr, M. R. Pearson, J. Zhang, L. A. Orozco, S. Aubin, and E. Gomez (FrPNC Collaboration), "Isotope shifts in francium isotopes $^{206-213}\text{Fr}$ and ^{221}Fr ," *Phys. Rev. A* **90**, 052502 (2014), URL <http://link.aps.org/doi/10.1103/PhysRevA.90.052502>.
- [14] Cold Quanta, "Bose-Einstein condensate experiments to be conducted in space," Press Release (2013).
- [15] R. J. C. Spreeuw, C. Gerz, L. S. Goldner, W. D. Phillips, S. L. Rolston, C. I. Westbrook, M. W. Reynolds, and I. F. Silvera, "Demonstration of neutral atom trapping with microwaves," *Phys. Rev. Lett.* **72**, 3162 (1994), URL <http://link.aps.org/doi/10.1103/PhysRevLett.72.3162>.
- [16] N. Yu, J. M. Kohel, J. Ramirez-Serrano, J. R. Kellogg, L. Lim, and L. Maleki, "Progress towards a space-borne quantum gravity gradiometer," NASA's Earth Science & Technology Conference (2004).
- [17] M. J. Snadden, J. M. McGuirk, P. Bouyer, K. G. Haritos, and M. A. Kasevich, "Measurement of the Earth's Gravity Gradient with an Atom Interferometer-Based Gravity Gradiometer," *Phys. Rev. Lett.* **81**, 971 (1998), URL <http://link.aps.org/doi/10.1103/PhysRevLett.81.971>.
- [18] B. Dubetsky and M. A. Kasevich, "Atom interferometer as a selective sensor of rotation or gravity," *Phys. Rev. A* **74**, 023615 (2006), URL <http://link.aps.org/doi/10.1103/PhysRevA.74.023615>.
- [19] P. Böhi, M. Riedel, J. Hoffrogge, J. Reichel, T. W. Hänsch, and P. Treutlein, "Coherent manipulation of Bose-Einstein condensates with state-dependent microwave potentials on an atom chip," *Nature Physics* **5**, 592 (2009).

- [20] H. J. Metcalf and P. van der Straten, *Laser Trapping and Cooling* (Springer-Verlag, 1999).
- [21] N. Tammuz, Ph.D. thesis (2011).
- [22] M. Landini, Ph.D. thesis (2011).
- [23] J. Metzkes, "Design of a magnetic transfer system," (2008).
- [24] M. S. Yoon, Ph.D. thesis (2009).
- [25] I. I. Rabi, J. R. Zacharias, S. Millman, and P. Kusch, "A New Method of Measuring Nuclear Magnetic Moment," *Phys. Rev.* **53**, 318 (1938), URL <http://link.aps.org/doi/10.1103/PhysRev.53.318>.
- [26] D. A. Steck (2010), revision 2.1.4, URL <http://steck.us/alkalidata/>.
- [27] T. G. Tiecke (2011), revision 1.02, URL <http://www.tobiastiecke.nl/physics/>.
- [28] R. S. I. Williamson and T. Walker, "Magneto-optical trapping and ultracold collisions of Potassium atoms.," *J. Opti. Soc. Am. B* **12**, 1393 (1995).
- [29] M. S. Santos and et al., "Simultaneous trapping of two different atomic species in a vapor cell MOT.," *Phys. Rev. A* **52**, R4340 (1995).
- [30] C. Fort and et al., "Cooling mechanisms in Potassium magneto-optical traps.," *Eur. Phys. J. D* **3**, 113 (1998).
- [31] L. De Sarlo and et al., "Collisional properties of sympathetically cooled ^{39}K ," *Phys. Rev. A* **75**, 022715 (2007).
- [32] R. S. I. Williamson, "Magneto-optical trapping of potassium isotopes.," Ph.D. Thesis (1997).
- [33] H. Wang, P. Gould, and W. C. Stwalley, "Photoassociative spectroscopy of ultracold ^{39}K atoms in a high-density vapor-cell magneto-optical trap.," *Phys. Rev. A* **53**, R1216 (2003).
- [34] M. Landini, S. Roy, M. Simoni, A. Inguscio, G. Modugno, and M. Fattori, "Direct evaporative cooling of ^{39}K atoms to Bose-Einstein condensation," *Phys. Rev. A* **86**, 033421 (2012).
- [35] M. Landini, S. Roy, L. Carcagni, D. Trypogeorgos, M. Fattori, M. Inguscio, and G. Modugno, "Sub-Doppler laser colling of potassium atoms," *Phys. Rev. A* **84**, 043432 (2011).
- [36] G. Modugno, "Anderson localization in Bose-Einstein condensates.," *Rep. Prog. Phys* **73**, 102401 (2010).

- [37] S. S. Kondov, W. R. McGhee, J. J. Zirbel, and B. DeMarco, “Three-dimensional Anderson localization of ultracold matter,” *Science* **334**, 66 (2011).
- [38] M. Fattori and et al, “Atom interferometry with a weakly interacting Bose-Einstein condensate,” *Phys. Rev. Lett.* **100**, 080405 (2008).
- [39] C. Cohen-Tannoudji, B. Diu, and F. Laloë, *Quantum Mechanics* (Wiley, 1977).
- [40] T. Bergeman, G. Erez, and H. Metcalf, “Magnetostatic trapping fields for neutral atoms,” *Phys. Rev. A* **35** (1987).
- [41] M. M. Yee, “Magnetic Trapping and Transport of Ultracold Atoms,” (2009).
- [42] E. Majorana, “Atomi orientati in campo magnetico variabile.,” *Nuovo Cimento* **9**, 43 (1932).
- [43] J. Schwinger, “On nonadiabatic processes in inhomogenous fields,” *Phys. Rev* **51**, 648 (1937).
- [44] T. B. P. McNicholl, J. Kycia, H. Metcalf, and N. L. Balzs, “Quantized motion of atoms in a quadrupole magnetostatic trap,” *J. Opt. Soc. Am. B* **6**, 2249 (1989).
- [45] W. D. Phillips, J. V. Prodan, and H. J. Metcalf, “Laser cooling and electromagnetic trapping of neutral atoms,” *J. Opt. Soc. Am. B* **2**, 1751 (1985).
- [46] C. G. Townsend, N. H. Edwards, C. J. Cooper, K. P. Zetie, C. J. Foot, A. M. Steane, P. Szriftgiser, H. Perrin, and J. Dalibard, “Phase-space density in the magneto-optical trap,” *Phys. Rev. A* **52**, 1423 (1995), URL <http://link.aps.org/doi/10.1103/PhysRevA.52.1423>.
- [47] C. Zimmerman and M. Weidenmüller, eds., *Cold Atoms and Molecules* (Wiley-VCH, 2009).
- [48] C. C. Agosta, I. F. Silvera, H. T. C. Stoof, and B. J. Verhaar, “Trapping of neutral atoms with resonant microwave radiation,” *Phys. Rev. Lett.* **62**, 2361 (1989), URL <http://link.aps.org/doi/10.1103/PhysRevLett.62.2361>.
- [49] C. D’Errico, M. Zaccanti, G. Roati, G. Modugno, and M. Inguscio, “Feshbach resonances in ultracold ^{39}K ,” *N. J. Phys.* **9** (2007).
- [50] G. Thalhammer, G. Barontini, L. De Sarlo, J. Catani, F. Minardi, and M. Inguscio, “Double Species Bose-Einstein Condensate with Tunable Interspecies Interactions,” *Phys. Rev. Lett.* **100**, 210402 (2008), URL <http://link.aps.org/doi/10.1103/PhysRevLett.100.210402>.
- [51] G. Roati, M. Zaccanti, C. D’Errico, J. Catani, M. Modugno, A. Simoni, M. Inguscio, and G. Modugno, “ ^{39}K Bose-Einstein Condensate with Tunable Interactions,” *Phys. Rev. Lett.* **99**, 010403 (2007), URL <http://link.aps.org/doi/10.1103/PhysRevLett.99.010403>.

- [52] A. Simoni, F. Ferlaino, G. Roati, G. Modugno, and M. Inguscio, "Magnetic Control of the Interaction in Ultracold K-Rb Mixtures," *Phys. Rev. Lett.* **90**, 163202 (2003), URL <http://link.aps.org/doi/10.1103/PhysRevLett.90.163202>.
- [53] Z. Lu, J. A. Murakowski, C. A. Shuetz, S. Shi, G. J. Schneider, J. P. Samluk, and D. W. Prather, "Perfect lens makes a perfect trap," *Optics Express* **14**, 2228 (2006).
- [54] D. T. C. Allcock, T. P. Harty, C. J. Ballance, B. C. Keitch, N. M. Linke, D. N. Stacey, and D. M. Lucas, "A microfabricated ion trap with integrated microwave circuitry," *Applied Physics Letters* **102**, 044103 (2013), URL <http://scitation.aip.org/content/aip/journal/apl/102/4/10.1063/1.4774299>.
- [55] D. Aude Craik, N. Linke, T. Harty, C. Ballance, D. Lucas, A. Steane, and D. Allcock, "Microwave control electrodes for scalable, parallel, single-qubit operations in a surface-electrode ion trap," *Applied Physics B* **114**, 3 (2014), ISSN 0946-2171, URL <http://dx.doi.org/10.1007/s00340-013-5716-7>.
- [56] C. Ospelkaus, C. E. Langer, J. M. Amini, K. R. Brown, D. Leibfried, and D. J. Wineland, "Trapped-Ion Quantum Logic Gates Based on Oscillating Magnetic Fields," *Phys. Rev. Lett.* **101**, 090502 (2008), URL <http://link.aps.org/doi/10.1103/PhysRevLett.101.090502>.
- [57] C. Ospelkaus, U. Warring, Y. Colombe, J. M. Amini, K. R. Brown, D. Leibfried, and D. J. Wineland, "Microwave quantum logic gates for trapped ions," *Nature* **476**, 181 (2001).
- [58] U. Warring, C. Ospelkaus, Y. Colombe, K. R. Brown, J. M. Amini, M. Carsjens, D. Leibfried, and D. J. Wineland, "Techniques for microwave near-field quantum control of trapped ions," *Phys. Rev. A* **87**, 013437 (2013), URL <http://link.aps.org/doi/10.1103/PhysRevA.87.013437>.
- [59] T. P. Harty, D. T. C. Allcock, J. Ballance, C., L. Guidoni, H. A. Janacek, N. M. Linke, D. N. Stacey, and D. M. Lucas, "High-Fidelity Preparation, Gates, Memory, and Readout of a Trapped-Ion Quantum Bit," *Phys. Rev. Lett.* **113**, 220501 (2014), URL <http://link.aps.org/doi/10.1103/PhysRevLett.113.220501>.
- [60] W. H. Wing, "On neutral particle trapping in quasistatic electromagnetic fields," *Progress in Quantum Electronics* **8**, 181 (1984), ISSN 0079-6727, URL <http://www.sciencedirect.com/science/article/pii/0079672784900120>.
- [61] J. Fortágh and C. Zimmermann, "Magnetic microtraps for ultracold atoms," *Rev. Mod. Phys.* **79**, 235 (2007), URL <http://link.aps.org/doi/10.1103/RevModPhys.79.235>.

- [62] P. Krüger, L. M. Andersson, S. Wildermuth, S. Hofferberth, E. Haller, S. Aigner, S. Groth, I. Bar-Joseph, and J. Schmiedmayer, “Potential roughness near lithographically fabricated atom chips,” *Phys. Rev. A* **76**, 063621 (2007), URL <http://link.aps.org/doi/10.1103/PhysRevA.76.063621>.
- [63] V. Bolpasi and W. von Klitzing, “Double-pass tapered amplifier diode laser with an output power of 1W for an injection power of only 200 μ W,” *Rev. Sci. Inst.* **81**, 113108 (2010).
- [64] V. M. Valenzuela, L. Hernandez, and E. Gomez, “High power rapidly tunable system for laser cooling,” *Rev. Sci. Inst.* **83**, 015111 (2012).
- [65] J. H. Huckans, I. B. Spielman, B. L. Tolra, W. D. Phillips, and J. V. Porto, “Quantum and classical dynamics of a Bose-Einstein condensate in a large-period optical lattice,” *Phys. Rev. A* **80**, 043609 (2009), URL <http://link.aps.org/doi/10.1103/PhysRevA.80.043609>.
- [66] J. Thywissen, Group Website.
- [67] D. Anderson, Group Website.
- [68] M. K. Ivory, Private communication.
- [69] J. Schmiedmayer, Group Website.
- [70] S. Aubin, M. H. T. Extavour, S. Myrskog, L. J. Leblanc, J. Esteve, S. Singh, P. Scrutton, D. McKay, R. McKenzie, I. D. Leroux, et al., “Trapping Fermionic ^{40}K and Bosonic ^{87}Rb on a Chip,” *J. Low Temp. Phys.* **140**, 377 (2005).
- [71] J. Thywissen, personal communication with Seth Aubin.
- [72] T. L. Gustavson, A. P. Chikkatur, A. E. Leanhardt, A. Görlitz, S. Gupta, D. E. Pritchard, and W. Ketterle, “Transport of Bose-Einstein Condensates with Optical Tweezers,” *Phys. Rev. Lett.* **88**, 020401 (2001), URL <http://link.aps.org/doi/10.1103/PhysRevLett.88.020401>.
- [73] H. J. Lewandowski, D. M. Harber, D. L. Whitaker, and E. A. Cornell, “Simplified system for creating a bose-einstein condensate,” *J. Low Temp. Phys.* (2003).
- [74] J. H. T. Burke and C. A. Sackett, “Scalable Bose-Einstein-condensate Sagnac interferometer in a linear trap,” *Phys. Rev. A* **80**, 061603 (2009), URL <http://link.aps.org/doi/10.1103/PhysRevA.80.061603>.
- [75] J. McGuirk, personal communication with Seth Aubin.
- [76] B. Battelier, Ph.D. thesis (2007).
- [77] K. Winkler, Ph.D. thesis (2002).

- [78] M. Greiner, I. Bloch, T. W. Hänsch, and T. Esslinger, “Magnetic transport of trapped cold atoms over a large distance,” *Phys. Rev. A* **63**, 031401 (2001), URL <http://link.aps.org/doi/10.1103/PhysRevA.63.031401>.
- [79] D. R. Fernandes, F. Sievers, N. Kretzschmar, S. Wu, C. Salomon, and F. Chevy, “Sub-Doppler laser cooling of fermionic 40 K atoms in three-dimensional gray optical molasses,” *EPL (Europhysics Letters)* **100**, 63001 (2012), URL <http://stacks.iop.org/0295-5075/100/i=6/a=63001>.
- [80] G. Salomon, L. Fouch, P. Wang, A. Aspect, P. Bouyer, and T. Bourdel, “Gray-molasses cooling of ^{39}K to a high phase-space density,” *EPL (Europhysics Letters)* **104**, 63002 (2013), URL <http://stacks.iop.org/0295-5075/104/i=6/a=63002>.
- [81] R. A. Nyman, G. Varoquaux, B. Villier, D. Sacchet, F. Moron, Y. Le Coq, A. Aspect, and P. Bouyer, “Tapered-amplified antireflection-coated laser diodes for potassium and rubidium atomic-physics experiments,” *Review of Scientific Instruments* **77**, 033105 (2006).
- [82] K. Lindquist, M. Stephens, and C. Wieman, “Experimental and theoretical study of the vapor-cell Zeeman optical trap,” *Phys. Rev. A* **46**, 4082 (1992), URL <http://link.aps.org/doi/10.1103/PhysRevA.46.4082>.
- [83] M. D. Barrett, J. A. Sauer, and M. S. Chapman, “All-Optical Formation of an Atomic Bose-Einstein Condensate,” *Phys. Rev. Lett.* **87**, 010404 (2001), URL <http://link.aps.org/doi/10.1103/PhysRevLett.87.010404>.
- [84] N. Masuhara et al., “Evaporative cooling of spin-polarized atomic Hydrogen,” *Phys. Rev. Lett* **61**, 935 (1988).
- [85] R. L. D. Campbell, R. P. Smith, N. Tammuz, S. Beattie, S. Moulder, and Z. Hadzibabic, “Efficient production of large ^{39}K Bose-Einstein condensates,” *Phys. Rev. A* **82**, 063611 (2010), URL <http://link.aps.org/doi/10.1103/PhysRevA.82.063611>.
- [86] D. Ciampini, E. Courtade, C. Sias, D. Cossart, G. Carelli, F. Mango, O. Morsch, and E. Arimondo, “Manipulation of ultracold atomic mixtures using microwave techniques,” *Optics Communications* **257**, 340 (2006), ISSN 0030-4018, URL <http://www.sciencedirect.com/science/article/pii/S0030401805007418>.
- [87] G. Modugno, G. Ferrari, G. Roati, R. J. Brecha, A. Simoni, and M. Inguscio, “Bose-Einstein Condensation of Potassium Atoms by Sympathetic Cooling,” *Science* **294**, 1320 (2001), <http://www.sciencemag.org/content/294/5545/1320.full.pdf>, URL <http://www.sciencemag.org/content/294/5545/1320.abstract>.

- [88] R. Côté, A. Dalgarno, H. Wang, and W. C. Stwalley, “Potassium scattering lengths and prospects for Bose-Einstein condensation and sympathetic cooling,” *Phys. Rev. A* **57**, R4118 (1998), URL <http://link.aps.org/doi/10.1103/PhysRevA.57.R4118>.
- [89] L. J. LeBlanc and J. H. Thywissen, “Species-specific optical lattices,” *Phys. Rev. A* **75**, 053612 (2007), URL <http://link.aps.org/doi/10.1103/PhysRevA.75.053612>.
- [90] M. Brown-Hayes and R. Onofrio, “Optimal cooling strategies for magnetically trapped atomic Fermi-Bose mixtures,” *Phys. Rev. A* **70**, 063614 (2004), URL <http://link.aps.org/doi/10.1103/PhysRevA.70.063614>.
- [91] C. Chin, R. Grimm, P. Julienne, and E. Tiesinga, “Feshbach resonances in ultracold gases,” *Rev. Mod. Phys.* **82**, 1225 (2010), URL <http://link.aps.org/doi/10.1103/RevModPhys.82.1225>.

VITA

Austin Robert Ziltz

Austin R. Ziltz was born on the 30th of April, 1986 in Harrisburg, Pennsylvania. He attended West Hanover Elementary School, Central Dauphin East Junior High and Central Dauphin High School. After being inadvertently electrocuted several times during his youth, he eventually found a passion for physics. In 2004, he entered Bucknell University. He graduated with honors in 2008 with a Bachelor of Science in Physics and a minor in Mathematics. Austin entered the College of William & Mary in the fall of 2008, and began work with Dr. Seth Aubin in the Ultracold Atoms Group to develop microwave and RF atom chip potentials and the apparatus with which to study them. He received a Master of Science in 2010. Austin began working for Laser & Plasma Technologies in Hampton, Virginia in October 2014, developing corrosion detection instruments for the Navy.